2014

Enzyme-Based Nitric Oxide Releasing Thin Films and Scaffolds

Mutha Merenna Nuwan Bhagya Gunasekera
Cleveland State University

Recommended Citation

Gunasekera, Mutha Merenna Nuwan Bhagya, "Enzyme-Based Nitric Oxide Releasing Thin Films and Scaffolds" (2014). *ETD Archive*. 114.
https://engagedscholarship.csuohio.edu/etdarchive/114

ENZYME-BASED NITRIC OXIDE RELEASING THIN FILMS AND SCAFFOLDS

MUTHA MERENNA NUWAN BHAGYA GUNASEKERA

Bachelor of Science in Biology

University of Colombo

August, 2003

Master of Science in Analytical Chemistry

University of Colombo

July, 2008

submitted in partial fulfillment of requirements for the degree

DOCTOR OF PHILOSOPHY IN CLINICAL-BIOANALYTICAL CHEMISTRY

at the

CLEVELAND STATE UNIVERSITY

May 2014

We hereby approve this dissertation

for

Mutha Merenna Nuwan Bhagya Gunasekera

Candidate for the Doctor of Philosophy in Clinical-Bioanalytical Chemistry Degree

for the

Department of Chemistry

and

CLEVELAND STATE UNIVERSITY'S

College of Graduate Studies

Mekki Bayachou. PhD.

Department of Chemistry / May 5th 2014

David W. Ball. PhD.

Department of Chemistry / May 5th 2014

John F. Turner. PhD.

Department of Chemistry / May 5th 2014

Parthasarathy Srinivasan. PhD.

Department of Mathematics / May 5th 2014

Gary Wnek. PhD.

Department of Macromolecular Science and Engineering,

Case Western Reserve University / May 5th 2014

Student's Date of Defense: April 29th 2014

ACKNOWLEDGEMENTS

I thank first, my advisor Dr. Mekki Bayachou, for his help and guidance throughout the years. Next, I thank members of the dissertation committee, Dr. David W. Ball, Dr. John F. Turner, Dr. Parthasarathy Srinivasan and Dr. Gary Wnek for their time and advice. I also thank faculty members and staff of the Department of Chemistry, College of Science and Health Professions, College of Graduate Studies and the Center for International Services and Programs for their help with coursework and administrative matters. I thank past lab members of the Bayachou lab group for the work that I was able to build upon. I also thankfully commit to my memory, all my peers of Bayachou group and Wnek group (Case Western Reserve University) for their support.

I would like to dedicate this thesis to all my family members and all my teachers whose blessings have always been with me.

ENZYME-BASED NITRIC OXIDE RELEASING THIN FILMS AND SCAFFOLDS

MUTHA MERENNA NUWAN BHAGYA GUNASEKERA

ABSTRACT

Nitric oxide synthase enzyme (NOS) embedded in thin films and scaffolds, when exposed to a solution of its substrate arginine, a source of reducing equivalents, and other required ingredients of the NOS reaction, can release fluxes of nitric oxide (NO). The latter is a molecule known to counteract platelet aggregation, and thus can prevent the thrombosis cascade on the surfaces of implantable medical devices. Therefore NO antithrombogenic regimens such as active coatings and embedded scaffolds have the potential to increase the lifespan of implantable biomaterials.

Layer-by-layer electrostatic adsorption allows for assembly of multi-component protein/polyelectrolytes nanostructured films. Electrospun fiber matrices may embed proteins in aqueous pockets that allow the formation of functional scaffolds. Such functional coatings and polymer scaffolds have potential applications as antithrombotic surfaces. In this project, inducible nitric oxide synthase is proposed as a functional component in active thin films and electrospun scaffolds for nitric oxide release under physiologic conditions.

Atomic force microscopic (AFM) imaging confirms the presence of enzyme in adsorbed thin films. Fourier transform infrared (FTIR) spectroscopic analysis was used to characterize structure-function relationships of NOS-containing thin films. Voltammetry was used to characterize the active catalyst concentration on adsorbed surfaces and activity of NOS-containing thin films. Further, analysis of cyclic voltammetric data enabled the study of Michaelis-Menten kinetics of NOS-containing thin films. Other spectrophotometric and spectrofluorometric assays were used to monitor nitric oxide release for the NOS-based thin films and scaffolds. Three polymers were characterized for their ability to embed iNOSoxy and show enzyme activity in electrospun scaffolds.

For the LbL method, during protein adsorption, an adjusted pH of 8.6 or the use of a branched matrix immobilizes more enzyme units in thin layers compared to pH 7.0 or a linearly structured polymer matrix. However, the enzyme structure adsorbed at pH 7.0 allows faster catalytic turnover of substrate compared to enzyme structure from pH 8.6 immobilization. Overall, both the cumulative nitric oxide output and the flux were higher for films immobilized at pH 8.6 or adsorbed onto branched polymer matrices. Electrospun fiber scaffolds produce nitric oxide when bathed in a cocktail containing the ingredients of NOS catalyzed reaction.

TABLE OF CONTENTS

Page

LIST OF TABLES .... **XI**

LIST OF FIGURES .... **XII**

NOMENCLATURE .... **XVIII**

GENERAL INTRODUCTION **1**

Background 1

Thrombogenesis 2

Nitric oxide in antithrombogenic regimens 2

Nitric oxide and nitric oxide synthase 5

Mechanism of nitric oxide mediated antithrombogenesis 8

Electrostatically adsorbed thin films of NOS enzyme 9

NOS embedded electrospun scaffolds 11

NO as a short-lived reactive species and its significance in localized activity..... 13

CHAPTER I: IMPROVED ENZYME LOADING IN LAYER-BY-LAYER (LBL) ADSORBED THIN FILMS OF INDUCIBLE NITRIC OXIDE SYNTHASE (INOS) AND POLYETHYLENIMINE (PEI) **14**

1.1 Introduction 14

1.1.1 Isoelectric point of iNOS and its significance 15

1.2 Experimental 16

1.2.1 Expression and purification of iNOSoxy through recombinant plasmid DNA 16

1.2.2 Adjustment of pH of protein in solution 18

1.2.3 Atomic force microscopic (AFM) imaging of adsorbed thin films 19

1.2.4 Electrochemical investigation of heme-Fe^{3+} reduction and catalytic NO reduction by LbL immobilized PEI/iNOSoxy films on graphite electrodes 20

1.2.5 Fourier Transform Infrared Spectroscopy (FTIR) on thin protein layers . 21

1.2.6 Griess assay for the determination of activity of thin films of PEI/iNOSoxy 22

1.3 Results and discussion 24

1.3.1 AFM images of iNOSoxy on PEI-modified surfaces 24

1.3.2 Electrocatalytic reduction of NO mediated by iNOSoxy in films 29

1.3.2.1 iNOSoxy-heme Fe^{3+} reduction as a quantifier of immobilization 31

1.3.2.2 Catalytic reduction of NO mediated by iNOSoxy on PEI/iNOSoxy films on PG electrodes 34

1.3.2.3 Michaelis-Menten kinetics 37

1.3.3 FTIR Characterization of PEI/iNOSoxy films prepared at various pH's . 40

1.3.4 Activity of iNOSoxy / PEI thin films 44

1.4 Conclusion 48

1.5 Reference 49

CHAPTER II: LBL THIN FILMS OF INDUCIBLE NITRIC OXIDE SYNTHASE OXYGENASE (INOSOXY) AND BRANCHED POLYETHYLENIMINE (PEI)... 62

2.1 Introduction ... 62

2.1.1 Charge density of matrix polymer and its significance ... 63

2.2 Experimental ... 64

2.2.1 Expression and purification of iNOSoxy through recombinant plasmid DNA ... 64

2.2.2 Atomic force microscopic (AFM) imaging of adsorbed thin layers ... 65

2.2.3 Griess assay for the determination of activity of thin films of iNOSoxy . 66

2.2.4 Electrochemical investigation of heme-Fe^{3+} reduction and catalytic NO reduction by LbL immobilized PEI/iNOSoxy films on graphite electrodes ... 67

2.3 Results and discussion ... 70

2.3.1 AFM imaging of modified surfaces ... 70

2.3.2 Activity of thin films of enzyme ... 75

2.3.3 Electrochemistry and Michaelis-Menten kinetics ... 79

2.3.3.1 Electrocatalytic reduction of NO mediated by iNOSoxy in films ... 79

2.3.3.2 iNOSoxy-heme Fe^{3+} reduction as a quantifier of immobilization ... 81

2.3.3.3 Catalytic reduction of NO by iNOSoxy immobilized on branched and linear PEI ... 83

2.3.3.4 Michaelis-Menten kinetics ... 86

2.4 Conclusion 89

2.5 Reference 90

CHAPTER III: INDUCIBLE NITRIC OXIDE SYNTHASE OXYGENASE (INOSOXY) ENCAPSULATED IN ELECTROSPUN FIBER SCAFFOLDS AND MATS 94

3.1 Introduction 94

3.1.1 Electrospinning 94

3.1.2 The polymers 96

3.2 Experimental 99

3.2.1 iNOSoxy structural study by FTIR in different organic solvent mixtures used in electrospinning 99

3.2.2 Activity of iNOSoxy in polymer mixture before electrospinning 99

3.2.3 Electrospinning apparatus 100

3.2.4 Preparation of polymer solution and electrospinning parameters 101

3.2.5 Optical microscopic imaging of electrospun scaffolds and mats 103

3.2.6 Scanning Electron Microscopic imaging of electrospun scaffolds and mats 104

3.2.7 Activity of iNOSoxy enzyme embedded in PVA scaffold through Griess reagent system 104

3.2.8 Activity of iNOSoxy enzyme embedded in scaffold using a fluorometric method ... 105

3.3 Results and Discussion ... 108

3.3.1 FTIR analysis for protein structure in organic solvent systems ... 108

3.3.2 Activity of iNOSoxy in polymer mixture before electrospinning ... 108

3.3.3 Physical characteristics of electrospun fiber scaffolds and mats ... 110

3.3.4 Optical microscopic imaging ... 113

3.3.5 Scanning electron microscopic imaging ... 118

3.3.6 Activity of iNOSoxy enzyme embedded in scaffolds ... 122

3.4 Conclusion ... 125

3.5 Reference ... 126

LIST OF TABLES

Table **Page**

Table 1: Extracted Michaelis-Menten parameters from nonlinear regression fitting using Michaelis-Menten model... 39

Table 2: Extracted Michaelis-Menten parameters from non-linear regression fitting using Michaelis-Menten model... 88

Table 3: Electrospinning parameters for each polymer/solvent system................ 103

LIST OF FIGURES

Figure **Page**

Figure 1: Scheme showing thrombosis at the surface of medical implant material... 4

Figure 2: A schematic representation of the depletion of NO source in a multilayer release coating; a) at the initial stages, b) depletion over time. 4

Figure 3: A schematic representation of the general reaction catalyzed by NOS. 6

Figure 4: Reaction sequence in the reductase domain for the electron shunt; 1) $NADPH_2$ to NADP, 2) $FADH_2$ to FAD, 3) $FMNH_2$ to FMN. 7

Figure 5: A schematic representation of a cross section of the LbL adsorbed monolayer of NOS. Enzyme converts substrate to NO. Hence a NOS immobilized implant displays intrinsic antithrombogenic activity. 10

Figure 6: A schematic representation of the LbL adsorbed monolayers of (-) charged enzyme protein onto (+) charged polymer matrix layer on surface. 10

Figure 7: A schematic representation of an embedded aqueous 'node' in an electrospun scaffold microfiber. 12

Figure 8: AFM images on the topology of the bare and PEI matrix adsorbed surfaces; a) Bare HOPG (scan size 25 μm × 25 μm), b) PEI immobilized on HOPG for 5min (Scan size: 25 μm × 25 μm). 25

Figure 9: AFM images with a 3-D perspective of the topology of the outermost layer in iNOSoxy immobilization on PEI; a) Outermost iNOSoxy layer immobilized at pH 7.0

(Scan size: 1 μm × 1 μm), b) Outermost iNOSoxy layer immobilized at pH 8.6 (Scan size: 1 μm × 1 μm). 26

Figure 10: Histogram of cluster abundance in various diameter ranges for pH 8.6 and pH 7.0 PEI/iNOSoxy films. 28

Figure 11: Typical cyclic voltammogram showing Fe^{3+}/Fe^{2+} (approx. 500mV) and Fe^{2+}/Fe^{+} (approx. 950mV) redox couples for the heme moieties in an iNOSoxy immobilized electrode. The effect of Ohmic drop has been removed by mathematically treating the original voltammogram.. 30

Figure 12: Integrals of characteristic Fe^{3+} reduction in 8mV.s^{-1} linear sweep voltammograms for iNOSoxy/PEI films adsorbed from iNOSoxy solution at pH 8.6 and pH 7.0. 32

Figure 13: Average of integrals of the characteristic Fe^{3+} reduction in 8mV.s^{-1} linear sweep voltammograms showing different amounts of immobilization at different pH's. Standard deviation based on data for the same batch of electrodes immobilized at pH 8.6 and 7.0 (N=5). 33

Figure 14: Cyclic voltammogram (200mV.s^{-1}) for catalytic NO reduction by different amounts of iNOSoxy immobilized at different pH's measured at the same NO concentration (120 μM). 35

Figure 15: Average catalytic peak current for NO reduction at the surfaces of iNOSoxy/PEI modified electrodes prepared at pH 7.0 and pH 8.6. Standard deviation based on data for the same batch of electrodes immobilized at the respective pH's (N=5). 38

Figure 16: Deconvoluted Amide I bands for the envelope signals obtained at pH 7.0 and pH 8.6 immobilization. 42

Figure 17: Deconvoluted Amide II bands for the envelope signals obtained at pH 7.0 and pH 8.6 immobilization. 43

Figure 18: Average cumulative NO concentration for immobilization pH values, pH 7.0 & pH 8.6; Standard deviation shown where N=3 for each immobilization pH.......... 45

Figure 19: Average surface NO flux for each immobilization pH value; pH 7.0 & pH 8.6; Standard deviation shown where N=3 for each immobilization pH......... 47

Figure 20: AFM images on the topology of the bare and PEI matrix adsorbed surfaces; a) Bare HOPG (scan size 25 μm × 25 μm), b) PEI immobilized on HOPG for 5min (Scan size: 25 μm × 25 μm). 71

Figure 21: AFM images on the topology of the outermost layer in iNOSoxy immobilization on PEI; a) Outermost NOS layer immobilized at pH 8.6 on linear PEI matrix (Scan size: 1 μm × 1 μm) & b) Outermost NOS layer immobilized at pH 8.6 on branched PEI matrix (Scan size: 1 μm × 1 μm). 72

Figure 22: Histographic comparison of cluster diameters for Figure 21 a) & 21 b) showing number of features in each diameter range. 74

Figure 23: Average cumulative NO concentration generated from iNOSoxy/PEI films using branched PEI and linear PEI. Error bars represent standard deviations for 5 trials. 76

Figure 24: Average surface flux of NO from iNOSoxy/PEI films immobilized on branched PEI and linear PEI. Error bars represent standard deviations for 5 trials.......... 78

Figure 25: Typical cyclic voltammogram showing Fe^{3+}/Fe^{2+} (approx. 500mV) and Fe^{2+}/Fe^{+} (approx. 950mV) redox couples for the heme moieties in an iNOSoxy immobilized electrode. The effect of Ohmic drop has been removed by mathematically treating the original graph. 80

Figure 26: Integrals of characteristic Fe^{3+} reduction in $8mV.s^{-1}$ linear sweep voltammograms for iNOSoxy/PEI films adsorbed on linear PEI and branched PEI. Thin films immobilized from iNOSoxy solution at pH 8.6 82

Figure 27: Average of integrals of the characteristic Fe^{3+} reduction in $8mV.s^{-1}$ linear sweep voltammograms for iNOSoxy/PEI films adsorbed on linear PEI and branched PEI. Standard deviation based on data for the same batch of electrodes immobilized at pH 8.6 (N=5). 83

Figure 28: Cyclic voltammogram (200 $mV.s^{-1}$) for catalytic NO reduction iNOSoxy immobilized on linear PEI and branched PEI, measured at the same NO concentration (120 μM). Immobilization pH is 8.6. 85

Figure 29: Average catalytic peak current for NO reduction at the surfaces of thin films of iNOSoxy adsorbed at pH 8.6 onto linear PEI and branched PEI. Standard deviation based on data for the same batch of electrodes immobilized using linear and branched PEI (N=5). 87

Figure 30: Structures of a) polycaprolactone, b) polyvinyl alcohol and, c) polyethyl-vinyl acetate. 98

Figure 31: A schematic representation of a typical electrospinning apparatus. 101

Figure 32: Reaction scheme for the detection of NO by DAF-FM diacetate 107

Figure 33: Activity of iNOSoxy prior to electrospinning in three different homogenized polymer/solvent mixtures and iNOSoxy. Control is provided by iNOSoxy enzyme in EPPS buffer. Error bars represent standard deviations in repeated trials (N=3). 109

Figure 34: A photograph of a section of PCL scaffold retrieved from the small 4 mm mandrel immediately after electrospinning. Electrospinning conditions: Air-gap distance: 15 cm, Potential: 15 kV, Electrospinning emulsion ratio (v/v): 20:1 (Polymer mixture : iNOSoxy containing buffer), Flow rate 1 ml/hr........ 111

Figure 35: A photograph of a section of PEVA scaffold cut open and retrieved from the small 4 mm mandrel after electrospinning. Electrospinning conditions: Air-gap distance: 30 cm, Potential: 15 kV, Electrospinning emulsion ratio (v/v): 20:1 (Polymer mixture : iNOSoxy containing buffer), Flow rate 3 ml/hr. 111

Figure 36: A photograph of a section of PVA scaffold retrieved from the large mandrel immediately after electrospinning. Electrospinning conditions: Air-gap distance: 15 cm, Potential: 15 kV, Electrospinning emulsion ratio (v/v): 20:1 (Polymer mixture : iNOSoxy containing buffer), Flow rate 1 ml/hr. 112

Figure 37: Optical microscopic images of PCL microfibers stained with Sudan IV. 114

Figure 38: Optical microscopic images of PCL microfibers with encapsulated pockets of iNOSoxy. 115

Figure 39: Fluorescence microscopic image of FITC stained PCL electrospun microfibers. Electrospinning conditions: Air-gap distance: 15 cm, Potential: 15 kV,

Electrospinning emulsion ratio (v/v): 20:1 (Polymer mixture : iNOSoxy containing buffer), Flow rate 1 ml/hr.. 117

Figure 40: SEM images of electrospun 10% w/w PCL with 20:1 v/v iNOSoxy in EPPS buffer. 119

Figure 41: SEM images of electrospun 10% w/w PVA with 20:1 v/v iNOSoxy in EPPS buffer. 120

Figure 42: Mean fiber diameter of PCL showing increase of mean fiber diameter in the presence of encapsulated aqueous pockets. Error bars show standard deviations (N=43)... 121

Figure 43: Cumulative NO concentration resulting from iNOSoxy embedded in PCL and PEVA scaffolds in comparison to iNOSoxy immobilized thin film activity........... 123

Figure 44: NO flux for each type of scaffold compared to flux of thin films of iNOSoxy. 124

NOMENCLATURE

Amp:	Ampicillin
AFM:	Atomic force microscopy
ATR:	Attenuated total reflectance
CaM:	Calmodulin
CV:	Cyclic voltammetry
δ-ALA:	δ-Aminolevulinic acid
DI:	De-ionized
DMSO:	Dimethyl sulfoxide
DTT:	Dithiothreitol
EPPS:	3-[4-(2-hydroxyethyl)piperazin-1-yl]propane-1-sulfonic acid
FAD:	Flavin adenine dinucleotide
FE-SEM:	Field emission scanning electron microscope
FITC:	Fluorescein isothiocyanate
FMN:	Flavin mononucleotide
FTIR:	Fourier transform infrared spectroscopy
H_4B:	Tetrahydrobiopterin

Hb:	Hemoglobin
HOPG:	Highly oriented pyrolytic graphite
iNOS:	Inducible Nitric Oxide Synthase
iNOSoxy:	Inducible Nitric Oxide Synthase Oxygenase
IPTG:	Isopropyl β-D-1-thiogalactopyranoside
LB:	Lysogeny broth
LbL:	Layer-by-layer
MWCO:	Molecular weight cut-off
NADPH:	Nicotinamide adenine dinucleotide phosphate
NED:	N-1-napthylethylenediamine dihydrochloride
NHA:	N-hydroxy-L-arginine
NO:	Nitric oxide
NOS:	Nitric Oxide Synthase
PCL:	Poly(Caprolactone)
PEI:	Polyethylenimine
PEVA:	Poly(Ethylene-co-vinyl acetate)
PG:	Pyrolytic graphite
PLL:	Poly-L-lysine
PMSF:	Phenylmethanesulfonyl fluoride

PVA:	Polyvinyl alcohol
SEM:	Scanning electron microscopy
SPIP®:	Scanning probe image processor
TB:	Terrific broth
UV-Vis:	Ultraviolet – visible

GENERAL INTRODUCTION

Background

Increase of life expectancy is ascribed in part to the marked successes in the use of medical implants. Diseases once considered untreatable make use of synthetic inserts for better outcomes and are replacing or competing with surgical methods of intervention [1, 2]. Medical implants are becoming common practice in the treatment of acute to chronic ailments, end-stage diseases, and post-traumatic surgeries. While the use of blood-contacting medical implants increased over the past few decades [3], their lifespan and inherent need for replacement has become a concern. Implant malfunction is presented as clinical complications and can be life-threatening. One of the main causes needing surgical replacement for a medical implant is the intrinsic thrombosis cascade on its surface that causes it to be defective [4, 5]. For example, studies reveal that stent thrombosis in the coronary artery result in 20-48% complications and death while 60-70% of the cases studied resulted in myocardial infarction [6]. In other studies, control groups of animals not administered with drugs showed thrombosis cascade on the luminal surfaces of polyurethane grafts in contrast to sample population treated with potential suppressants [7].

Thrombogenesis

All blood-contacting foreign-body surfaces are prone to a thrombosis cascade regardless of surface properties [8, 9]. It involves both cellular and protein components. Adsorption of fibrinogen onto the surface/s of the implant initiates the thrombosis cascade followed by the recruitment of platelets [10-12], which presents a clinical complication, as depicted in Figure 1.

Nitric oxide in antithrombogenic regimens

The success of implants that has a built-in antithrombogenic regimen such as in drug-eluting stents has been reported previously [13-15]. A number of surface modification methods are being used to increase the blood compatibility of blood-contacting implants [16]. Release of an antithrombogenic chemical reagent is one approach that has been adopted [6]. Nitric oxide (NO) is one such molecular intervention for maintaining vascular hemostasis [17], that also exhibits direct inhibitory action on platelet aggregation [18]. Towards this end, direct NO release by NO donors such as S-nitrothiols [19] and N-diazeniumdiolates [20] have been reported as potential routes for preparing NO-releasing films that can be applied to blood-contacting implants.

However, NO releasing chemical coatings do not completely resolve the issue of graft thrombosis. As shown by Figure 2, release coatings are a time-limited source of NO, considering longer lifespan of most blood-contacting internal implants. Over a long period of time, a depletion of NO source allows further recruitment of platelets and the thrombosis cascade. The biocompatibility of direct chemical interventions is another common concern. This work replaces chemically synthesized NO release coatings with layer-by-layer (LbL) immobilized thin films of nitric oxide synthase (NOS) enzyme.

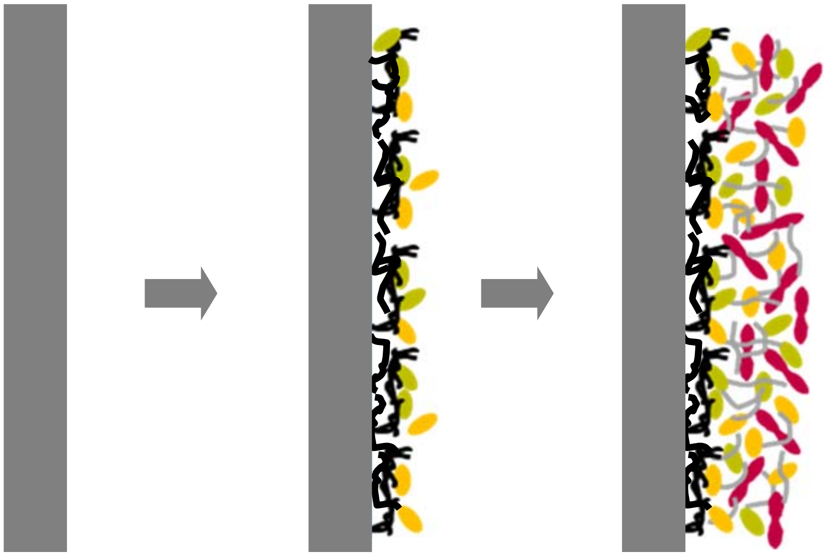

Figure 1: Scheme showing thrombosis at the surface of medical implant material.

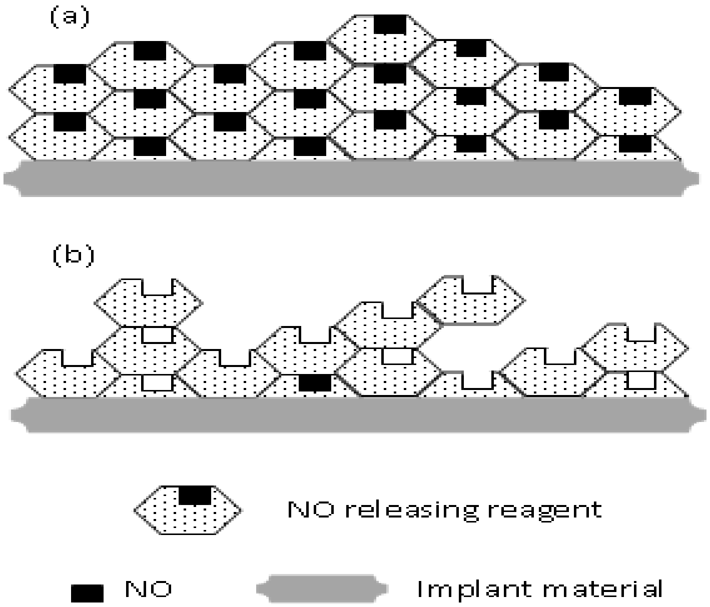

Figure 2: A schematic representation of the depletion of NO source in a multilayer release coating; a) at the initial stages, b) depletion over time.

Nitric oxide and nitric oxide synthase

Three NOS isoenzymes have been identified in mammals: inducible (iNOS/NOS-2), neuronal (nNOS/ NOS-1), and endothelial (eNOS or NOS-3) [21]. As illustrated in Figure 3, NOS convert L-arginine to citrulline and nitric oxide (NO) using nicotinamide adenine dinucleotide phosphate (NADPH) as the reducing equivalent and oxygen [22-25].

The complete primary sequence for NOS [26] consists of an oxygenase domain (N-terminus) and a reductase domain (C-terminus) with a linker having a calmodulin (CaM) binding sequence [21]. Electron equivalents are transferred from the reductase domain to the oxygenase domain where oxygen activation takes place. Following cofactors take part in this transfer.

Flavin adenine dinucleotide (FAD) → Flavin mononucleotide (FMN) → heme → O_2

Functional NOSs are dimeric; Cofactors FAD and FMN in the reductase domain of one functional monomer transfers the electrons to the heme cofactor at the oxygenase domain of the other functional monomer. Calcium ion (Ca^{2+}) dependant calmodulin acts as an activator switch for the transfer of the electrons from FMN to heme in nNOS and eNOS but iNOS is independent of the Ca^{2+}, likely due to its inherently tightly-bound CaM [27].

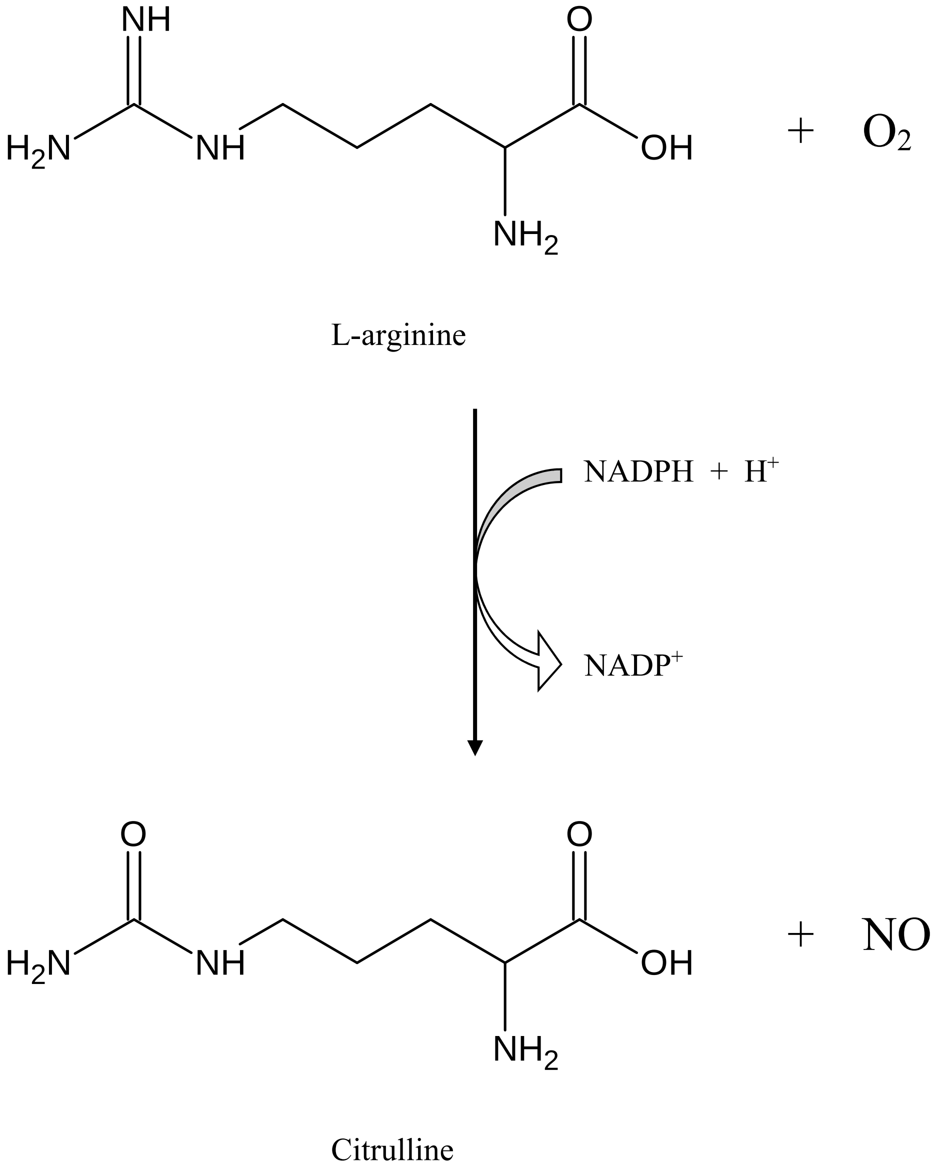

Figure 3: A schematic representation of the general reaction catalyzed by NOS.

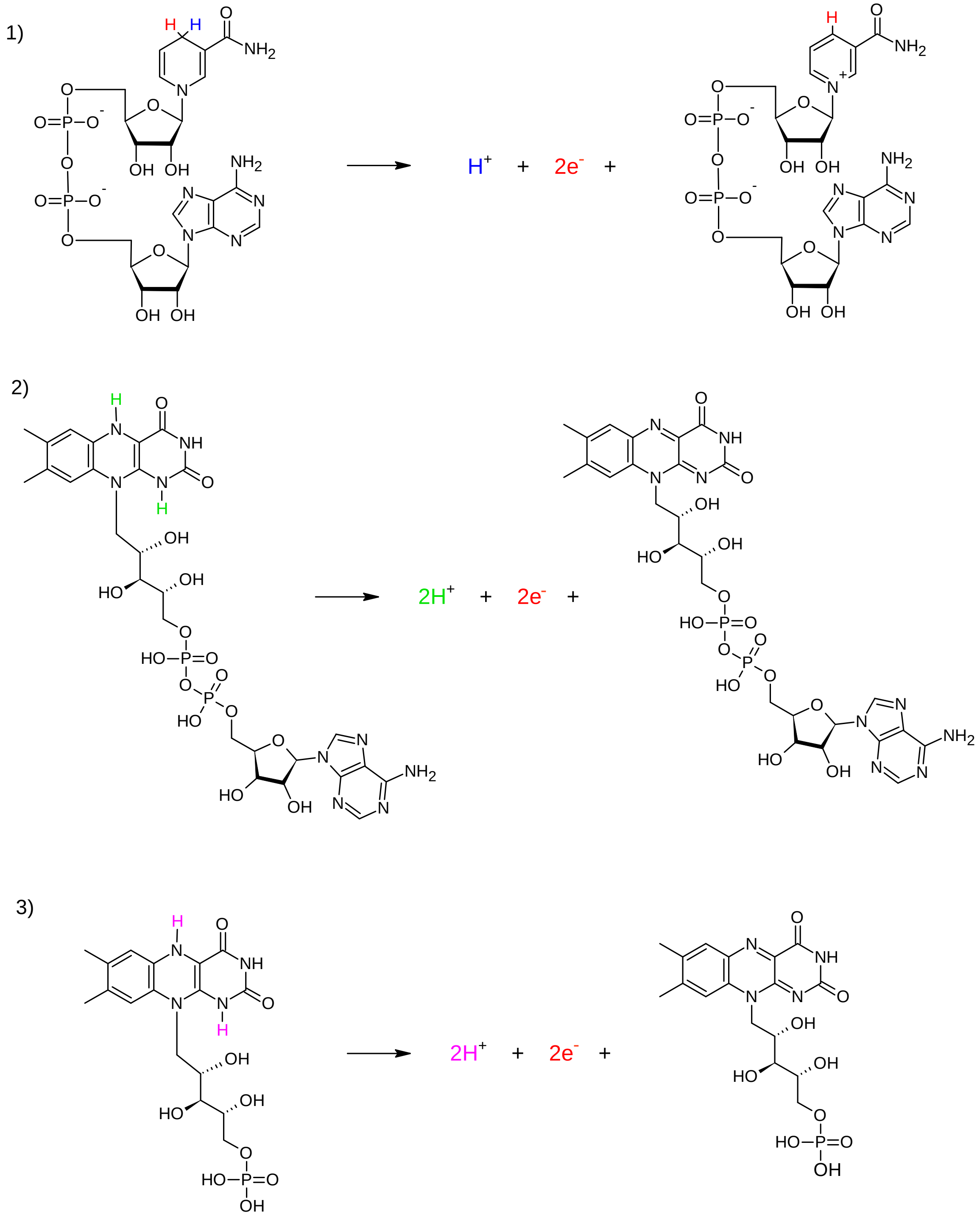

Figure 4: Reaction sequence in the reductase domain for the electron shunt; 1) NADPH$_2$ to NADP, 2) FADH$_2$ to FAD, 3) FMNH$_2$ to FMN.

Mechanism of nitric oxide mediated antithrombogenesis

The diffusion of NO into platelets stimulate guanylyl cyclase to produce cGMP that in-turn lowers cytosolic Ca^{2+} concentration by the inhibition of gated Ca^{2+} channels [28]. Upon activation, calcium concentration in intracellular space of platelets rise from its resting levels that triggers the cascade leading to platelet aggregation [29]. In the presence of guanylyl cyclase inhibitors, the platelet aggregation increases significantly, providing evidence to the regulatory function of NO on both cGMP and cGMP-dependant protein kinases [30-33]. For fibrinogen binding, one of the essential requirements is the conformational change of glycoprotein IIb/IIIa. The deactivation of phosphoinositide 3-kinase suppresses this conformational change, resulting in fibrinogen binding [34], halting the thrombosis cascade. Elevated levels of cAMP have also been linked to the decline in levels of intracellular Ca^{2+} [35, 36]. NO-induced cGMP production could also suppress protein kinase C, which in turn regulates surface expression of P-selectin, a mediator of platelet adhesion [37].

Electrostatically adsorbed thin films of NOS enzyme

In our previous work published, we showed that, NO-based antithrombogenic regimens that use blood-contacting LbL immobilized thin NOS enzyme films are better than direct NO-release mechanisms in counteracting coagulation [38]. Adsorbed LbL onto the surface as thin films, NOS catalyzes the conversion of substrate L-arginine to citrulline and NO as shown in Figure 4.

Charge-based LbL adsorption of thin film components for biocompatible applications have been widely explored [17, 18, 39, 40]. Here, the enzyme protein used is a negatively charged polyelectrolyte in solution. Using this solution the enzyme is adsorbed onto the positively charged matrix layer, polyethylenimine (PEI). Figure 5 and 6 are depictions of the LbL concept as applicable to a single layer each of both matrix and active component.

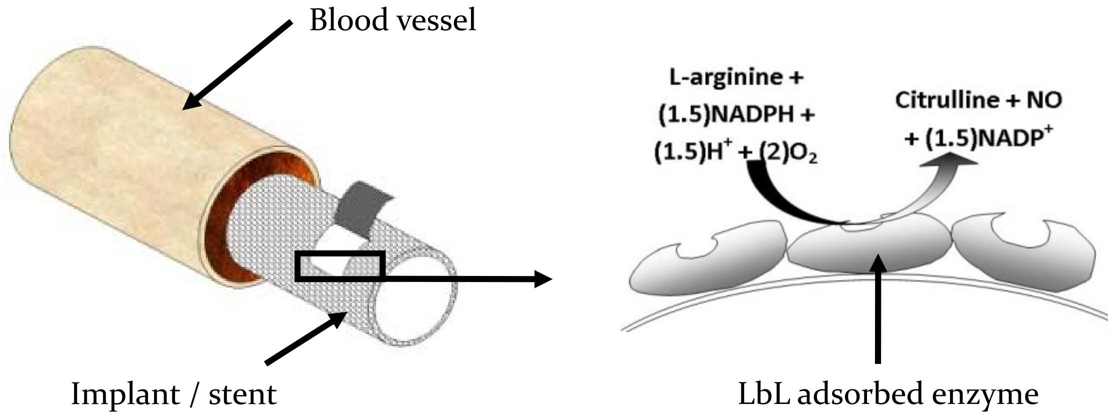

Figure 5: A schematic representation of a cross section of the LbL adsorbed monolayer of NOS. Enzyme converts substrate to NO. Hence a NOS immobilized implant displays intrinsic antithrombogenic activity.

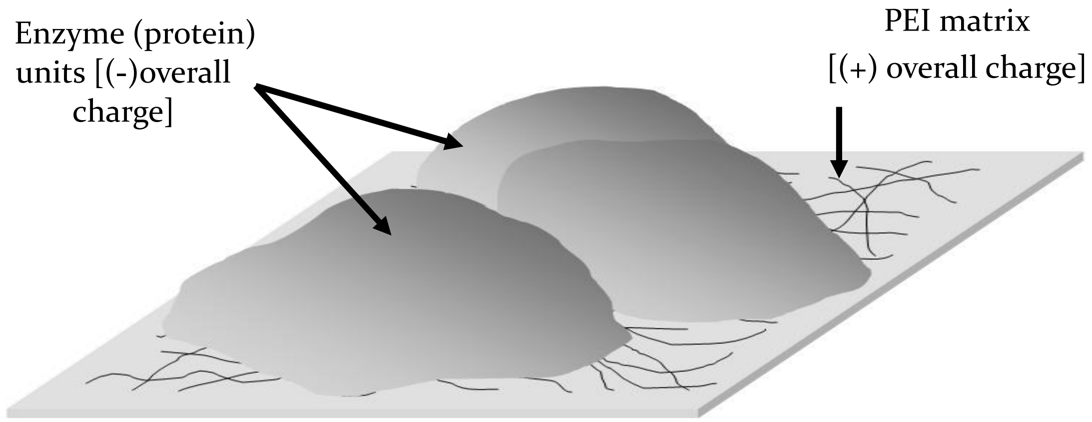

Figure 6: A schematic representation of the LbL adsorbed monolayers of (-) charged enzyme protein onto (+) charged polymer matrix layer on surface.

NOS embedded electrospun scaffolds

Inserts that demonstrate regenerative potential has been a recent area of thrust in regenerative medicine. Scaffolds fabricated from synthetic material have been in use for different applications from stem cell based transplantable artificial organs grown in laboratory to drug delivery systems fabricated for pharmaceutical purposes. Electrospun fiber scaffolds are known to closely resemble the extracellular matrix with the porosity and ultra-thin fiber arrangements [41, 42]. A greater control over the tissue organization can be achieved with electrospun fiber scaffolds and allows various functional modifications [43-46].

Similar to all implantable material, scaffolds and mats are prone to the thrombosis cascade on their surfaces and hence need a mechanism of antithrombogenesis. In this work, we explore the use of functional iNOS embedded in electrospun fiber scaffolds as a catalytic source of NO release for potential antithrombogenic action. Figure 7 is a schematic representation of a porous microfiber with an encapsulated ‘node’ containing an active component such as NOS. The porosity allows substrates and co-factors access to the enzyme and allows NO release/diffusion.

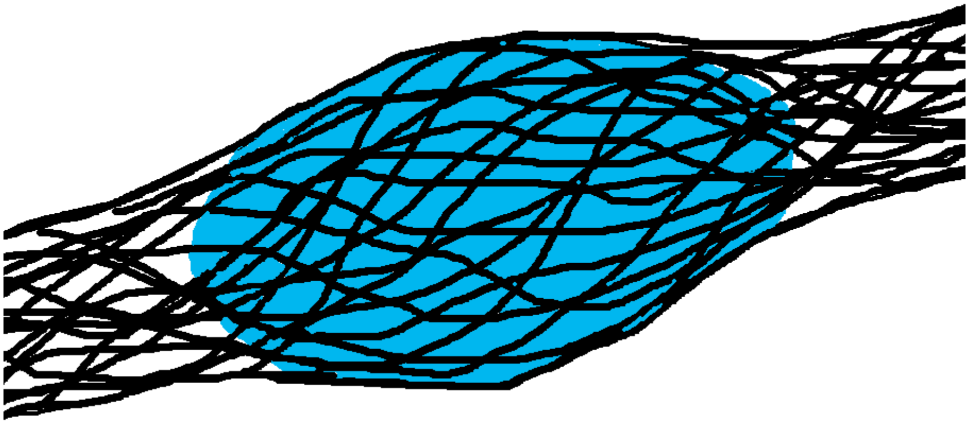

Figure 7: A schematic representation of an embedded aqueous ‘node’ in an electrospun scaffold microfiber.

NO as a short-lived reactive species and its significance in localized activity

As a gaseous molecule, nitric oxide is known to have a half-life ranging from 6-30 seconds [47]. However, nitric oxide does not have the ability to act as a circulating humoral species under physiological conditions[48], because plasma hemoglobin (Hb) and erythrocyte-based Hb scavenge NO rapidly [49]. NO flux resulting from an active NO-releasing regimen of a modified medical implant is localized. In blood vessels, the NO flux has to also compete with both the flow and scavengers in the blood plasma to maintain a useful threshold level of NO in the local environment. Therefore it is reasonable to assume that antithrombogenic activity of thin film coatings or drug-eluting scaffolds depend on their ability to produce NO at a rate that compensates for the loss.

CHAPTER I: IMPROVED ENZYME LOADING IN LAYER-BY-LAYER (LbL) ADSORBED THIN FILMS OF INDUCIBLE NITRIC OXIDE SYNTHASE (iNOS) AND POLYETHYLENIMINE (PEI)

1.1 Introduction

This chapter describes the enzyme loading and activity of NOS enzyme in LbL thin films. Our aim is to explore ways to increase the amount of enzyme loaded onto the active layer. NO production is known both to inhibit platelet adhesion and to restore blood flow [50]. Stimulated human endothelial cells are known to produce NO flux of 400 $pmol.cm^{-1}.min^{-1}$ [51]. Our previous work accomplished this by exposing enzyme substrate to an LbL deposited thin film consisting of multiple alternating iNOS and PEI layers. In this work, we report comparable fluxes, achieved by an iNOSoxy monolayer immobilized on a monolayer of PEI matrix. The catalytic turnover of substrate to NO is proportional to the number of active enzyme units that are exposed to substrate molecules on the surface by the modified surface. In the current work we explore methods to enhance enzyme loading onto the outermost layer of LbL film of PEI/NOS. The pH at which the immobilization takes place is expected to modulate the amount of NOS adsorbed. The Isoelectric point of the enzyme plays a major role in deciding the correct pH of the buffer from which the enzyme is adsorbed onto the thin film.

1.1.1 Isoelectric point of iNOS and its significance

The isoelectric point of mouse iNOS is 7.76 while for iNOSoxy domain it is 6.11 [52-54]. This implies that iNOSoxy protein used, carries an overall positive charge in solution below pH 6.11. In contrast, at higher pH values of the solution, the protein has an overall negative charge. We used two different pH's, both above 6.11 which ensure the protein is negatively charged, to study the levels of enzyme loading as a function of pH. To this end, we used adjusted values of pH 8.6 and 7.0 for sample iNOSoxy immobilizations. We avoided using pH in excess of 9.0, based on our preliminary findings that showed enzyme denaturation effects with significantly low enzyme activity. The control experiments used surfaces with only PEI immobilized. Similar work on pH-dependant immobilization of proteins as functional thin films have been reported in various other contexts [55].

1.2 Experimental

1.2.1 Expression and purification of iNOSoxy through recombinant plasmid DNA

Mouse iNOS oxygenase (iNOSoxy) domain template transgene in pCWori vector plasmid transformed into BL21(DE3) ampicillin-resistant E. coli. strain has been used for the protein expression (received from the Dennis Stuehr Laboratory at the Lerner Research Institute, Cleveland Clinic, Cleveland, OH, USA). Glycerol stocks were prepared and were stored at -80°C for continued use. Volumes of 150 μl of glycerol stock were inoculated into twelve aliquots of 2.00 ml each of lysogeny broth (LB), with 500 μl of ampicillin (Amp-100: 100 $\mu g.ml^{-1}$) added to each, to start a new batch. These were allowed to grow overnight at 37°C. Simultaneously, six volumes of 450 ml each of terrific broth (TB) and 300 ml of 100 mM phosphate buffer were autoclaved. Volumes of 50 ml each of phosphate buffer were added to each 450 ml of TB media to make the total volume 500 ml in each of the 2L culture flasks. Overnight LB cultures were added to the flasks and allowed to grow with 250 rpm shaking at 37°C. Readings for optical density at 600nm were then taken hourly, until an OD value of 0.8 was reached. At this point protein synthesis was induced by adding 500 μl of Isopropyl-β-D-1-thiogalactopyranoside (IPTG) together with 500 μl of heme-precursor, δ-aminolevulinic (δ-Ala). The induced culture was allowed to grow 48-60 hours. Cells were harvested by pelleting growth media at 4,000 rpm centrifugation at 4°C for 30 minutes. The re-suspension of this pellets used 10 ml volumes of pH 7.6 LB media to which were added 100 μl of lysozyme, 100 μl of phenylmethanesulfonylfluoride (PMSF) in dimethyl sulfoxide (DMSO), 500 μl Protease inhibitor cocktail III (4-(2-Aminoethyl) benzenesulfonyl fluoride hydrochloride, aprotinin, leupeptin, pepstatin A, bestatin, and L-3-trans-Carboxyoxiran-2-carbonyl)-L-leucyl-agmatine), EMD Chemicals, Inc., Gibbstown, NJ), 1 µl of DNase, and 10 µl of 1 M $MgCl_2$. The resuspended cells were lysed by sonication at 20 cycles each with 15 second 'on' and 45 second 'off' timing, while the cell containing vials were being kept on ice. The light brown colored resuspended pellet turned light pink indicating protein in the solution. Lysed cellular residue were separated from the protein cocktail in solution by centrifugation at 12,000 rpm through 30 minutes at 4°C. Protein in the lysate of the resultant supernatant was carefully collected. The dissolved protein was salted-out to precipitate by adding a combined mass to the ratio of 0.3 g of ammonium sulfate ($(NH_4)_2SO_{4(s)}$) per 1 ml of solution over a period of approximately one hour while being stirred on ice. The precipitate was separated from the supernatant by centrifugation at 10,000 rpm through 30 minutes at 4°C. We stored the precipitated protein overnight and also confirmed its viability through several weeks of storage.

The pellet saved at -80°C was re-suspended in base buffer to which 100 µl of PMSF in DMSO and 100 µl of Protease inhibitor cocktail III were added. Resuspensions were ultra-centrifuged at 10,000 rpm to further remove particulate debris that could clog the affinity column. In a cold room maintained at 4°C, a newly packed affinity column [56, 57] of Ni-NTA superflow® (Qiagen Inc., CA) with a dead volume of 10 cm^3 was charged with 50 mM $NiSO_4$ charge buffer followed by binding buffer. Once the protein suspension was loaded, the Tris binding buffer followed by wash buffer were run through the column. Finally, the elution buffer (200 mM imidazole) was used to detach and elute iNOSoxy, observed by the gradual movement of reddish-brown colored band in the column. The enzyme was collected in approx 0.5 ml aliquots in cryogenic vials. The used column was stored in 25% ethanol after stripping. The protein aliquots were dialyzed in batches in 500 ml base buffer to which 200 µl β-mercaptoethanol was added. The enzyme containing dialysis bags were transferred to fresh dialysis solution twice. The concentrated protein aliquots were spot-frozen in cryogenic vials using liquid nitrogen before being stored at -80°C. Concentration of protein in solution was determined for each batch before each characterization method, using the bathochromic shift of the Soret band for the p-450 type enzyme [58].

1.2.2 Adjustment of pH of protein in solution

Through a series of dilutions, a solution of ~12 µM NaOH(aq) was prepared. An aliquot of 100 µl of iNOSoxy was thawed on ice and was transferred into a Microcon® 3000 MWCO centrifugal filter vial. To this tube, an aliquot of 400 µl of ~12 µM NaOH(aq) was added. After vortexing for 3-5 seconds, the pH of the total aliquot was measured using an Accumet mini pH probe connected to an AB-15 pH meter (Fisher Scientific). The solution was centrifuged (in Beckman Coulter Microfuge-18 centrifuge) for 5 minutes at 14,000 rpm. After confirming approx. 4/5 in filtrate, the residual enzyme solution (approx. 100 µl) was kept on ice. This exchange sequence of the washing buffer was repeated three times before the final aliquot of pH adjusted enzyme solution was retrieved. Using the mini pH probe, the pH of the final 100 µl of enzyme aliquot was measured. Several aliquots of 100 µl each of pH adjusted enzyme solutions were made immediately before each investigation.

1.2.3 Atomic force microscopic (AFM) imaging of adsorbed thin films

We used Agilent Pico-SPM atomic force microscope, PicoView controller and Mac-mode module (Agilent Technologies Inc.). The scanner used in this imaging sequence was the multi-purpose macro scanner with a scan range of 90 µm in the x-y dimension and 7 µm in the z-dimension (Agilent Technologies Inc.). PointProbe® Plus AFM probe (NanoAndMore USA Inc., SC, USA) of 125 µm length, 30 µm width, 42 N/m spring constant, and 270 kHz resonant frequencies were used in Acoustic AC mode. AFM imaging was carried-out in a chamber at ambient conditions. We used grade ZYA highly oriented pyrolytic graphite (HOPG) (Structure Probe Inc., PA, USA) for immobilization of thin films. HOPG squares of 12 mm × 12 mm with 2 mm thickness were mounted on the sample plate. Freshly cleaved bare HOPG surface was scanned at different speeds for scan sizes ranging from 90 µm × 90 µm to focused scan sizes of 500 nm × 500 nm. Aliquots of 100 µl of 1.5 mg/ml PEI (Linear; MW 25,000 free base form; Polysciences Inc.) were added onto the surfaces. After an incubation time of 5 minutes, the surface was washed with DI water and dried in a nitrogen stream. Scan sizes ranging from 50 µm × 50 µm to 500 nm × 500 nm were obtained. Aliquots of 50 µl of iNOSoxy adjusted to pH 7.0 or 8.6 were added onto the PEI layer. After incubation for 5-10 minutes, the surface was washed with EPPS buffer and dried using a nitrogen stream. AFM scans were performed for scan areas ranging from 50 µm × 50 µm down to 500 nm × 500 nm.

1.2.4 Electrochemical investigation of heme-Fe^{3+} reduction and catalytic NO reduction by LbL immobilized PEI/iNOSoxy films on graphite electrodes

We used an in-house purging system for making saturated NO in aqueous solution. Nitric oxide (Praxair) was first purged through an oxygen-scrubbing alkaline pyrogallol solution (1:4 v/v 250 $mg.ml^{-1}$ pyrogallol: 1 $g.ml^{-1}$ KOH). The resultant NO stream was then purged through a saturated KOH solution for further removal of gaseous oxides. The resultant pure NO gas stream was bubbled into 10 ml of DI water in a sealed scintillation vial. Using a Griess assay calibration curve, the concentration of saturated aqueous NO (2.0 mM) was established before each experiment for a separately purged saturated NO (NO_2^-) solution.

We prepared graphite electrodes in-house following established methods [59]. The electrodes were first polished using a rotating polishing pad. Then the discs were polished using 0.3 μm and then with 0.05 μm size alumina with intermittent washings with water. Each disc was sonicated in a water bath for 30 sec and dried in a stream of nitrogen gas. Aliquots of 5 μl each of 1.5 mg/ml PEI solution (Linear; MW 25,000 free base form; Polysciences Inc.) were added onto the polished surfaces of each of the discs. After a 10 minute incubation time, the electrodes were washed using DI water before drying in a stream of nitrogen gas. Aliquots of 5 μl each of pH 7.0 and pH 8.6 enzyme solutions were added on top of PEI-immobilized electrode surfaces. After a 15-20 minute incubation time, the electrodes were washed with DI water and dried using a nitrogen gas stream. A typical series of experiment uses five electrodes for enzyme immobilization, which we test side by side for films prepared at pH 7.0 and pH 8.6 respectively. Three electrodes with only PEI were used as the control experiment.

We used multi-necked electrochemical cells (Ace Glass). The working electrode is the PEI/iNOSoxy modified PG electrode. We used Ag/AgCl as the reference electrode and a platinum wire as an auxiliary electrode in 10.0 ml solution of the phosphate buffer. The buffer was de-gased first for 30 minutes using a slow nitrogen gas flow. A nitrogen blanket was maintained throughout the experiment. As the first step for all the electrodes, we observed their current as a response to a linear sweep of potential in the absence of NO substrate. Blank cyclic voltammetric scans are run to confirm the absence of interfering catalytic currents for the reduction of nitrite derived from traces of NO_x in solution. Small aliquots of 2.0 mM NO were injected to the buffer solution using an airtight Hamilton syringe. The NO concentration in buffer increased roughly by 20 μM increments. After each injection, the solution was stirred using a magnetic stirrer before the beginning of voltammetric scans.

1.2.5 Fourier Transform Infrared Spectroscopy (FTIR) on thin protein layers

We used attenuated total reflection (ATR) configuration in FTIR analysis to investigate thin protein films. A diamond ATR crystal assembly (PIKE technologies) was used with a Varian Digilab Scimitar series FTS 2000 FTIR. An aliquot of 100 μl of 1.5 mg/ml PEI (MW 25,000; Polysciences Inc.) was placed on the clean crystal. Using a plastic microscope cover-slip the drop was smeared to cover the crystal. This was collected as the blank reading. Evaporation of the water of the smear resulted in the PEI film on the crystal, which we dried with a nitrogen gas stream using a portable nitrogen purge system. An aliquot of 100 µl of enzyme solution adjusted at the desired pH was placed on the dry PEI layer. After an incubation time of 15 minutes, the crystal was washed gently with DI water. The resulting surface was dried under a slow nitrogen gas stream while obtaining IR readings. The final IR reading was obtained for the immobilized layer after adding an aliquot of 100 µl of EPPS buffer and resuspending the immobilized layer.

1.2.6 Griess assay for the determination of activity of thin films of PEI/iNOSoxy

Cylindrical discs were drilled-out from a block of high grade graphite using a hole-saw type drill-bit. The discs were first polished using the same protocol described earlier (section 1.2.4) for regular electrodes. Diameter of each disc was measured using a Vernier caliper. Diameters are in the range of 7.27-7.35 mm for the seven discs used. Aliquots of 50 µl each of 1.5 mg/ml PEI solution (MW 25,000, Polysciences Inc.) were added onto the polished surfaces of each disc. After a 5 minute incubation time, the disc surfaces were thoroughly washed with DI water and were dried in a gentle nitrogen stream. Aliquots of 25 µl each of pH 7.0 enzyme solution were added on top of three PEI-modified disc surfaces. Aliquots of 25 µl each of pH 8.6 enzyme solution were added on top of the other three PEI-modified discs. One PEI modified disc was used as a control. Surfaces were incubated for 15-20 minutes with the solutions of enzyme adjusted at the desired pH. After incubation, the disc surfaces were thoroughly washed with DI water and dried in a gentle nitrogen stream. All discs were placed in labeled vials with the modified surface faced up.

Volumes of 5 ml of the reaction cocktail containing 250 µM N-hydroxy-L-arginine (NHA), 10 µM tetrahydrobiopterin (H_4B), and 400 µM dithiothreitol (DTT) prepared in 100 mM phosphate buffer and adjusted to pH 7.4 were added to each of the vials. The reaction was triggered by adding hydrogen peroxide to a final concentration of 150 mM at 37˚C. Aliquots of 100 µl of reaction media were drawn at 2, 4, 8, 12, 24, 48 & 72 hour lapse times, and were combined with 100 µl of each of Griess reagents R1 (sulfanilamide) and R2 (N-(1-naphthyl)ethylenediamaine) (Cayman chemical company, Ann Arbor, MI, USA) [60]. Spectrophotometric absorbance values for 540 nm against the reagent blank were recorded (UV-Vis; Model 8543, Agilent Technologies) after a 10 minute reaction time for all aliquots. A standard calibration series was prepared and the readings were plotted.

1.3 Results and discussion

1.3.1 AFM images of iNOSoxy on PEI-modified surfaces

Figure 8 shows topology of both the bare HOPG surface and PEI-modified HOPG surface. Figure 8(a) shows the typical steps characteristic of a HOPG surface. Figure 8(b) shows the AFM image of PEI immobilized on HOPG, and shows the arrangement of the polymer aggregates on the surface. Figure 9 shows representative topological images of PEI/iNOSoxy.

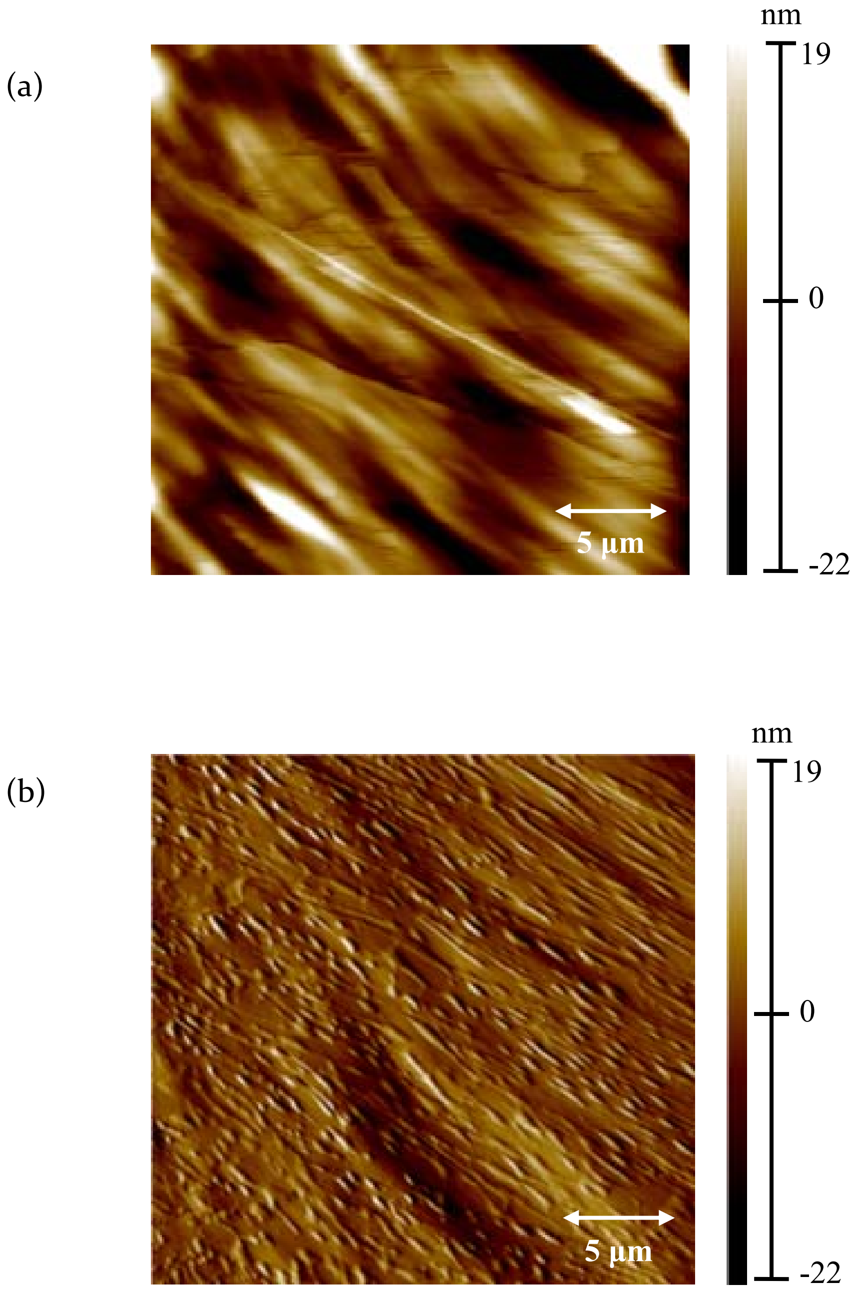

Figure 8: AFM images on the topology of the bare and PEI matrix adsorbed surfaces; a) Bare HOPG (scan size 25 µm × 25 µm), b) PEI immobilized on HOPG for 5min (Scan size: 25 µm × 25 µm).

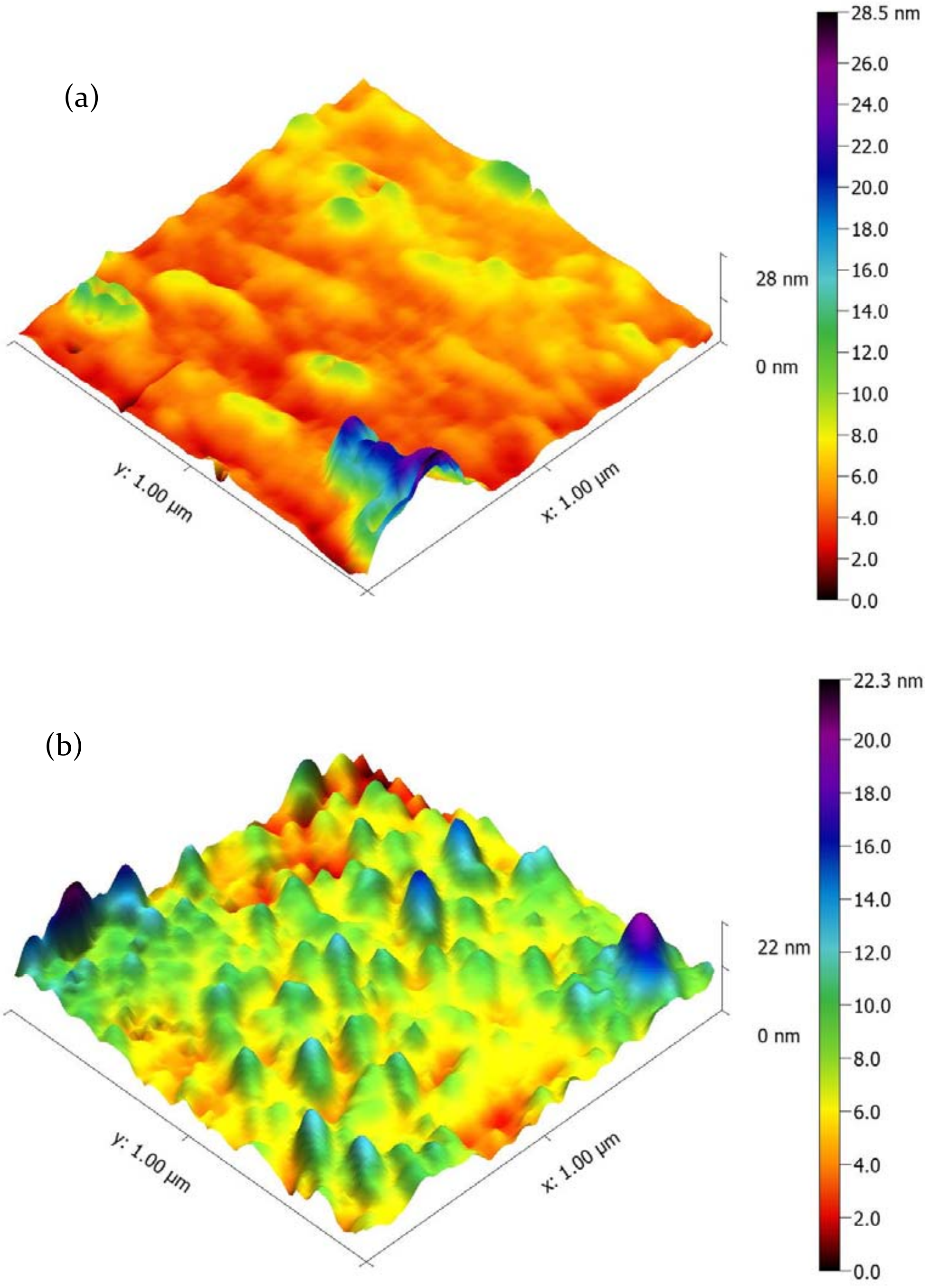

Figure 9: AFM images with a 3-D perspective of the topology of the outermost layer in iNOSoxy immobilization on PEI; a) Outermost iNOSoxy layer immobilized at pH 7.0

(Scan size: 1 µm × 1 µm), b) Outermost iNOSoxy layer immobilized at pH 8.6 (Scan size: 1 µm × 1 µm).

Analysis of the prominent features in the 10-160 nm diameter range shows higher density of protein clusters for PEI/iNOSoxy films made at pH 8.6 compared to films made from pH 7.0 iNOSoxy solution. Figure 10 shows the comparative counts of the number of protein clusters in various diameter ranges for films prepared from iNOSoxy at pH 7.0 and pH 8.6.

An increased pH beyond the isoelectric point of iNOSoxy brings about a higher negative charge density for iNOSoxy in the solution which drives higher electrostatic loading of iNOSoxy on the positively charged PEI matrix. Lower pH values lead to less attachment to the positively charged PEI film. AFM imaging and cluster density analysis is consistent with higher enzyme loading at pH 8.6 compared to pH 7.0.

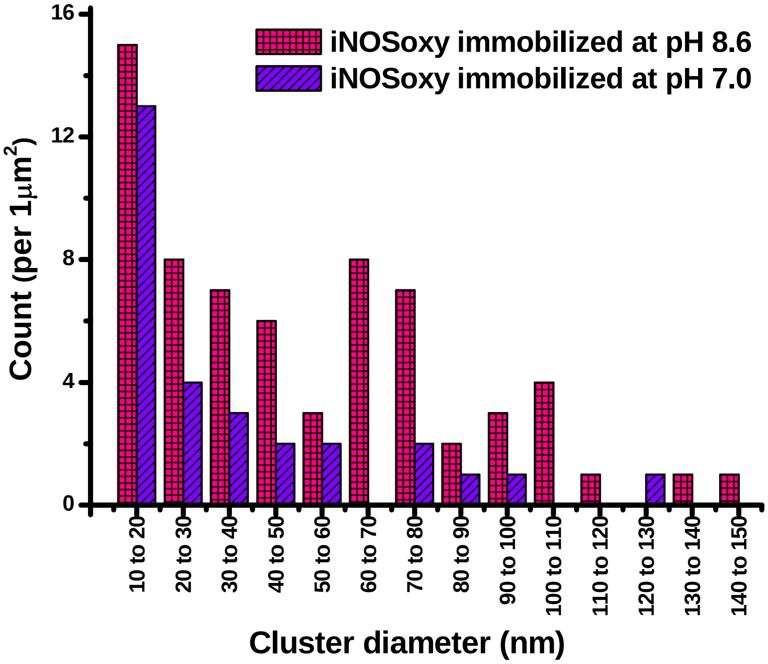

Figure 10: Histogram of cluster abundance in various diameter ranges for pH 8.6 and pH 7.0 PEI/iNOSoxy films.

1.3.2 Electrocatalytic reduction of NO mediated by iNOSoxy in films

Electrochemical analyses using iNOSoxy/PEI immobilized on electrode surfaces as working electrodes provided two aspects of information. In the absence of substrate NO, the redox active Fe^{3+}-heme of iNOSoxy was used to monitor the overall amount of iNOSoxy adsorbed in the two sets of films. Integration of the voltammetric current provides the faradaic charge passed, which indicates the amount of iNOSoxy present in the film. The enzyme iNOSoxy is also known to catalyze the electrochemical reduction NO [61]. Therefore, in the second component of electrochemical characterization, we used this metalloprotein-dependent catalytic reduction as a handle to compare and contrast activity of iNOSoxy in the thin layers.

Figure 11 is a typical cyclic voltammogram for the specific window that shows the Fe^{3+}/Fe^{2+} and Fe^{2+}/Fe^{+} redox couples by a heme moiety, iNOSoxy in this particular case. In this control experiment the NO substrate is absent.

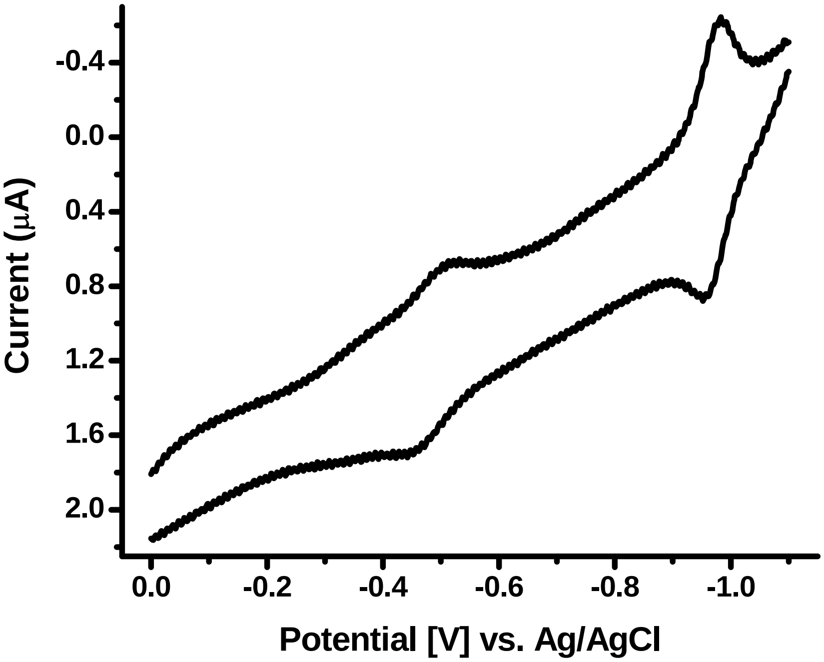

Figure 11: Typical cyclic voltammogram showing Fe^{3+}/Fe^{2+} (approx. 500mV) and Fe^{2+}/Fe^{+} (approx. 950mV) redox couples for the heme moieties in an iNOSoxy immobilized electrode. The effect of Ohmic drop has been removed by mathematically treating the original voltammogram.

1.3.2.1 iNOSoxy-heme Fe^{3+} reduction as a quantifier of immobilization

Integrals of voltammograms for Fe^{3+}-heme reduction obtained at 8mV/s scan rate linear sweep show higher faradaic charge transfer by electrodes modified with PEI/iNOSoxy films where iNOSoxy solution maintained pH at 8.6 during immobilization. PEI/iNOSoxy modified electrodes where immobilization of iNOSoxy solution maintained pH at 7.0 show lower faradaic charge transfer. Figure 12 is a typical comparison of integrals for a single electrode. Here the same electrode modified at pH 8.6 has more active sites per unit surface area compared to pH 7.0.

In average, we find that films constructed using pH 8.6 iNOSoxy solution exhibit close to 4x the amount of charge compared to films constructed using pH 7.0 iNOSoxy solution (55 nC for pH 8.6 versus 14 nC for pH 7.0) as shown in Figure 13. This translates to an average of 0.57 pmol of iNOSoxy adsorbed in films constructed at pH 8.6 compared to 0.15 pmol of iNOSoxy in films formed at pH 7.0.

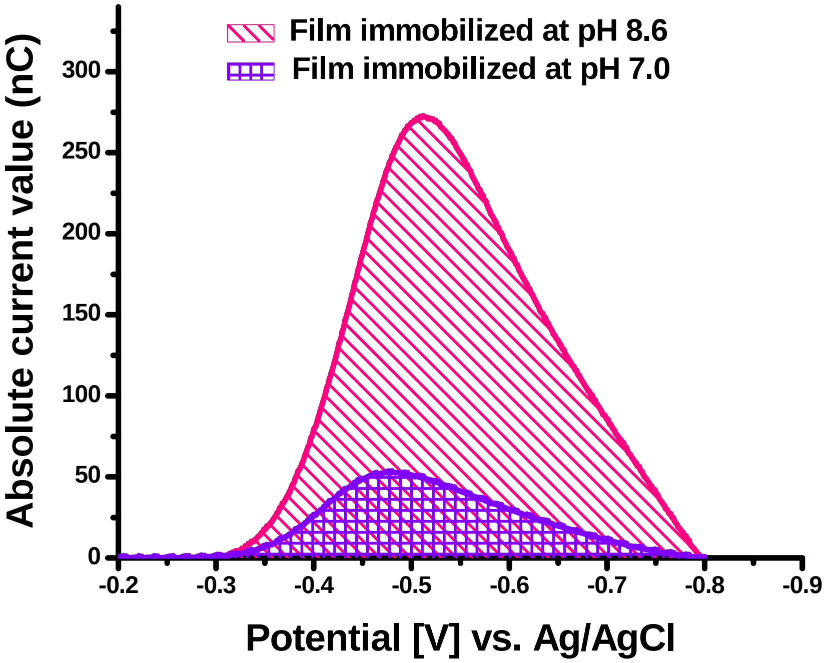

Figure 12: Integrals of characteristic Fe^{3+} reduction in 8mV.s^{-1} linear sweep voltammograms for iNOSoxy/PEI films adsorbed from iNOSoxy solution at pH 8.6 and pH 7.0.

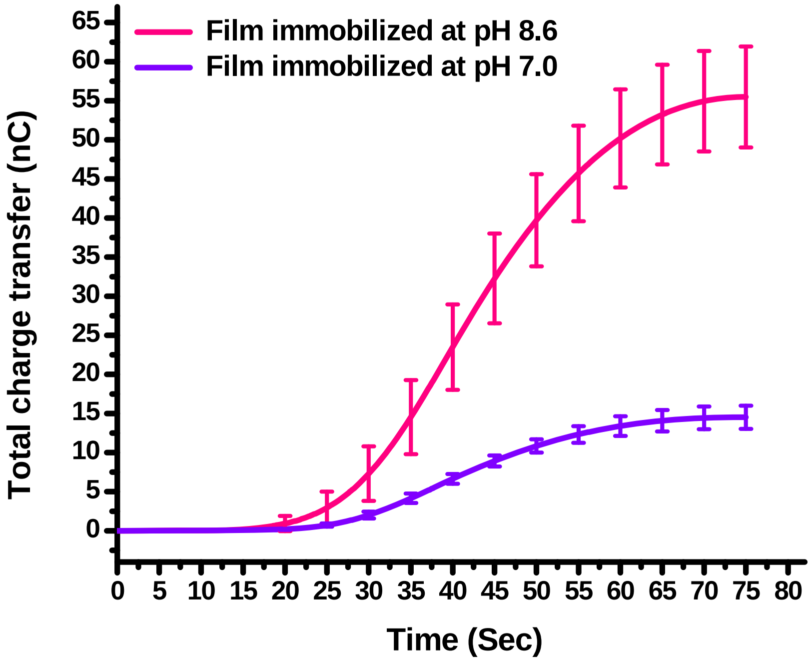

Figure 13: Average of integrals of the characteristic Fe^{3+} reduction in $8mV.s^{-1}$ linear sweep voltammograms showing different amounts of immobilization at different pH's. Standard deviation based on data for the same batch of electrodes immobilized at pH 8.6 and 7.0 (N=5).

1.3.2.2 Catalytic reduction of NO mediated by iNOSoxy on PEI/iNOSoxy films on PG electrodes

Addition of NO substrate to the solution results in a catalytic peak around -0.9V vs. Ag/AgCl. As expected based on previous studies [38, 61], the catalytic current is proportional to NO concentration. Figure 14 shows the peaks of nitric oxide catalytic reduction mediated by iNOSoxy for pH 8.6 and pH 7.0 films.

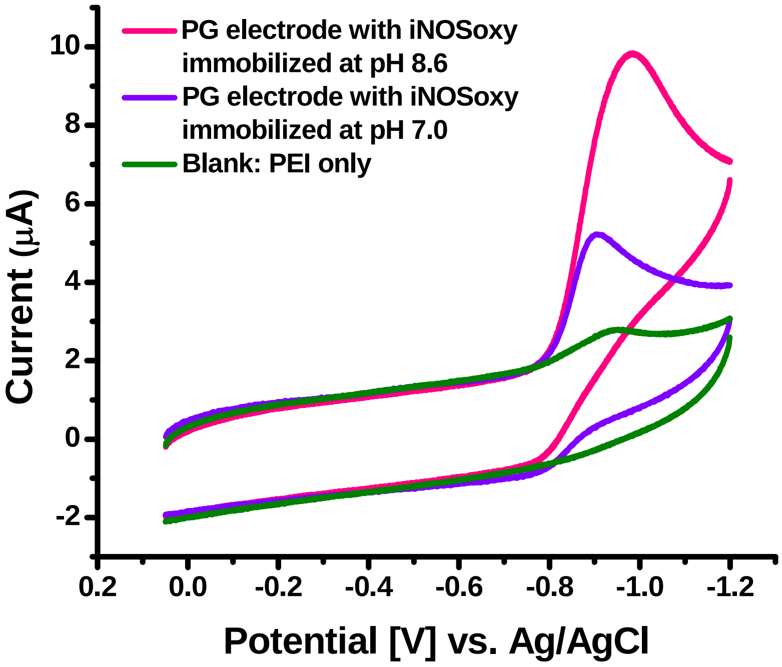

Figure 14: Cyclic voltammogram (200mV.s^{-1}) for catalytic NO reduction by different amounts of iNOSoxy immobilized at different pH's measured at the same NO concentration (120 µM).

In the electrostatic adsorption of iNOSoxy/PEI, the number of iNOSoxy units adsorbed and hence the number of electron transfer sites on PG electrodes is higher when enzymes are immobilized at pH 8.6 than immobilized at pH 7.0. Figure 14 is a comparison of peak catalytic currents (I_{PC}) for NO reduction by iNOSoxy immobilized electrodes. I_{PC} follows a ratio of 1:2 between pH 7.0 immobilization and pH 8.6 immobilization for each NO concentration. For example, in Figure 14, I_{PC} value for pH 7.0 immobilization and pH 8.6 immobilization are 5.2 μA and 9.8 μA respectively for 120 μM NO concentration.

1.3.2.3 Michaelis-Menten kinetics

The rate of an enzyme-catalyzed reaction is given as V in the Michaelis-Menten model where;

$$\mathrm{V} = \frac{\mathrm{V_{Max}} \times [\mathrm{S}]}{\mathrm{k_M} + [\mathrm{S}]} \tag{1.1}$$

V_{Max} is the maximum rate at which substrate turnover takes place, k_M is the substrate concentration at half maximum of the rate of reaction (also known as the Michaelis constant), and, k_{cat} is the turnover number. The corresponding electrochemical version of the Michaelis-Menten equation is as follows;

$$\mathrm{I_{cat}} = \frac{\mathrm{nFA\Gamma}k_{\mathrm{cat}} \times [\mathrm{S}]}{\mathrm{k_M} + [\mathrm{S}]} \tag{1.2}$$

where the rate of catalysis is represented by the catalytic current I_{cat}. In this equation, Γ is the active surface catalyst concentration, A is the electrode surface area, and F is the Faraday constant. The rearrangement allows the plotting of normalized catalytic current against nitric oxide concentration as shown in Figure 15, where typical enzyme saturation kinetics are observed.

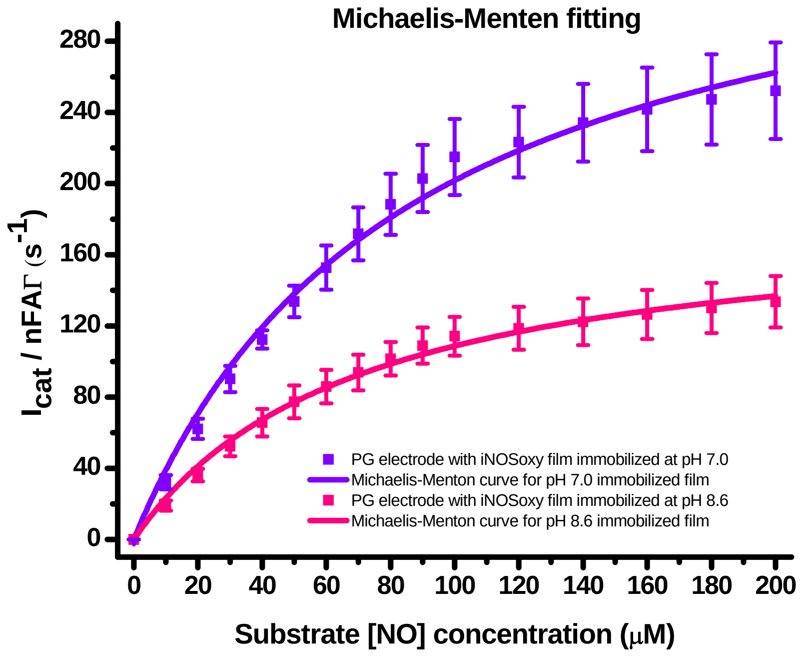

Figure 15: Average catalytic peak current for NO reduction at the surfaces of iNOSoxy/PEI modified electrodes prepared at pH 7.0 and pH 8.6. Standard deviation based on data for the same batch of electrodes immobilized at the respective pH’s (N=5).

iNOSoxy/PEI films grown at pH 7.0 show higher turnover rates of iNOSoxy-mediated NO reduction compared to films formed at pH 8.6. Non-linear fitting of observed traces using the Michaelis-Menten kinetic model yields the k_M and k_{cat} values for the two films.

pH of iNOSoxy at Immobilization	k_M (μM)	k_{cat} (s^{-1})
pH 8.6	69.6±4.8	184.4±5.3
pH 7.0	85.9±7.4	375.2±14.6

Table 1: Extracted Michaelis-Menten parameters from nonlinear regression fitting using Michaelis-Menten model.

According to the Michaelis-Menten parameters extracted from nonlinear fitting of experimental data, a marked difference of the rate of catalysis is observed between the two types of iNOSoxy films. Films immobilized at pH 7.0 exhibit higher catalytic turnovers compared to films immobilized at pH 8.6. The differences in the electrochemical turnover numbers for iNOSoxy-mediated NO catalytic reduction may be related to a pH-dependent structural change in the enzyme protein.

Dynamic motions which depend on structure of an enzyme protein are known to play a role in enzyme catalysis [62-65]. In our case, iNOSoxy electrostatically adsorbed at the two different pH's may adopt different active structures characterized by distinct catalytic properties. The structural distortion changes the dynamic motions of the enzyme as reported in literature [66-70]. The degree to which the pH potentially affected the iNOSoxy structure, and thus its catalytic properties may be explored in terms of close structural characterization of PEI/iNOSoxy films prepared at various pH's.

1.3.3 FTIR Characterization of PEI/iNOSoxy films prepared at various pH's

FTIR has been used as a tool to investigate conformational change on protein microenvironments [71, 72]. For example, works by Korkmaz-Ozkan and co-workers [71] on the outer membrane protein-G (Omp-G) of *E.Coli.,* discusses how similar pH-induced conformational changes can be monitored by FTIR. We looked closely at structural features of iNOSoxy/PEI thin films using FTIR spectroscopy. Amide I (1650 cm^{-1}) and amide II (1550 cm^{-1}) bands [73-75] provide good structural handles to monitor local changes in the tertiary structure [62-64]. Figure 16 and Figure 17 show the amide I and II envelopes of iNOSoxy on PEI in films formed at pH 7.0 and pH 8.6. The Figures also show the deconvolution of the amide bands into individual components contributing to the overall envelopes.

Deconvolution of amide I and amide II bands of iNOSoxy into different component peaks suggest different microenvironments of the enzyme when deposited at different pH. Solution pH is known to induce conformational changes in proteins [72, 76-78], and enzymes [68, 79]. Significant differences in both the wavenumber and in the intensity of component peaks are evident as shown in Figure 16 and Figure 17. The observed changes in both number of components and positions in amide I and II FTIR envelopes is probably the result of changes in the tertiary structure of iNOSoxy when adsorbed from solution at pH 8.6 as opposed to pH 7.0 [62-64].

Change of pH is expected to result in changes in intra-molecular hydrogen bonds and other bipolar interactions. This may drive distortions in the protein's 3D structure. pH-driven protein conformational changes are not new, and have been reported for several proteins [72, 76-78] and enzymes [71, 72, 80, 81]. Dirix and co-workers [82] have interpreted deconvolution of amide I FTIR envelope into six peaks and attributed them to structural components such as α & β helices, extended chains, turns and bends. The work of Baron [73] attributes deconvoluted FTIR peaks to secondary structures in a specific example where enzyme catalysis is explained. The close link of protein conformation and enzyme catalysis has been studied both in their native environments [68, 69] and in immobilized films [20, 78].

From our results, we find pH 7.0 immobilization to result in an iNOSoxy/PEI film with a higher rate of catalysis than films prepared at pH 8.6, despite high enzyme loading at pH 8.6. This suggests that immobilization at pH 7.0 brings about a three dimensional enzyme structure with high catalytic efficiency compared to enzyme units adsorbed at pH 8.6.

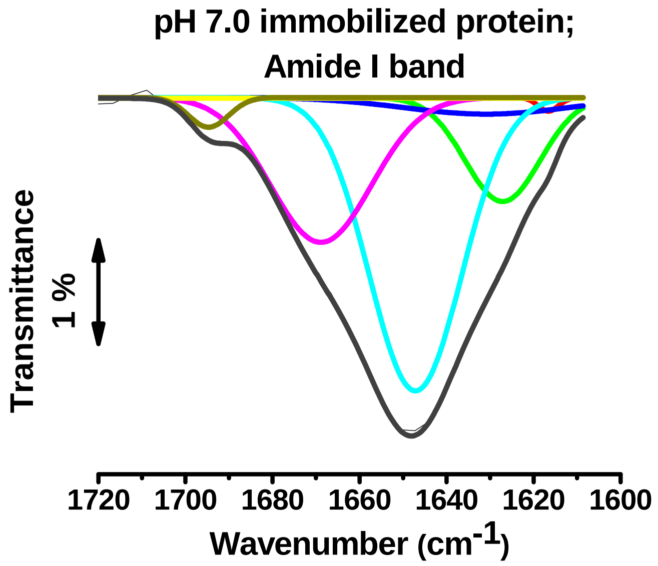

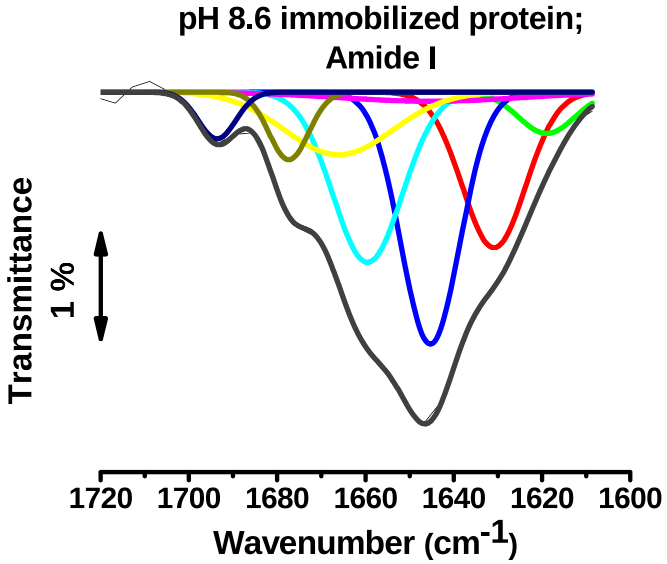

Figure 16: Deconvoluted Amide I bands for the envelope signals obtained at pH 7.0 and pH 8.6 immobilization.

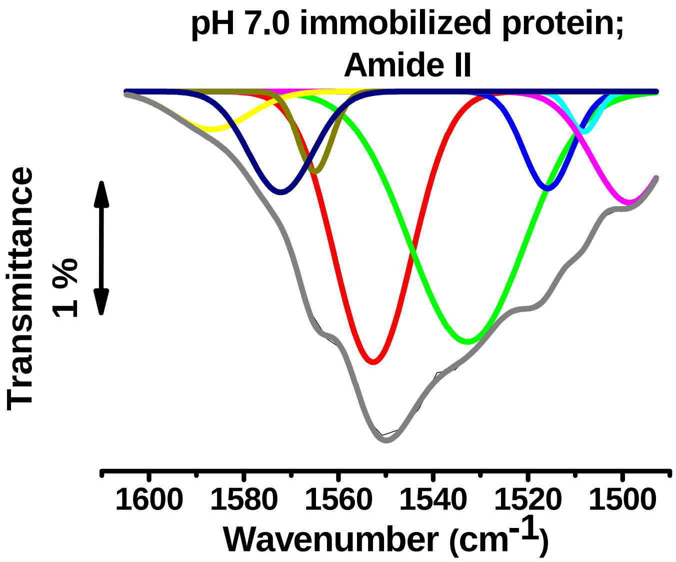

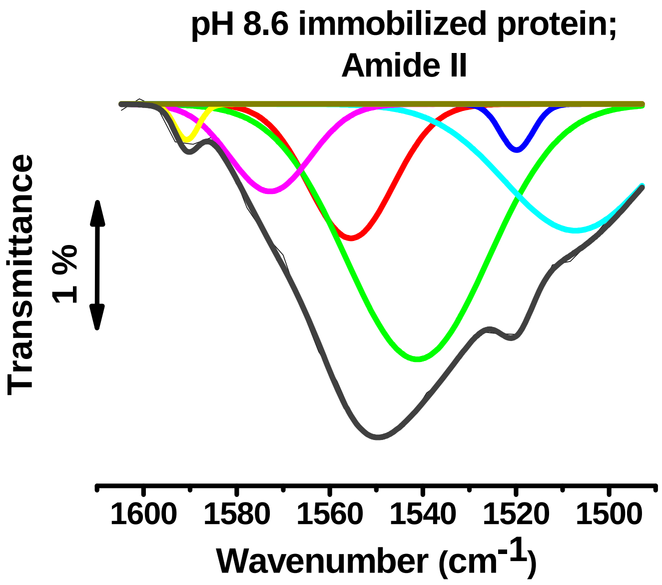

Figure 17: Deconvoluted Amide II bands for the envelope signals obtained at pH 7.0 and pH 8.6 immobilization.

1.3.4 Activity of iNOSoxy / PEI thin films

The ultimate test for iNOSoxy-based thin films is the catalytic synthesis of NO when ingredients of the NOS reaction are provided. We thus explored whether the NOS reaction in thin films is affected by the pH at which iNOSoxy is adsorbed onto PEI layer. To this end, we measured NO generated over time in a cocktail that contains the N-hydroxy-L-arginine as a substrate surrogate and all other ingredients of the NOS reaction [83, 84]. We followed NO synthesis in terms of nitrite accumulated in solution. In aqueous media the NOS reaction product, NO, converts to nitrite, and the latter is typically used as measure of NO formation [60]. Since the reaction cocktail contains all factors for the NOS catalytic turnover, the initiation of the reaction is the immersion of iNOSoxy-modified surfaces in the reaction cocktail. Figure 18 shows the graph of cumulative NO synthesis in the reaction cocktail measured from the time of immersion. NO accumulation is rapid in the beginning, and reaches a plateau after about 48 hours. For example, during the second two-hour window the cumulative NO concentration almost quadruples (approx. 0.5 to 2.1 μM for films immobilized at pH 7.0 and 1.3 to 4.5 μM for films immobilized at pH 8.6). In contrast, in the following four-hour window the cumulative NO concentration increases only to below twofold of the preceding value, eventually reaching a plateau after 48 hours. However, as evident from the same Figure, the average cumulative concentration at each sample interval resulting from pH 8.6 PEI/iNOSoxy film activity is two- to three-fold that of the average cumulative concentration resulting from activity of the pH 7.0 thin film. At 72 hours, thin layers immobilized at pH 8.6 resulted in nearly 60 nmol of NO released in solution, whereas thin layers immobilized at pH 7.0 resulted in just over 20 nmol of NO released.

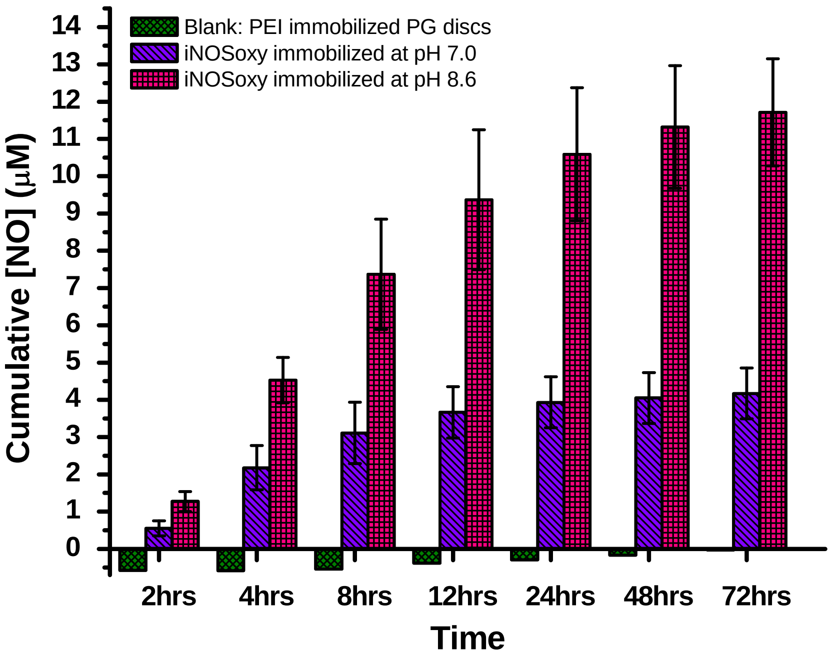

Figure 18: Average cumulative NO concentration for immobilization pH values, pH 7.0 & pH 8.6; Standard deviation shown where N=3 for each immobilization pH.

When converted to the average flux per unit surface area of the immobilized surfaces, our results show an initial burst of NO through the first 12 hours followed by a decline and then stable NO release up to the end of our observation window of 72 hours for all PEI/iNOSoxy surfaces regardless of pH of film formation (Figure 19). This two-phase NO release kinetics model has been previously reported [85, 86]. The initial burst is especially useful to counter early prosthetic graft occlusion and hence delay the requirement of surgical revision of synthetic grafts such as those used in hemodialysis [87]. The flux peaks at a 2-4 hour timeframe from the start of the reaction. The average peak NO flux values range from 386 $pmol.mm^{-2}$ for discs incubated using protein at pH 8.6 to 194 $pmol.mm^{-2}$ for discs incubated using protein at pH 7.0 in the same time window. For the two hour window considered, this translates to nearly 322 $pmol.cm^{-2}.min^{-1}$ for discs incubated using protein at pH 8.6 and to nearly 162 $pmol.cm^{-2}.min^{-1}$ for discs incubated using protein at pH 7.0. The NO flux resulting from the single enzyme layer immobilized at pH 8.6 comes close to the NO flux of stimulated human endothelial cells, at around 400 $pmol.cm^{-2}.min^{-1}$ [51]. Moreover, the average flux resulting from pH 7.0 immobilized films diminishes faster, while flux resulting from pH 8.6 immobilized films is sustained at a higher level of release up until the end of our observation window of 72 hours.

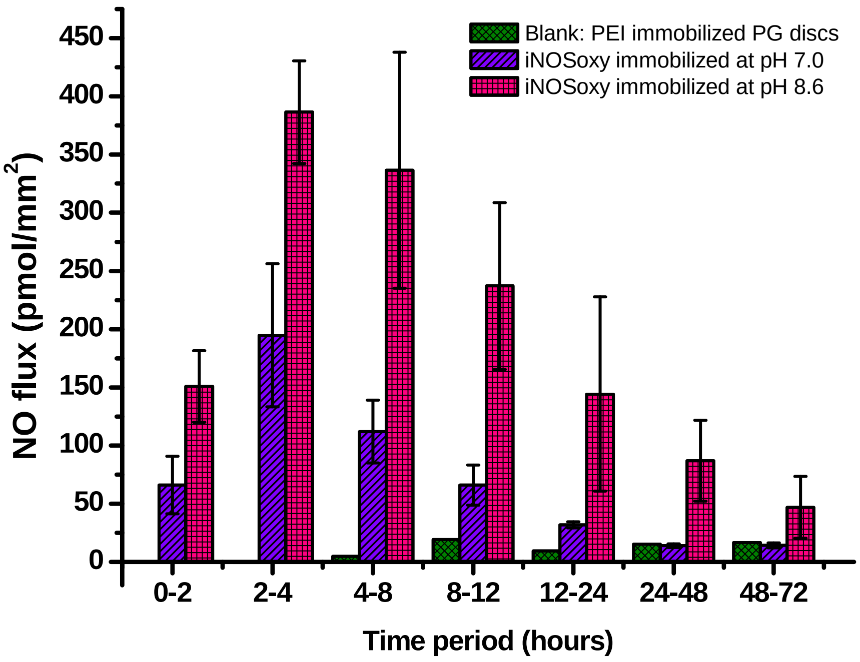

Figure 19: Average surface NO flux for each immobilization pH value; pH 7.0 & pH 8.6; Standard deviation shown where N=3 for each immobilization pH.

1.4 Conclusion

This chapter describes an improvement in the LbL method for the fabrication of thin films containing NOS enzymes for potential enzyme-based NI-release coatings. NOS enzymes can potentially be used in antithrombogenic coatings on blood-contacting medical implants. We have used pH to modulate the iNOSoxy loading on PEI layers. We report an increase of activity of the thin films formed at pH 8.6 compared to thin films built at pH 7.0 based on NO flux values. The activity of a LbL immobilized enzyme monolayer adsorbed at pH 8.6 is comparable to reported activity resulting from alternating (3)NOS-(3)PEI multilayer thin film, that was immobilized at pH 7.4.

The specific focus of this work has been to explore the use of pH of the immobilizing solution used to adsorb NOS enzyme layer to optimize enzyme loading on PEI. Electrochemical analysis of iNOSoxy films showed a high density of enzyme in films prepared at pH 8.6 compared to pH 7.0. This is consistent with our AFM imaging analyses, which show higher cluster density of features adsorbed at pH 8.6. The immobilization pH therefore controls the iNOSoxy loading on PEI thin films and hence the higher NO flux observed for films prepared at pH 8.6.

1.5 Reference

1. Taggart, D.P., *Stents or surgery in coronary artery disease in 2013.* Annals of Cardiothoracic Surgery, 2013. **2**(4): p. 431-434.

2. Serruys, P.W., M.C. Morice, A.P. Kappetein, A. Colombo, D.R. Holmes, M.J. Mack, E. Stahle, T.E. Feldman, M. van den Brand, E.J. Bass, N. Van Dyck, K. Leadley, K.D. Dawkins, and F.W. Mohr, *Percutaneous coronary intervention versus coronary-artery bypass grafting for severe coronary artery disease.* N Engl J Med, 2009. **360**(10): p. 961-72.

3. Moss, A.J., Hamburger, S., Moore, R.M., Jeng, L.L., Howie, L.J., *Use of selected medical device implants in the United States, 1988.* Advance data from vital and health statistics, Feb 26, 1991. **191**: p. 1-24.

4. Baim, D.S., Carrozza Jr, J.P., *Stent thrombosis; closing in on the best preventive treatment.* Circulation, 1997. **95**(5): p. 1098-1100.

5. Rasche, H., *Haemostasis and thrombosis: an overview.* European Heart Journal Supplements, 2001. **3**(Q): p. Q3-Q7.

6. Iakovou, I., *Thrombosis after stent implantation: How much of a problem is there?* Future Cardiology, 2008. **4**(3): p. 261-267.

7. Matsumoto, M., T. Ban, and Y. Okamoto, *Behavior of platelets and leukocytes on the luminal surface of small caliber polyurethane grafts.* J Cardiovasc Surg (Torino), 1989. **30**(4): p. 609-13.

8. van Kampen, C.L. and D.F. Gibbons, *Effect of implant surface chemistry upon arterial thrombosis.* J Biomed Mater Res, 1979. **13**(4): p. 517-41.

9. Sarkar, S., K.M. Sales, G. Hamilton, and A.M. Seifalian, *Addressing thrombogenicity in vascular graft construction.* J Biomed Mater Res B Appl Biomater, 2007. **82**(1): p. 100-8.

10. Frost, M., Meyerhoff, M.E., *Sensors: Tackling biocompatibility.* Analytical Chemistry, 2006. **78**(1): p. 7370-7377.

11. Alkhamis, T.M., Beissinger, R.L., Chediak, J.R., *Artificial surface effect on red blood cells and platelets in laminar shear flow.* Blood, 1990. **75**(7): p. 1568-1575.

12. Furie, B. and B.C. Furie, *Thrombus formation in vivo.* J Clin Invest, 2005. **115**(12): p. 3355-62.

13. Urban, P., A. Abizaid, A. Banning, A.L. Bartorelli, A.C. Baux, V. Dzavik, S. Ellis, R. Gao, D. Holmes, M.H. Jeong, V. Legrand, F.J. Neumann, M. Nyakern, C. Spaulding, and S. Worthley, *Stent thrombosis and bleeding complications after implantation of sirolimus-eluting coronary stents in an unselected worldwide population: a report from the e-SELECT (Multi-Center Post-Market Surveillance) registry.* J Am Coll Cardiol, 2011. **57**(13): p. 1445-54.

14. Hanna, N.N., M.A. Gaglia, Jr., R. Torguson, I. Ben-Dor, M.A. Gonzalez, S.D. Collins, A.I. Syed, G. Maluenda, K. Kaneshige, Z. Xue, L.F. Satler, K.M. Kent, W.O. Suddath, A.D. Pichard, and R. Waksman, *Three-year outcomes following sirolimus- versus paclitaxel-eluting stent implantation in an unselected population*

with coronary artery disease (from the REWARDS Registry). Am J Cardiol, 2010. **106**(4): p. 504-10.

15. Di Lorenzo, E., R. Sauro, A. Varricchio, G. Carbone, G. Cortese, M. Capasso, T. Lanzillo, F. Manganelli, C. Mariello, F. Siano, M.R. Pagliuca, G. Stanco, G. Rosato, and G. De Luca, *Long-Term outcome of drug-eluting stents compared with bare metal stents in ST-segment elevation myocardial infarction: results of the paclitaxel- or sirolimus-eluting stent versus bare metal stent in Primary Angioplasty (PASEO) Randomized Trial.* Circulation, 2009. **120**(11): p. 964-72.

16. Jacobs, H., D. Grainger, T. Okano, and S.W. Kim, *Surface modification for improved blood compatibility.* Artif Organs, 1988. **12**(6): p. 506-7.

17. Walford, G., Locallzo, J., *Nitric oxide in vascular biology.* Journal of Thrombosis and Haemostasis, 2003. **1**(10): p. 2112-2118.

18. Ignarro, L.J., *Biological actions and properties of endothelium-derived nitric oxide formed and released from artery and vein.* Circulation Research, 1989. **65**(1): p. 1-21.

19. Jourd'heuil, D., Hallen, K., Feelisch, M., Grisham, M.B., *Dynamic state of S-nitrosothiols in human plasma and whole blood.* Free Radical Biology & Medicine, 2000. **28**(3): p. 409-417.

20. Zhang, H., Annich, G.M., Miskulin, J., Stankiewicz, K., Osterholzer, K., Merz, S.I., Bartlett, R.H., Meyerhoff, M.E., *Nitric oxide releasing fumed silica particles: Synthesis, characterization, and biomedical application.* Journal of the American Chemical Society, 2003. **125**(17): p. 5015-5024.

21. Titheradge, M.A., *Nitric oxide protocols*. Methods in molecular biology. 1998, Totowa, N.J.: Humana Press. xi, 324 p.

22. Stuehr, D.J., N.S. Kwon, C.F. Nathan, O.W. Griffith, P.L. Feldman, and J. Wiseman, *N omega-hydroxy-L-arginine is an intermediate in the biosynthesis of nitric oxide from L-arginine.* J Biol Chem, 1991. **266**(10): p. 6259-63.

23. Kwon, N.S., C.F. Nathan, C. Gilker, O.W. Griffith, D.E. Matthews, and D.J. Stuehr, *L-citrulline production from L-arginine by macrophage nitric oxide synthase. The ureido oxygen derives from dioxygen.* J Biol Chem, 1990. **265**(23): p. 13442-5.

24. Mayer, B., M. John, B. Heinzel, E.R. Werner, H. Wachter, G. Schultz, and E. Bohme, *Brain nitric oxide synthase is a biopterin- and flavin-containing multi-functional oxido-reductase.* FEBS Lett, 1991. **288**(1-2): p. 187-91.

25. Klatt, P., K. Schmidt, G. Uray, and B. Mayer, *Multiple catalytic functions of brain nitric oxide synthase. Biochemical characterization, cofactor-requirement, and the role of N omega-hydroxy-L-arginine as an intermediate.* J Biol Chem, 1993. **268**(20): p. 14781-7.

26. Bredt, D.S., P.M. Hwang, C.E. Glatt, C. Lowenstein, R.R. Reed, and S.H. Snyder, *Cloned and expressed nitric oxide synthase structurally resembles cytochrome P-450 reductase.* Nature, 1991. **351**(6329): p. 714-8.

27. Cho, H.J., Q.W. Xie, J. Calaycay, R.A. Mumford, K.M. Swiderek, T.D. Lee, and C. Nathan, *Calmodulin is a subunit of nitric oxide synthase from macrophages.* J Exp Med, 1992. **176**(2): p. 599-604.

28. Trepakova, E.S., R.A. Cohen, and V.M. Bolotina, *Nitric oxide inhibits capacitative cation influx in human platelets by promoting sarcoplasmic/endoplasmic reticulum Ca2+-ATPase-dependent refilling of Ca2+ stores.* Circ Res, 1999. **84**(2): p. 201-9.

29. Kroll, M.H. and A.I. Schafer, *Biochemical mechanisms of platelet activation.* Blood, 1989. **74**(4): p. 1181-95.

30. Moro, M.A., R.J. Russel, S. Cellek, I. Lizasoain, Y. Su, V.M. Darley-Usmar, M.W. Radomski, and S. Moncada, *cGMP mediates the vascular and platelet actions of nitric oxide: confirmation using an inhibitor of the soluble guanylyl cyclase.* Proc Natl Acad Sci U S A, 1996. **93**(4): p. 1480-5.

31. Rao, G.H., S. Krishnamurthi, L. Raij, and J.G. White, *Influence of nitric oxide on agonist-mediated calcium mobilization in platelets.* Biochem Med Metab Biol, 1990. **43**(3): p. 271-5.

32. Pigazzi, A., S. Heydrick, F. Folli, S. Benoit, A. Michelson, and J. Loscalzo, *Nitric oxide inhibits thrombin receptor-activating peptide-induced phosphoinositide 3-kinase activity in human platelets.* J Biol Chem, 1999. **274**(20): p. 14368-75.

33. Zhang, J., J. Zhang, S.J. Shattil, M.C. Cunningham, and S.E. Rittenhouse, *Phosphoinositide 3-kinase gamma and p85/phosphoinositide 3-kinase in platelets. Relative activation by thrombin receptor or beta-phorbol myristate acetate and roles in promoting the ligand-binding function of alphaIIbbeta3 integrin.* J Biol Chem, 1996. **271**(11): p. 6265-72.

34. Michelson, A.D., S.E. Benoit, M.I. Furman, W.L. Breckwoldt, M.J. Rohrer, M.R. Barnard, and J. Loscalzo, *Effects of nitric oxide/EDRF on platelet surface glycoproteins.* Am J Physiol, 1996. **270**(5 Pt 2): p. H1640-8.

35. Geiger, J., C. Nolte, and U. Walter, *Regulation of calcium mobilization and entry in human platelets by endothelium-derived factors.* Am J Physiol, 1994. **267**(1 Pt 1): p. C236-44.

36. Fischer, T.H. and G.C. White, 2nd, *Partial purification and characterization of thrombolamban, a 22,000 dalton cAMP-dependent protein kinase substrate in platelets.* Biochem Biophys Res Commun, 1987. **149**(2): p. 700-6.

37. Murohara, T., S.J. Parkinson, S.A. Waldman, and A.M. Lefer, *Inhibition of nitric oxide biosynthesis promotes P-selectin expression in platelets. Role of protein kinase C.* Arterioscler Thromb Vasc Biol, 1995. **15**(11): p. 2068-75.

38. Bayachou, M., Abou-Diwan, C. , *US Patent # 2009/073643.* 2009.

39. Freedman, J.E., Localzo, J., Barnard, M.R., Alpert, C., Keany, J.F., Michelson, A.D., *Nitric oxide released from activated platelets inhibits platelet recruitment.* Journal of Clinical Investigation, 1997. **100**(2): p. 350-356.

40. Smith, A.W., *Biofilms and antibiotic therapy: Is there a role for combating bacterial resistance by the use of novel drug delivery systems?* Advanced Drug Delivery Reviews, 2005. **57**(10).

41. Kenawy, E., G.L. Bowlin, K. Mansfield, J. Layman, D.G. Simpson, E.H. Sanders, and G.E. Wnek, *Release of tetracycline hydrochloride from electrospun*

poly(ethylene-co-vinylacetate), poly(lactic acid), and a blend. Journal of Controlled Release, 2002. **81**(1–2): p. 57-64.

42. Telemeco, T.A., C. Ayres, G.L. Bowlin, G.E. Wnek, E.D. Boland, N. Cohen, C.M. Baumgarten, J. Mathews, and D.G. Simpson, *Regulation of cellular infiltration into tissue engineering scaffolds composed of submicron diameter fibrils produced by electrospinning.* Acta Biomater, 2005. **1**(4): p. 377-85.

43. Sun, T., S. Mai, D. Norton, J.W. Haycock, A.J. Ryan, and S. MacNeil, *Self-organization of skin cells in three-dimensional electrospun polystyrene scaffolds.* Tissue Eng, 2005. **11**(7-8): p. 1023-33.

44. Lyu, S., C. Huang, H. Yang, and X. Zhang, *Electrospun fibers as a scaffolding platform for bone tissue repair.* J Orthop Res, 2013. **31**(9): p. 1382-9.

45. Wang, H.S., G.D. Fu, and X.S. Li, *Functional polymeric nanofibers from electrospinning.* Recent Pat Nanotechnol, 2009. **3**(1): p. 21-31.

46. Wang, X., B. Ding, and B. Li, *Biomimetic electrospun nanofibrous structures for tissue engineering.* Materials Today, 2013. **16**(6): p. 229-241.

47. Palmer, R.M.J., D.S. Ashton, and S. Moncada, *Vascular endothelial-cells synthesize nitric-oxide from L-arginine.* Nature, 1988. **333**(6174): p. 664-666.

48. Hakim, T.S., K. Sugimori, E.M. Camporesi, and G. Anderson, *Half-life of nitric oxide in aqueous solutions with and without haemoglobin.* Physiol Meas, 1996. **17**(4): p. 267-77.

49. Gladwin, M.T., J.H. Crawford, and R.P. Patel, *The biochemistry of nitric oxide, nitrite, and hemoglobin: role in blood flow regulation.* Free Radic Biol Med, 2004. **36**(6): p. 707-17.

50. Yan, Z.-Q., Yokoda, T., Zhang, W., Hansson, G.K., *Expression of inducible nitric oxide synthase inhibits platelet adhesion and restores blood flow in injured artery.* Circulation Research, 1996. **79**(1): p. 38-44.

51. Vaughn, M.W., Kuo, L., Lioa, J.C., *Estimation of nitric oxide production and reaction rates in tissue by use of a mathematical model.* American Journal of Physiology; Heart and Circular Physiology, 1998. **274**(6-2): p. H2163-2176.

52. Bjellqvist, B., Hughes, G.J., Pasquali, Ch., Paquet, N., Ravier, F., Sanchez, J.-Ch., Frutiger, S., Hochstrasser, D.F., *The focusing positions of polypeptides in immobilized pH gradients can be predicted from their amino acid sequences.* Electrophoresis, 1993. **14**(10): p. 1023-1031.

53. Bjellqvist, B., Basse, B., Olsen, E. and Celis, J.E., *Reference points for comparisons of two-dimensional maps of proteins from different human cell types defined in a pH scale where isoelectric points correlate with polypeptide compositions.* Electrophoresis, 1994. **15**(3-4): p. 529-539.

54. Gasteiger E., H.C., Gattiker A., Duvaud S., Wilkins M.R., Appel R.D., Bairoch A., *Protein Identification and Analysis Tools on the ExPASy Server*, ed. J.M. Walker. The Proteomics Protocols Handbook, Humana Press (2005).

55. Belegrinou, S., Mannelli, I., Lisboa, P., Bretagnol, F., Valsesia, A., Ceccone, G., Colpo, P., Rauscher, H., Rossi, F., *pH-dependant immobilization of proteins on*

surfaces functionalized by plasma-enhanced chemical vapor deposition of poly(acrylic acid)- and poly(ethylene oxide)-like films Langmuir, 2008. **24**(14): p. 7251-7261.

56. Stuehr, D.J., *Purification and properties of nitric oxide synthase.* Methods in Enzymology, 1996. **268**: p. 324-333.

57. Tiso, M., Strub, A., Hesslinger, C., Kenney, C.T., Boer, R., Stuehr, D.J., *BYK191023 (2-[2-(4-Methoxy-pyridin-2-yl)-ethyl]-3H-imidazo[4,5-b]pyridine) is an NADPH- and time-dependant irreversible inhibitor of inducible nitric oxide synthase.* Molecular Pharmacology, 2008. **73**(4): p. 1244-1253.

58. Wang, Z., Wei, C., Stuehr, D.J., *A Conserved Tryptophan 457 Modulates the Kinetics and Extent of N-Hydroxy-l-Arginine Oxidation by Inducible Nitric-oxide Synthase.* The Journal of Biological Chemistry, 2002. **277**(15): p. 12830-12837.

59. Rusling, J.F., Nassar, A.F., *Enhanced electron transfer for myoglobin in surfactant films on electrodes.* Journal of the American Chemical Society, 1996. **115**(25): p. 11891-11897.

60. Waitumbi, J. and A. Warburg, *Phlebotomus papatasi saliva inhibits protein phosphatase activity and nitric oxide production by murine macrophages.* Infect Immun, 1998. **66**(4): p. 1534-7.

61. Immoos, C.E., Chou, J., Bayachou, M., Blair, E., Greaves, J., Farmer, P.J., *Electrocatalytic reductions of nitrite, nitric oxide, and nitrous oxide by thermophilic cytochrome P450 CYP119 in film-modified electrodes and an*

analytical comparison of its catalytic activities with myoglobin. Journal of the American Chemical Society, 2004. **126**(15): p. 4934-4942.

62. Agarwal, P.K., Geist, A., Gorin, A., *Protein dynamics and enzymatic catalysis: investigating the peptidyl-prolyl cis-trans isomerization activity of cyclophilin A.* Biochemistry, 2004. **43**(33): p. 10605-10618.

63. Agarwal, P.K., Billeter, S.R., Rajagopalan, P.T,, Benkovic, S.J., Hammes-Schiffer, S., *Network of coupled promoting motions in enzyme catalysis.* Proc. Natl. Acad. Sci., 2002. **99**(5): p. 2794-2799.

64. Yang, L.W., Bahar, I., *Coupling between catalytic site and collective dynamics: A requirement for mechanochemical activity of enzymes.* Structure, 2005. **13**(6): p. 893-904.

65. Tousignant, A., Pelletier, J.N. , *Protein motions promote catalysis.* Chemistry & Biology, 2004. **11**(8): p. 1037-1042.

66. Doshi, U., McGowan, L.C., Ladani, S.F., Hamelberg, D., *Resolving the complex role of enzyme conformational dynamics in catalytic function.* Proceedings of the National Academy of Sciences, 2012. **109**(15): p. 5699-5704.

67. Weikl, T.R., Hammateenejad, B., *How conformational changes can affect catalysis, inhibition and drug resistance of enzymes with induced-fit binding mechanism such as the HIV-1 protease* Biochimica et Biophysica Acta, 2013. **1834**(5): p. 867-873.

68. Ishikita, H., Eger, B.T., Okamoto, K., Nishino, T., Pai, E.F., *Protein conformational gating of enzymatic activity in Xanthine Oxidoreductase.* Journal of the American Chemical Society, 2012. **134**(2): p. 999-1009.

69. Gao, J., *Catalysis by enzyme conformational change as illustrated by orotidine 5'-monophosphate decarboxylase.* Current Opinion in Structural Biology, 2003. **13**: p. 184-192.

70. Vendruscolo, M., *Enzymatic activity in disordered state of proteins.* Current Opinion in Chemical Biology, 2010. **14**: p. 671-675.

71. Korkmaz-Ozkan, F., Koster, S., Kuhlbrandt, W., Mantele, W., Yildiz, O., *Correlation between the OmpG secondary structure and its pH-dependant alterations monitored by FTIR.* Journal of Molecular Biology, 2010. **401**(1): p. 56-67.

72. Shang, L., Wang, Y., Jiang, J., Dong, S., *pH-Dependant protein conformational changes in Albumin: Gold nanoparticle bioconjugates: A spectroscopic study.* Langmuir, 2007. **23**(5): p. 2714-2721.

73. Baron, M.H., Revault, M., Servagent-Noinville, S., Abadie, J., Quiquampoix, H., *Chymotrypsin adsorption on Montmorillonite: Enzymatic activity and kinetic FTIR structural analysis.* Journal of Colloid and Interface Science, 1999. **214**(2): p. 319-332.

74. Venyaminov, S. and N.N. Kalnin, *Quantitative IR spectrophotometry of peptide compounds in water (H2O) solutions. I. Spectral parameters of amino acid residue absorption bands.* Biopolymers, 1990. **30**(13-14): p. 1243-57.

75. Krimm, S. and J. Bandekar, *Vibrational spectroscopy and conformation of peptides, polypeptides, and proteins.* Adv Protein Chem, 1986. **38**: p. 181-364.

76. Dockal, M., Carter, D.C., Ruker, F., *Conformational transitions of the three recombinant domains of human serum albumin depending on pH.* Journal of Biological Chemistry, 2000. **275**: p. 3042-3050.

77. El Kadi, N., Taulier, N., Le Heurou, J.Y., Gindre, M., Urbach, W., Nwigwe, I., Kahn, P.C., Waks, M., *Unfolding and refolding of bovine serum albumin at acid pH: Ultrasound and structural studies.* Biophysical Journal, 2006. **91**: p. 3397-3404.

78. Shao, Q., We, P., Gu, P., Xu, X., Zhang, H., Cai, C., *Electrochemical and spectroscopic studies on the conformational structure of hemoglobin assembled on gold nanoparticles.* The Journal of Physical Chemistry, 2011. **115**: p. 8627-8637.

79. Di Russo, N.V., Estrin, D.A., Marti, M.A., Roitberg, A.E., *pH-Dependent conformational changes in croteins and their effect on experimental pK*$_a$*s: The case of Nitrophorin 4.* PLoS Computational Biology, 2012. **8**(11): p. 1-9.

80. Martinez-Cruz, L.A., Encinar, J. A., Kortazar, D., Prieto, J., Gomez, J., Fernandez-Millan, P., Lucas, M., Arribas, E.A., Fernandez, J.A., Martinez-Chantar, M.L., Mato, J.M., Neira, J.L., *The CBS domain protein MJ0729 of Methanocaldococcus jannaschii is a thermostable protein with pH-dependant self-oligomerization.* Biochemistry, 2009. **48**(12): p. 2760-2776.

81. Stevens, M.M., Allen, S., Sakata, J.K., Davies, M.C., Roberts, C.J., Tendler, S.J.B., Tirrel, D.A., Williams, P.M. , *pH-dependant behavior of surface-immobilized artificial Leucine Zipper Proteins.* Langmuir, 2004. **20**(18): p. 7747-7752.

82. Dirix, C., Duvetter, T., Loey, A.V., Hendrickx, M., Heremans, K., *The in situ observation of the temperature and pressure stability of recombinant Aspergillus aculeatus pectin methylesterase with Fourier transform IR spectroscopy reveals an unusual pressure stability of β-helices.* Biochemical Journal, 2005. **392**(Pt 3): p. 565-571.

83. Lefevre-Groboillot, D., J.L. Boucher, D. Mansuy, and D.J. Stuehr, *Reactivity of the heme-dioxygen complex of the inducible nitric oxide synthase in the presence of alternative substrates.* Febs j, 2006. **273**(1): p. 180-91.

84. Pufahl, R.A., J.S. Wishnok, and M.A. Marletta, *Hydrogen Peroxide-Supported Oxidation of NG-Hydroxy-L-Arginine by Nitric Oxide Synthase.* Biochemistry, 1995. **34**(6): p. 1930-1941.

85. Jun, H.-W., TaiteL.J., West, J.L., *Nitric oxide-producing polyurethanes.* Biomacromolecules, 2005. **6**(2): p. 838-844.

86. Matl, F.D., A. Obermeier, S. Repmann, W. Friess, A. Stemberger, and K.D. Kuehn, *New anti-infective coatings of medical implants.* Antimicrob Agents Chemother, 2008. **52**(6): p. 1957-63.

87. Miller, P.E., Carlton, D., Deierhoi, M.H., Redden, D.T., Allon, M. , *Natural history of arteriovenous grafts in hemodialysis patients.* American Journal of Kidney Diseases, 2000. **36**(1): p. 68-74.

CHAPTER II: LbL THIN FILMS OF INDUCIBLE NITRIC OXIDE SYNTHASE OXYGENASE (iNOSoxy) AND BRANCHED POLYETHYLENIMINE (PEI)

2.1 Introduction

In this chapter we report enzyme-derived NO flux values from iNOSoxy monolayer immobilized on PEI matrix that has a branched polymeric structure as opposed to linear PEI. Charge-based electrostatic adsorption of macromolecules onto nanostructured thin-films comprising of different matrices and their bioactivity have been reported [1-4].

The effective NO flux resulting from active component in the film considered - iNOSoxy - is proportional to the number of active enzyme units at the surface. In the work described in this chapter, we explored the role of the polymeric structure of the underlying PEI matrix (linear vs. branched) on iNOSoxy enzyme loading, using the LbL process.

2.1.1 Charge density of matrix polymer and its significance

The isoelectric point of mouse iNOS is 7.76 while for iNOSoxy domain used in this work, it is 6.11 [3-5]. Therefore, iNOSoxy protein carries an overall positive charge in solutions maintained below pH 6.11. In contrast, at pH values higher than 6.11 in solution, the iNOSoxy domain has an overall negative charge. In the previous chapter, we have shown how the increased charge density of protein in solution drives more adsorption. In this chapter we used a pH of 8.6 for immobilization, based on our results described in chapter 1 that indicated higher enzyme loading onto iNOSoxy/PEI thin films at pH 8.6 compared to pH 7.0. In the current work we explored a different approach to achieve higher immobilization and activity. Linear and branched versions of same polymer matrix are known to carry different charge densities in solution [6, 7]. In a linear segment of PEI, every third atom is a secondary amino nitrogen that is protonable. This makes linear PEI chains excellent proton exchangers [8]. Therefore, the presence of protonated secondary amine groups in the linear PEI side-chains of branched PEI gives branched PEI a higher overall charge density, similar to reported charge density enhancement in other branched matrices [9]. We take advantage of this phenomenon, and use both linear and branched PEI as the matrices to compare and contrast immobilized iNOSoxy monolayers under both conditions. Polymer charge density and its significance in the formation of multilayered assemblies [10], co-deposition methods [11] and its ultimate effect on the adsorption of polyelectrolytes [12] have been reported. In our case, charge density of underlying matrix polymer layer is expected to dictate the level of iNOSoxy loading, and the strength of the electrostatic attraction. The characterization methods investigate the loading and activity of iNOSoxy in the linear and branched matrices.

2.2 Experimental

2.2.1 Expression and purification of iNOSoxy through recombinant plasmid DNA

Mouse iNOS oxygenase (iNOSoxy) domain template transgene in pCWori vector plasmid transformed into BL21(DE3) ampicillin-resistant *E. coli.* strain has been used for the protein expression (received from the Dennis Stuehr Laboratory at the Lerner Research Institute, Cleveland Clinic, Cleveland, OH, USA). From the glycerol stocks stored at -80°C, we initiated growth of the host and induced synthesis of the enzyme protein according to standard purification protocols [13] described in chapter 1. Cells were harvested by pelleting the growth media and lysing the microbial cells to release and then precipitate the protein. Finally we used affinity chromatography based on the His-tag sequence binding to a Nickel charged column to further purify the iNOSoxy protein [13, 14]. Dialysis was carried-out to further concentrate the aliquots obtained. Final concentration of protein in solution was determined for each batch before each characterization method, using the bathochromic shift of the Soret band for the p-450 type enzyme [15].

2.2.2 Atomic force microscopic (AFM) imaging of adsorbed thin layers

We used the Agilent Pico-SPM atomic force microscope, PicoView controller and Mac-mode module (Agilent Technologies Inc.). We used the multi-purpose macro scanner with a scan range of 90μm in the x-y dimension and 7μm in the z-dimension (Agilent Technologies Inc.). PointProbe® Plus AFM probes (NanoAndMore USA Inc., SC, USA) of 125 μm length, 30 μm width, 42 N/m spring constant, and 270 kHz resonant frequencies were used in Acoustic AC mode in the imaging. AFM imaging was done in the closed chamber at ambient conditions. We used general-purpose desiccant for dehumidifying the chamber. For immobilization of thin film components, we used grade ZYA highly ordered pyrolytic graphite (HOPG) (Structure Probe Inc., PA, USA). HOPG square sizes of 12 mm × 12 mm × 2 mm were used, mounted on the sample plate. Several graphite layers were stripped-off from the mounted HOPG surfaces before each scan. The bare HOPG surfaces were scanned at different scan speeds for scan sizes ranging from an initial wide-window size of 90 μm × 90 μm to focused scan sizes of 500 nm × 500 nm. Retrieved, aliquots of 100 μl of either linear or branched PEI (Polysciences Inc.) were added onto the surfaces. After an incubating for period of 5 minutes, the surfaces were washed thoroughly with DI water and were dried in a gentle nitrogen stream. Scan sizes ranging from 50 μm × 50 μm to 500 nm × 500 nm were obtained. Retrieved, aliquots of 50 μl of iNOSoxy adjusted to pH 8.6 were added onto each of the linear and branched PEI layers on HOPG. After an incubation time of 5-10 minutes, scans were performed for sizes 50 μm × 50 μm down to 500 nm × 500 nm.

2.2.3 Griess assay for the determination of activity of thin films of iNOSoxy

Using a hole-saw type drill bit, we made cylindrical PG discs from a high grade PG block. The discs were first polished following the same protocol described in chapter section 2.2.3. Using a Vernier caliper, the diameter of each disc was measured. Aliquots of 50 µl each of 1.5 mg/ml linear PEI solutions (Polysciences Inc.) were added onto three of the polished surfaces while aliquots of 50 µl each of 1.5 mg/ml branched PEI solutions (Polysciences Inc.) were added onto another three polished surfaces. After an incubation period of approximately 5 minutes, the surfaces were washed thoroughly using DI water. Then the surfaces were dried using a nitrogen stream.

Aliquots of 25 µl each of enzyme solution adjusted to pH 8.6 were added onto all six PEI immobilized disc surfaces. One disc having immobilized linear PEI without enzyme was used as the control. Modified surfaces were incubated for 15-20 minutes. Then, the surfaces were thoroughly washed using DI water before being dried in a gentle nitrogen stream. The seven discs were placed in the bottom of scintillation vials with the polished surfaces facing upwards. A cocktail volume of 5 ml reaction ingredients adjusted to 250 µM N-hydroxy-L-arginine (NHA), 10 µM tetrahydrobiopterin (H_4B), and 400 µM dithiothreitol (DTT) made in 100 mM phosphate buffer medium and adjusted to pH 7.4 was made for each vial. After adding the cocktail into the vials, the enzyme catalyzed reaction was triggered by adding hydrogen peroxide to a final concentration of 150mM. The vials were incubated at 37°C. Aliquots of 100 µl of reaction media were drawn from each vial at 2, 4, 8, 12, 24, 48 & 72 hour lapse times. These were combined with 100µl of each of Griess reagents R1 (sulfanilamide) and R2 (N-(1-naphthyl)ethylenediamaine)

(Cayman chemical company) in cuvettes. After a 10 minute reaction time for the assay, absorbance values were recorded against the blank at 540 nm (UV-Vis spectrophotometer; Model 8543, Agilent Technologies). Simultaneously, several standard calibration series were constructed.

2.2.4 Electrochemical investigation of heme-Fe^{3+} reduction and catalytic NO reduction by LbL immobilized PEI/iNOSoxy films on graphite electrodes

We used the redox active Fe^{3+}-heme of iNOSoxy to closely monitor the overall amount of iNOSoxy adsorbed in the two sets of films. Integration of the voltammetric current provides the faradaic charge passed, which can be converted to give the amount of iNOSoxy present in the film. The enzyme iNOSoxy, similar to other heme proteins and cytochrome P-450 enzymes, is able to catalyze the electrochemical reduction NO. We used this metalloprotein-dependent direct electron transfer of the enzyme as a handle to monitor its immobilization and activity in the thin layers.

An in-house purging system for making saturated NO in aqueous solution was used. Nitric oxide (Praxair) was purged through an alkaline pyrogallol solution (1:4 v/v 250 mg.ml^{-1} pyrogallol : 1 g.ml^{-1} KOH) for oxygen-scrubbing. The resulting oxygen free NO gas flow was purged through a saturated KOH solution for the removal of remaining gaseous oxides. The resultant purging was collected into 10 ml of DI water contained in a sealed scintillation vial. Concentration of saturated aqueous NO solution was confirmed using a Griess reagent system based calibration, before each experimental step for a separately purged, NO (NO_2^-) saturated solution.

Cylindrical pyrolytic graphite discs drilled-out from graphite blocs were connected to insulated copper wire, via a junction using conductive epoxy. Discs were then tightly fitted onto the end of glass tube using non-conductive epoxy resin. After letting the epoxy dry, the discs were first polished using a rotating polishing pad according to earlier protocols [16]. The discs were polished using 0.3 μm size Alumina. After washing, they were polished again using 0.05 μm size alumina. All discs were cleaned further by sonicating in a water bath for 30 seconds. Then the electrodes were blow-dried using a nitrogen stream. Aliquots of 5 μl each of 1.5 mg/ml linear and branched PEI solution (Polysciences Inc.) were added onto the polished surfaces of each of the discs. After incubating for 10 minutes, the electrodes were washed with DI water and dried in a nitrogen stream. On top of the electrodes immobilized with linear and branched PEI, aliquots of 5 μl of enzyme solution were added. We used five electrodes with relatively low capacitive currents for enzyme immobilization, and tested them with both linear PEI and branched PEI as matrices. Three electrodes coated with only linear PEI and not immobilized with enzyme were used as the control.

We used multi-necked electrochemical cells (Ace Glass) to set-up apparatus for enzyme immobilized PG electrode, Ag/AgCl reference electrode and platinum auxiliary electrode to make contact with 10.0 ml of the phosphate buffer solution used as the electrolytic medium. The buffer used, has been de-gased first for 30 minutes using a slow nitrogen purge to remove oxygen. A nitrogen blanket was maintained throughout all stages of the experiment. First, we observed the current as a response to a linear sweep of potential in the absence of NO substrate for all the electrodes. Proceeding onto cyclic voltammetry, we did several blank cyclic voltammetric scans to confirm the absence of peak reducing currents for the reduction of NO_2^- in solution. Introducing the substrate, aliquots of 2.0 mM NO were injected to the buffer solution using a Hamilton syringe, increasing the NO concentration in buffer by approximately 20 μM increments. Immediately after each injection, the solution was swiftly stirred by the magnetic stirrer before a scan was done.

2.3 Results and discussion

2.3.1 AFM imaging of modified surfaces

Figure 20(a) shows topology of the bare HOPG surface while Figure 20(b) shows the PEI immobilized HOPG surface. The topological image of PEI-modified HOPG shows aggregate polymeric features. In Figure 21, we show the topological images of iNOSoxy on PEI. Figure 21(a) for iNOSoxy immobilized on linear PEI shows sparsely distributed, small clusters of features after incubation in iNOSoxy solution. Figure 21(b), on the other hand, shows larger clusters of protein aggregates.

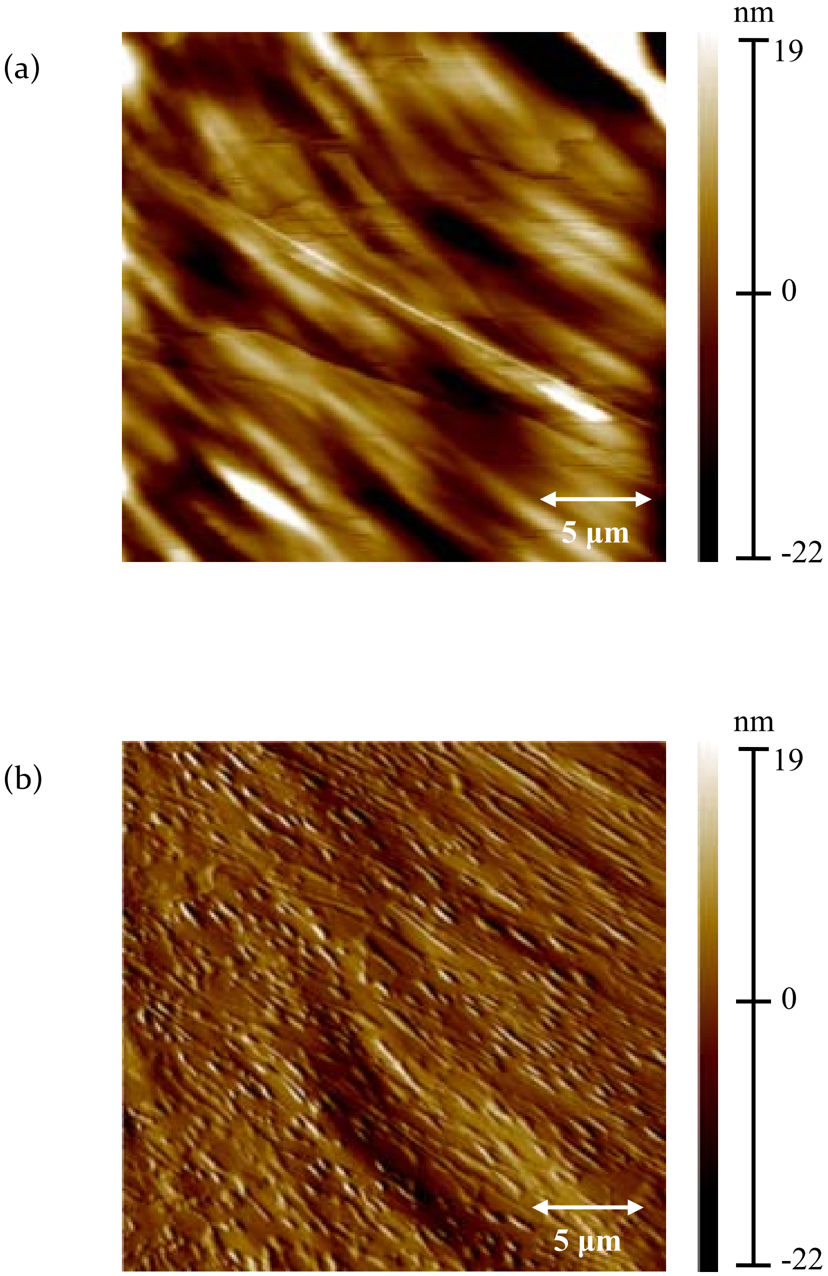

Figure 20: AFM images on the topology of the bare and PEI matrix adsorbed surfaces; a) Bare HOPG (scan size 25 µm × 25 µm), b) PEI immobilized on HOPG for 5min (Scan size: 25 µm × 25 µm).

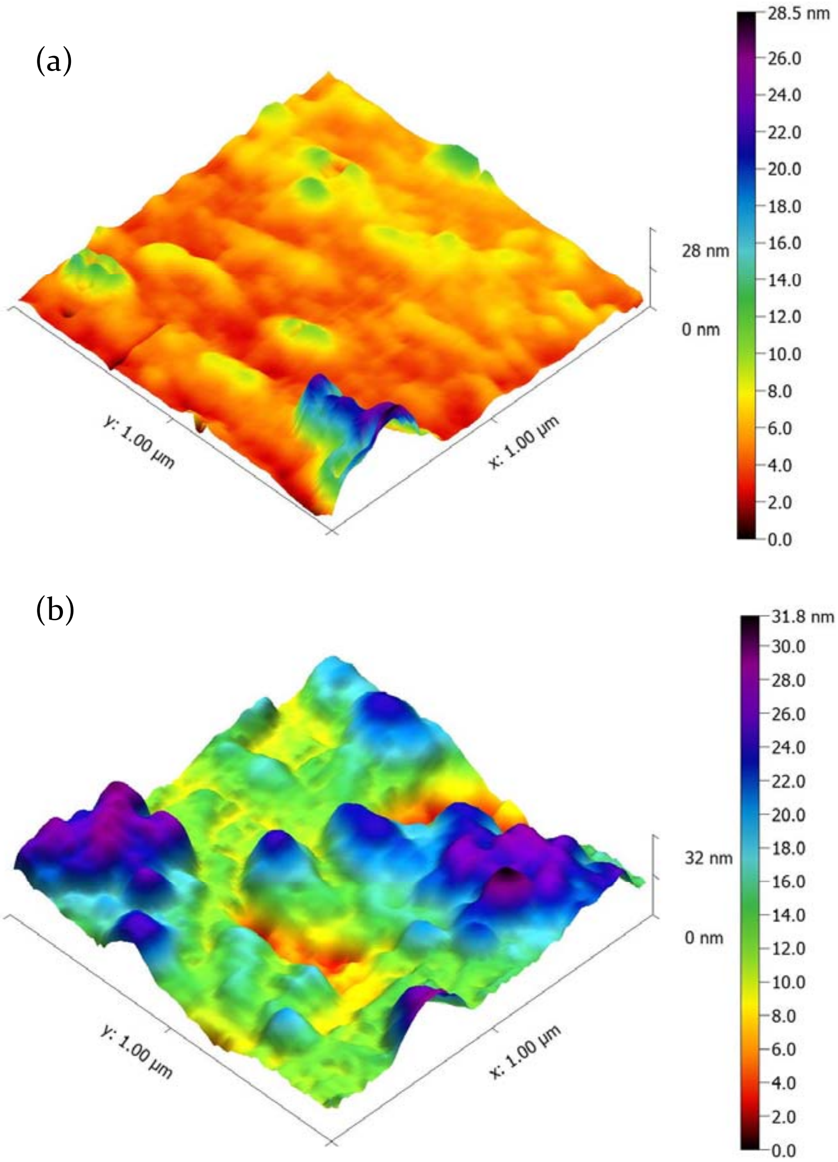

Figure 21: AFM images on the topology of the outermost layer in iNOSoxy immobilization on PEI; a) Outermost NOS layer immobilized at pH 8.6 on linear PEI matrix (Scan size: 1 µm × 1 µm) & b) Outermost NOS layer immobilized at pH 8.6 on branched PEI matrix (Scan size: 1 µm × 1 µm).

The analysis of clusters using Scanning Probe Image Processor (SPIP) is shown in Figure 22. Overall, for the range of feature diameters 20-100nm, iNOSoxy immobilized on linear PEI shows higher abundance of features than iNOSoxy immobilized on branched PEI. There is no significant difference in clusters in the diameter range from 100-120nm for linear and branched PEI based films. However, branched PEI based iNOSoxy layers show the presence of relatively larger clusters, from 140-280nm in diameter of features not seen on linear PEI. Overall, branched PEI loads more iNOSoxy units and exhibits a higher degree of roughness of iNOSoxy on surface compared to linear PEI.

The positive charge density of matrix layer increases for PEI due to its branching. This is expected to drive higher level of iNOSoxy adsorption and potentially higher roughness on surface compared to linear PEI.

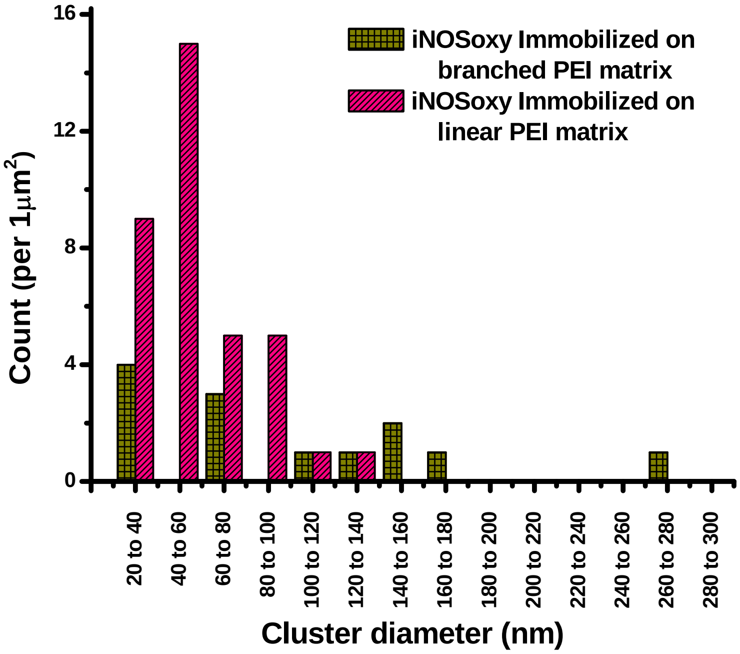

Figure 22: Histographic comparison of cluster diameters for Figure 21 a) & 21 b) showing number of features in each diameter range.

2.3.2 Activity of thin films of enzyme

Graphs on cumulative NO concentration in reaction cocktail, assayed by Griess reagent system [17] is shown in Figure 23. The cumulative NO release follows a general pattern of an initial burst to a plateau through the 72-hour measurement window, which is a typical two-phase release model [18, 19]. However, the average cumulative concentration at each sample interval resulting from iNOSoxy layer immobilized on branched PEI matrix is higher than the average cumulative concentration resulting from iNOSoxy layer immobilized on linear PEI matrix. At 72 hours, iNOSoxy layer immobilized on branched PEI matrix resulted in an average NO concentration of 16 μM in solution, whereas iNOSoxy layer immobilized on linear PEI matrix resulted in an average NO concentration close to 12 μM.

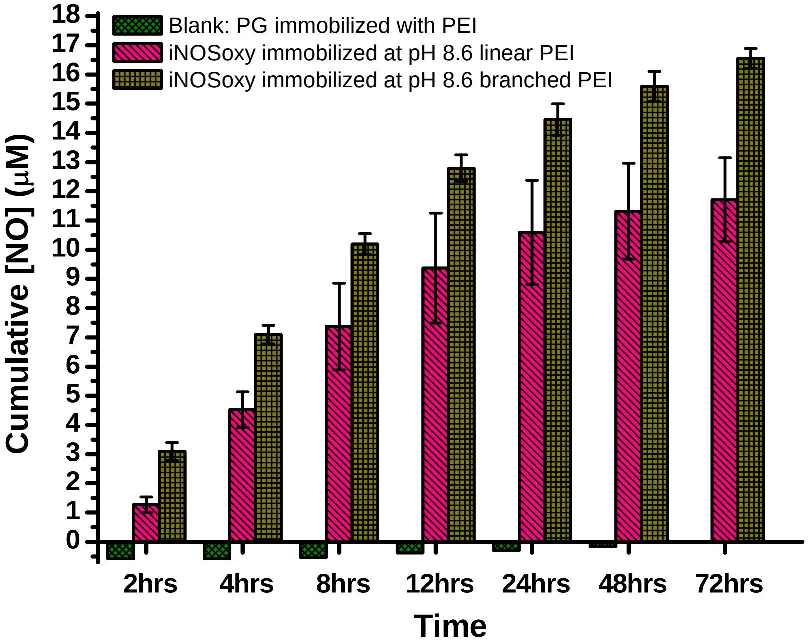

Figure 23: Average cumulative NO concentration generated from iNOSoxy/PEI films using branched PEI and linear PEI. Error bars represent standard deviations for 5 trials.

As shown previously (chapter 1), the average flux per unit surface area for all the immobilized surfaces shows an initial burst of NO through the first 12 hours as shown in Figure 24. This initial burst is followed by a decline and then a steady state of NO release up to the end of our observation window of 72 hours [20]. The average flux peaks at 2-4 hours from the start of the reaction, i.e. the incubation of thin layers. For the 2-4 hour time window, the average peak NO flux values range from nearly 479 pmol.mm^{-2} for discs having iNOSoxy immobilized on branched PEI matrix to about 386 pmol.mm^{-2} for discs having iNOSoxy immobilized on linear PEI matrix. For the two hour window considered, this translates to nearly 400 $\text{pmol.cm}^{-2}.\text{min}^{-1}$ for discs immobilized with thin films of iNOSoxy on branched PEI and to nearly 322 $\text{pmol.cm}^{-2}.\text{min}^{-1}$ for discs immobilized with thin films of iNOSoxy on linear PEI. Furthermore, average NO flux by iNOSoxy immobilized on linear PEI matrix diminishes faster, while NO flux resulting iNOSoxy immobilized on branched PEI matrix remains higher. Branched PEI based iNOSoxy monolayers equal the reported NO flux of stimulated human endothelial cells of 400 $\text{pmol.cm}^{-2}.\text{min}^{-1}$ [21].

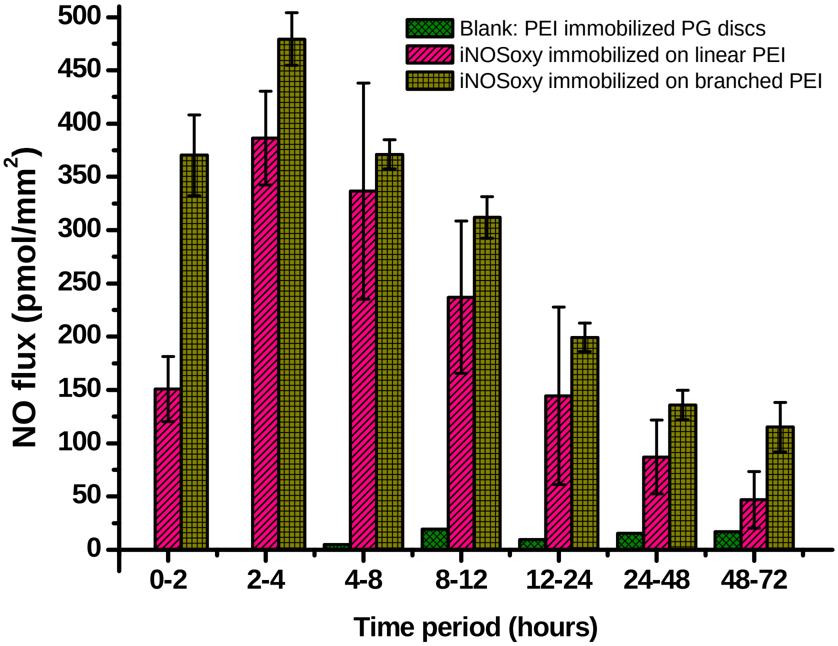

Figure 24: Average surface flux of NO from iNOSoxy/PEI films immobilized on branched PEI and linear PEI. Error bars represent standard deviations for 5 trials.

2.3.3 Electrochemistry and Michaelis-Menten kinetics

2.3.3.1 Electrocatalytic reduction of NO mediated by iNOSoxy in films

Electrochemical analyses of iNOSoxy immobilized electrodes have been used to provide both the amount of enzyme units on surface and their catalytic turnover rates. First, in the absence of NO – the reducible substrate – we used the redox active Fe^{3+}-heme of iNOSoxy to quantify the iNOSoxy adsorption in the two sets of films; one on linear PEI matrix and the other on branched PEI matrix. Integration of the voltammetric current provides the faradaic charge passed through the redox active iNOSoxy in each film, which is an indication of the amount of iNOSoxy present. Like chapter 1, we also used iNOSoxy-mediated NO catalytic reduction to compare and contrast the amount and catalytic integrity of adsorbed iNOSoxy units.

Figure 25 shows a typical cyclic voltammogram for a heme containing film for the specific window. Shown here are the Fe^{3+}/Fe^{2+} and Fe^{2+}/Fe^{+} redox couples, of iNOSoxy in this experiment.

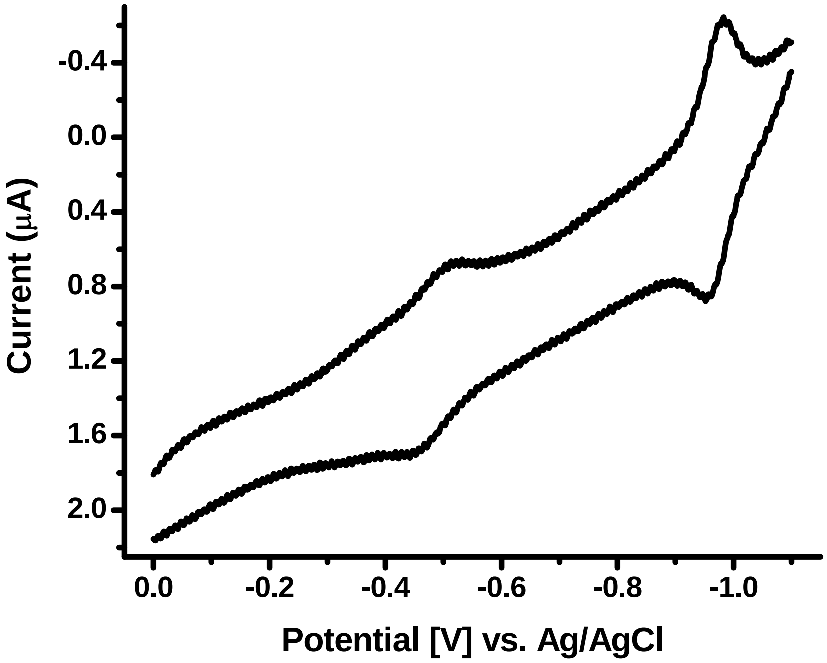

Figure 25: Typical cyclic voltammogram showing Fe^{3+}/Fe^{2+} (approx. 500mV) and Fe^{2+}/Fe^{+} (approx. 950mV) redox couples for the heme moieties in an iNOSoxy immobilized electrode. The effect of Ohmic drop has been removed by mathematically treating the original graph.

2.3.3.2 iNOSoxy-heme Fe^{3+} reduction as a quantifier of immobilization

Typical linear sweep voltammograms for Fe^{3+}-heme reduction obtained at 8mV/s scan rate for a set of the two types of films are shown in Figure 26. We observe a comparable Faradaic charge transfer by electrodes modified with linear & branched PEI. In average, we find that iNOSoxy films constructed using linear PEI transfer nearly the same amount of electrons as films constructed using branched PEI as matrix (approx. 55 nC for branched PEI based films vs. approx. 62 nC for linear PEI based films) as shown in Figure 27. Here, the same electrode has been modified with alternating PEI/iNOSoxy monolayers where one set of data were obtained using a linear PEI/iNOSoxy film and the other using a branched PEI/iNOSoxy film.

Previously, AFM-based cluster analysis showed larger clusters after incubation in iNOSoxy on branched PEI matrix. If this translates directly into active catalyst concentration on an electrode surface, the observation must be a higher charge transfer on branched PEI. The reason for the comparable integrals with approximately the same charge transfer, despite higher loading in branched PEI, is not clear at this point. However, it is possible that orientation of adsorbed protein units versus the electrode surface for linear and branched PEI plays a role in electron transfer, which affects the sampling of iNOSoxy units during the voltammetric scans in the two cases. However, this potential change of orientation in the two cases would not affect iNOS activity in terms of NO synthesis, which explains the results observed in terms of fluxes of NO measured in the previous section

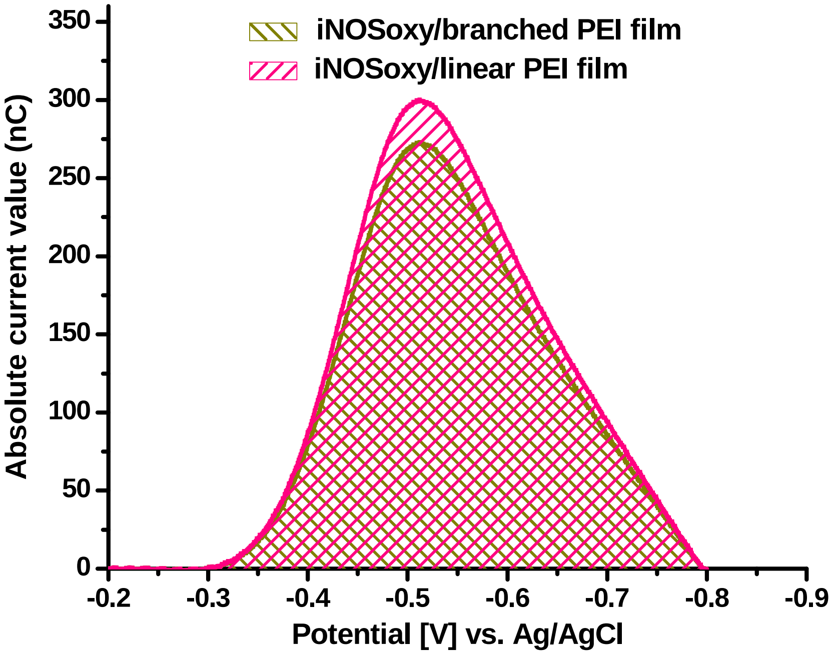

Figure 26: Integrals of characteristic Fe^{3+} reduction in $8mV.s^{-1}$ linear sweep voltammograms for iNOSoxy/PEI films adsorbed on linear PEI and branched PEI. Thin films immobilized from iNOSoxy solution at pH 8.6.

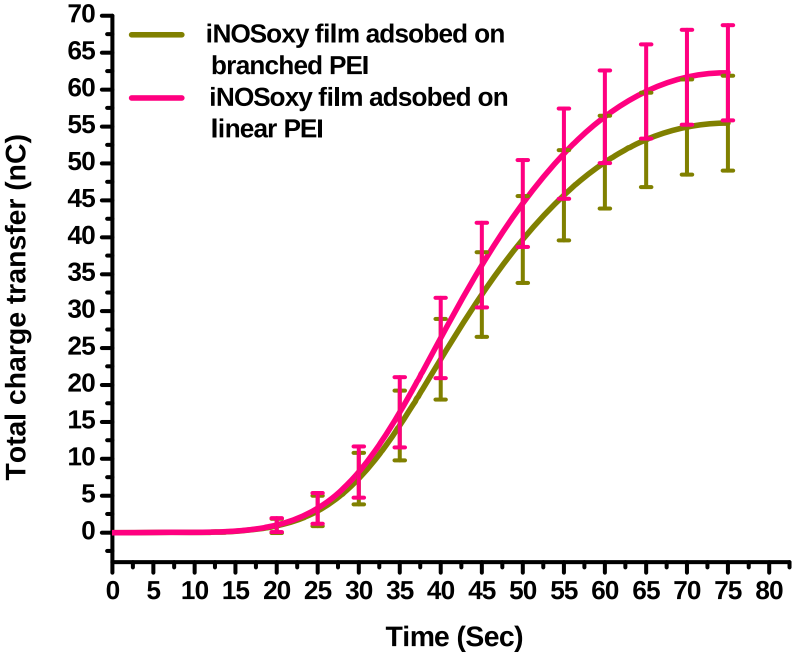

Figure 27: Average of integrals of the characteristic Fe^{3+} reduction in 8mV.s^{-1} linear sweep voltammograms for iNOSoxy/PEI films adsorbed on linear PEI and branched PEI. Standard deviation based on data for the same batch of electrodes immobilized at pH 8.6 (N=5).

2.3.3.3 Catalytic reduction of NO by iNOSoxy immobilized on branched and linear PEI

Addition of NO to the solution results in a catalytic peak around -0.9V vs. Ag/AgCl. In line with previous studies [22, 23], the catalytic current observed, is proportional to NO concentration. Figure 28 shows the peaks of nitric oxide catalytic reduction mediated by iNOSoxy films adsorbed onto linear and branched PEI.

Figure 28 is a comparison of peak catalytic currents (I_{PC}) for NO reduction by iNOSoxy immobilized electrodes. Peak catalytic currents (I_{PC}) for NO reduction by iNOSoxy immobilized electrodes are comparable between linear PEI and branched PEI based thin films for each NO concentration. For example, in Figure 28, average I_{PC} values for NO reduction by thin films of iNOSoxy adsorbed onto linear PEI and branched PEI are 9.8 μA and 10.1 μA respectively, for 120 μM NO concentration. We showed previously (section 2.3.3.2; Figures 26 & 27) that integral of voltammogram obtained in the absence of substrate can be comparison of surface-bound active catalyst concentration with regards to iNOSoxy/PEI on PG electrodes. When substrate NO is present, current, i.e., the rate of charge transfer by the enzyme in catalytic reduction, becomes a direct measurement of enzyme kinetics.

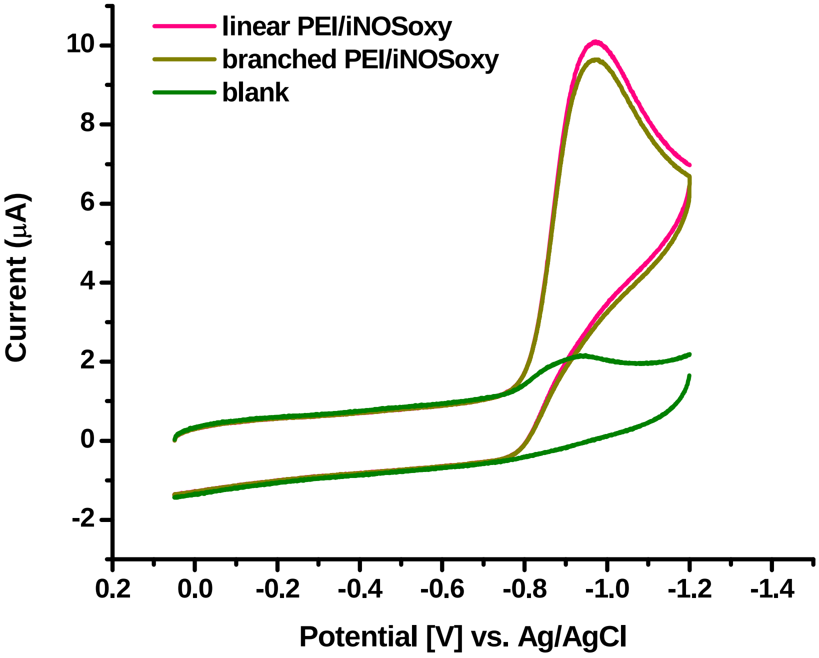

Figure 28: Cyclic voltammogram (200 mV.s^{-1}) for catalytic NO reduction iNOSoxy immobilized on linear PEI and branched PEI, measured at the same NO concentration (120 μM). Immobilization pH is 8.6.

2.3.3.4 Michaelis-Menten kinetics

According to the Michaelis-Menten model, the rate of an enzyme catalyzed reaction denoted by V, is given as follows.

$$V = \frac{V_{Max} \times [S]}{k_M + [S]} \tag{2.1}$$

V_{max} is the maximum rate of substrate turnover, k_M is the substrate concentration at half maximum of the rate of conversion, and, k_{cat} is the turnover number. In the electrochemical form, the rate of catalysis is I_{cat} measured in the voltammetric scan. According to Michaelis-Menten model, I_{cat} is given as follows.

$$I_{cat} = \frac{nFA\Gamma k_{cat} \times [S]}{k_M + [S]} \tag{2.2}$$

Γ is the surface active catalyst concentration, A is the active surface area electrode, and, F is the Faraday constant. While [S] is the substrate concentration, k_{cat} denotes the turnover number. Therefore, typical enzyme saturation kinetics can be observed in a plot of the normalized catalytic current against substrate (NO) concentration. Figure 29 shows the Michaelis-Menten plot for the electrodes modified using linear and branched PEI as matrices and iNOSoxy as the active layer. Michaelis-Menten non-linear curve fitting derives k_M and k_{cat} for the two sets of data, representing the conditions of immobilization and activity.

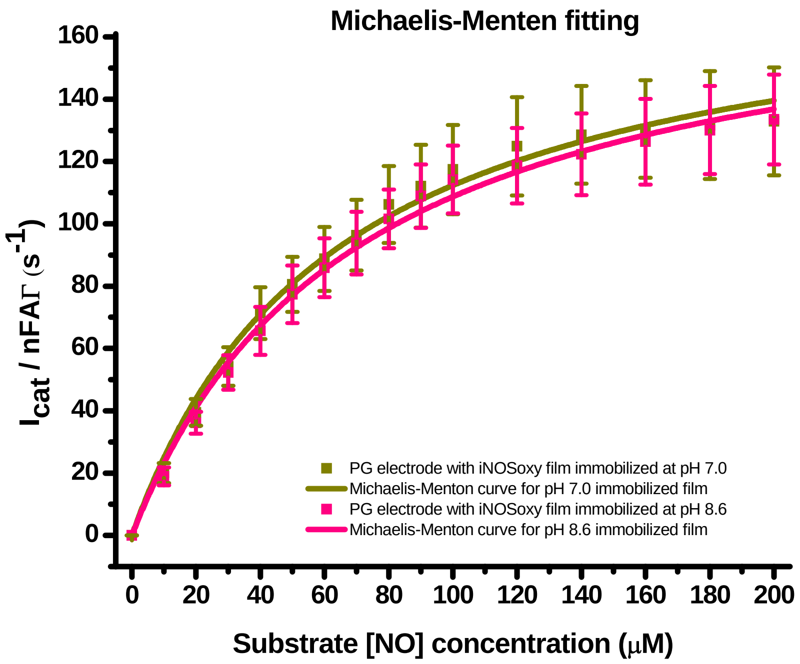

Figure 29: Average catalytic peak current for NO reduction at the surfaces of thin films of iNOSoxy adsorbed at pH 8.6 onto linear PEI and branched PEI. Standard deviation based on data for the same batch of electrodes immobilized using linear and branched PEI (N=5).

iNOSoxy films grown on branched PEI and linear PEI show comparable turnover rates. A slight decrease in the rate of catalysis is observable for the branched PEI based thin films, possibly due to the hindered electron shunt resulting from stacked iNOSoxy units. Non-linear fitting of observed traces using the Michaelis-Menten kinetic model yields the k_M and k_{cat} values for the two films shown in table 2.

Type of PEI used for iNOSoxy Immobilization	k_M (μM)	k_{cat} (s^{-1})
Linear PEI	69.6±4.8	184.4±5.3
Branched PEI	63.7±5.1	184.0±5.9

Table 2: Extracted Michaelis-Menten parameters from non-linear regression fitting using Michaelis-Menten model

Michaelis-Menten saturation kinetics do not show a significant difference in the rate of catalysis observed, for the iNOSoxy films immobilized on linear PEI or branched PEI. Our previous work showed a significant change in the rate of catalysis and different k_M and k_{cat} values, when the iNOSoxy/PEI films were immobilized at different pH. This was attributed to the possible structural distortions of the protein that lead to changes in dynamic motions of the enzyme [24-27]. In the current work, iNOSoxy is adsorbed at pH 8.6 for both linear and branched PEI based thin films. Therefore, the enzyme structure remains potentially unaffected when the enzyme is immobilized on either the linear PEI or the branched PEI, which explains the comparable kinetic parameters K_M and k_{cat} of the two sets of iNOSoxy films adsorbed onto linear PEI and branched PEI.

2.4 Conclusion

This chapter explored the effect of PEI structure (linear vs. branched) on iNOSoxy loading in LbL films. We used branched PEI to modulate the iNOSoxy loading on PEI layers. We report higher activity by the thin films formed on branched PEI compared to thin films built on linear PEI. The activity of thin films described in this chapter is comparable to the activity of alternating (3)NOS-(3)PEI multilayer thin film based LbL method.

The specific focus of this chapter has been to explore the use of polymer branching and the corresponding increase of polymer charge density to optimize enzyme loading on PEI. Active iNOSoxy concentration in thin films explored by electrochemical data implies comparable enzyme loading onto the outermost layer in linear and branched PEI based thin films. However, the AFM imaging of films made with branched PEI suggests higher density of packed enzyme clusters compared to smaller clusters in the case of films made with linear PEI. Assay based activity results confirm the higher loading onto branched PEI based films compared to linear PEI based films.

2.5 Reference

1. Walford, G., Locallzo, J., *Nitric oxide in vascular biology.* Journal of Thrombosis and Haemostasis, 2003. **1**(10): p. 2112-2118.

2. Ignarro, L.J., *Biological actions and properties of endothelium-derived nitric oxide formed and released from artery and vein.* Circulation Research, 1989. **65**(1): p. 1-21.

3. Bjellqvist, B., Basse, B., Olsen, E. and Celis, J.E., *Reference points for comparisons of two-dimensional maps of proteins from different human cell types defined in a pH scale where isoelectric points correlate with polypeptide compositions.* Electrophoresis, 1994. **15**(3-4): p. 529-539.

4. Gasteiger E., H.C., Gattiker A., Duvaud S., Wilkins M.R., Appel R.D., Bairoch A., *Protein Identification and Analysis Tools on the ExPASy Server*, ed. J.M. Walker. The Proteomics Protocols Handbook, Humana Press (2005).

5. Bjellqvist, B., Hughes, G.J., Pasquali, Ch., Paquet, N., Ravier, F., Sanchez, J.-Ch., Frutiger, S., Hochstrasser, D.F., *The focusing positions of polypeptides in immobilized pH gradients can be predicted from their amino acid sequences.* Electrophoresis, 1993. **14**(10): p. 1023-1031.

6. Meier, U. and C.W. Schläpfer, *Interaction between Cl− and linear and branched polyethyleneimine in aqueous solution studied by 35Cl- and 37Cl-NMR.* Berichte der Bunsengesellschaft für physikalische Chemie, 1998. **102**(8): p. 1011-1018.

7. Wu, C.-b., J.-y. Hao, X.-m. Deng, and Y. Liu, *Random branched poly(hydroxyetheramine): a novel polycation with proton sponge effect and high density of discrete charge.* Polymer Bulletin, 2008. **60**(5): p. 635-645.

8. Boussif, O., F. Lezoualc'h, M.A. Zanta, M.D. Mergny, D. Scherman, B. Demeneix, and J.P. Behr, *A versatile vector for gene and oligonucleotide transfer into cells in culture and in vivo: polyethylenimine.* Proceedings of the National Academy of Sciences, 1995. **92**(16): p. 7297-7301.

9. Mateos-Timoneda, M.A., M.C. Lok, W.E. Hennink, J. Feijen, and J.F. Engbersen, *Poly(amido amine)s as gene delivery vectors: effects of quaternary nicotinamide moieties in the side chains.* ChemMedChem, 2008. **3**(3): p. 478-86.

10. Voigt, U., V. Khrenov, K. Tauer, M. Hahn, W. Jaeger, and R.v. Klitzing, *The effect of polymer charge density and charge distribution on the formation of multilayers.* Journal of Physics: Condensed Matter, 2003. **15**(1): p. S213.

11. Drovetskaya, T.V., E.F. Diantonio, R.L. Kreeger, J.L. Amos, and D.P. Frank, *New high-charge density hydrophobically modified cationic HEC polymers for improved co-deposition of benefit agents and serious conditioning for problem hair.* J Cosmet Sci, 2007. **58**(4): p. 421-34.

12. Shin, Y., J.E. Roberts, and M.M. Santore, *The relationship between polymer/substrate charge density and charge overcompensation by adsorbed polyelectrolyte layers.* J Colloid Interface Sci, 2002. **247**(1): p. 220-30.

13. Stuehr, D.J., *Purification and properties of nitric oxide synthase.* Methods in Enzymology, 1996. **268**: p. 324-333.

14. Tiso, M., Strub, A., Hesslinger, C., Kenney, C.T., Boer, R., Stuehr, D.J., *BYK191023 (2-[2-(4-Methoxy-pyridin-2-yl)-ethyl]-3H-imidazo[4,5-b]pyridine) is an NADPH- and time-dependant irreversible inhibitor of inducible nitric oxide synthase.* Molecular Pharmacology, 2008. **73**(4): p. 1244-1253.

15. Wang, Z., Wei, C., Stuehr, D.J., *A Conserved Tryptophan 457 Modulates the Kinetics and Extent of N-Hydroxy-l-Arginine Oxidation by Inducible Nitric-oxide Synthase.* The Journal of Biological Chemistry, 2002. **277**(15): p. 12830-12837.

16. Rusling, J.F., Nassar, A.F., *Enhanced electron transfer for myoglobin in surfactant films on electrodes.* Journal of the American Chemical Society, 1996. **115**(25): p. 11891-11897.

17. Waitumbi, J. and A. Warburg, *Phlebotomus papatasi saliva inhibits protein phosphatase activity and nitric oxide production by murine macrophages.* Infect Immun, 1998. **66**(4): p. 1534-7.

18. Jun, H.-W., TaiteL.J., West, J.L., *Nitric oxide-producing polyurethanes.* Biomacromolecules, 2005. **6**(2): p. 838-844.

19. Matl, F.D., A. Obermeier, S. Repmann, W. Friess, A. Stemberger, and K.D. Kuehn, *New anti-infective coatings of medical implants.* Antimicrob Agents Chemother, 2008. **52**(6): p. 1957-63.

20. Miller, P.E., Carlton, D., Deierhoi, M.H., Redden, D.T., Allon, M. , *Natural history of arteriovenous grafts in hemodialysis patients.* American Journal of Kidney Diseases, 2000. **36**(1): p. 68-74.

21. Vaughn, M.W., L. Kuo, and J.C. Liao, *Estimation of nitric oxide production and reaction rates in tissue by use of a mathematical model.* Am J Physiol, 1998. **274**(6 Pt 2): p. H2163-76.

22. Bayachou, M., Abou-Diwan, C. , *US Patent # 2009/073643.* 2009.

23. Immoos, C.E., Chou, J., Bayachou, M., Blair, E., Greaves, J., Farmer, P.J., *Electrocatalytic reductions of nitrite, nitric oxide, and nitrous oxide by thermophilic cytochrome P450 CYP119 in film-modified electrodes and an analytical comparison of its catalytic activities with myoglobin.* Journal of the American Chemical Society, 2004. **126**(15): p. 4934-4942.

24. Agarwal, P.K., Geist, A., Gorin, A., *Protein dynamics and enzymatic catalysis: investigating the peptidyl-prolyl cis-trans isomerization activity of cyclophilin A.* Biochemistry, 2004. **43**(33): p. 10605-10618.

25. Agarwal, P.K., Billeter, S.R., Rajagopalan, P.T,, Benkovic, S.J., Hammes-Schiffer, S., *Network of coupled promoting motions in enzyme catalysis.* Proc. Natl. Acad. Sci., 2002. **99**(5): p. 2794-2799.

26. Yang, L.W., Bahar, I., *Coupling between catalytic site and collective dynamics: A requirement for mechanochemical activity of enzymes.* Structure, 2005. **13**(6): p. 893-904.

27. Tousignant, A., Pelletier, J.N. , *Protein motions promote catalysis.* Chemistry & Biology, 2004. **11**(8): p. 1037-1042.

CHAPTER III: INDUCIBLE NITRIC OXIDE SYNTHASE OXYGENASE (iNOSoxy) ENCAPSULATED IN ELECTROSPUN FIBER SCAFFOLDS AND MATS

3.1 Introduction

3.1.1 Electrospinning

Electrospinning is an economical method for fabricating scaffolds and mats that can host and release therapeutic agents while functioning as support structures for tissue and cell growth. Electrospinning produces polymer fibers with diameters in the nano to micrometer range. Electrospinning is used efficiently in a variety of tissue-engineering applications for different types of scaffolds [1-4], controlled drug-delivery platforms [5], and sensors [6, 7]. For example, materials such as DNA has been successfully embedded into and released from electrospun scaffolds, where the DNA has been used for transfection [8]. In our current work, electrospun scaffolds and mats encapsulate an enzyme, nitric oxide synthase, involved in the generation and release of nitric oxide (NO) upon contact with the buffer containing NOS reaction cocktail. Release of NO is useful for the scaffold to counteract thrombogenesis, which could be an advantage for scaffolds whose primary function is acting as a solid support for cells in regenerative medical applications.

A homogenized electrospinning mixture of polymer, solvent and active ingredient (the enzyme in our case) is contained in a syringe. This is horizontally driven at a flow rate of several milliliters per hour to elute from the needle tip. The eluting mixture, rather than falling along gravity, is attracted to a mandrel, due to a potential difference applied between the needle and the mandrel. The ejecting stream of electrospinning mixture forms a Taylor cone at the edge of the needle, before thinning-out along its direction [9, 10]. Typical voltage biases range from 5-30 kV and the air-gap distance between the needle and collecting mandrel range from 15-30 cm. On elution, the polymer mixture with its constituents is driven as a continuous stream of wet fiber. The electrospinning chamber facilitates the evaporation of solvent component from the spinning polymer solution. As the solvent evaporates, the jet solidifies, forming a polymer fiber. The spinning mandrel collects the fiber and forms either a mat or a scaffold depending on the shape and size of the mandrel.

The encapsulation of active agents in electrospun fibers can be achieved in two major electrospinning methods: (1) coaxial electrospinning and, (2) emulsion electrospinning. Coaxial electrospinning uses two separate spinning streams of fluids for the electrospinning process. A polymer shell and a core consisting of encapsulating ingredient are pumped through separate feeder lines, toward the tip of the coaxial double – bore needle. Coaxial electrospinning has been used to contain bovine serum albumin (BSA) in polycaprolactone [11, 12]. A number of pharmaceutical agents such as tetracycline hydrochloride [5], ibuprofen [13], and rifampicin [14] have been coaxially electrospun into encapsulating fibers, which are used to release the drug at targeted interventions.

The emulsion electrospinning method involves an aqueous solution containing typically the active ingredient in a non-polar polymer-solvent combination. The active component, iNOSoxy, and the polymer form a biphasic emulsion that is fed into a single-bore needle. When a biphasic emulsion is used for electrospinning, it results in the encapsulation of an aqueous pocket called a 'node' within the polymer microfibers. Growth factors [15] and different proteins such as cytochrome C [16] have been successfully electrospun using emulsion electrospinning to enhance biocompatibility. In this work, we explore conditions under which iNOSoxy can be embedded in aqueous pockets entrapped in electrospun polymer matrices. The long term goal of this work is to develop scaffolds and mats that demonstrate antithrombogenic activity to counteract thrombosis cascade observed in scaffolds.

3.1.2 The polymers

Polycaprolactone (PCL, Fig. 30(a)) is a hydrophobic polymer used in the fabrication of electrospun fiber scaffolds. PCL based scaffolds have been designed for the delivery of therapeutic agents [17], and as cell infiltration scaffolds systems [18]. Caprolactone-based polymers undergo hydrolysis in mammalian physiological conditions. For certain implantable devices, this is beneficial where implants are expected to safely degrade and leave the body after the end of its functional lifespan. Hydrolysis in biological conditions proceed via the cleavage of the ester bond and therefore can be affected by pH and temperature [6]. Studies of mouse fibroblast adhesion onto electrospun scaffolds have also shown the biocompatibility of PCL [19].

Polyvinyl alcohol (PVA, Figure 30(b)) is a water-soluble polymer used in electrospinning mats and scaffolds. PVA in electrospun implantable systems showed resistance against implant infection [20]. Electrospun PVA fiber mats are important as dissolving drug delivery systems that leave no harmful residue [21]. However, when longer functionality is desired, cross-linking can increase the stability of PVA fibers, which makes them resist degradation in aqueous systems, including body fluids [22, 23]. However, release and activity of embedded ingredients could be affected by the cross-linking process [24].

Polyethylene-co-vinyl acetate (PEVA, Figure 30(c)) is another hydrophobic polymer used in fabricating electrospun scaffolds for drug delivery [17]. PEVA is inert and non-biodegradable under human physiological conditions. *In-vivo* experiments have shown PEVA implants to be biocompatible, with evidence of tissue encapsulation of implants [25].

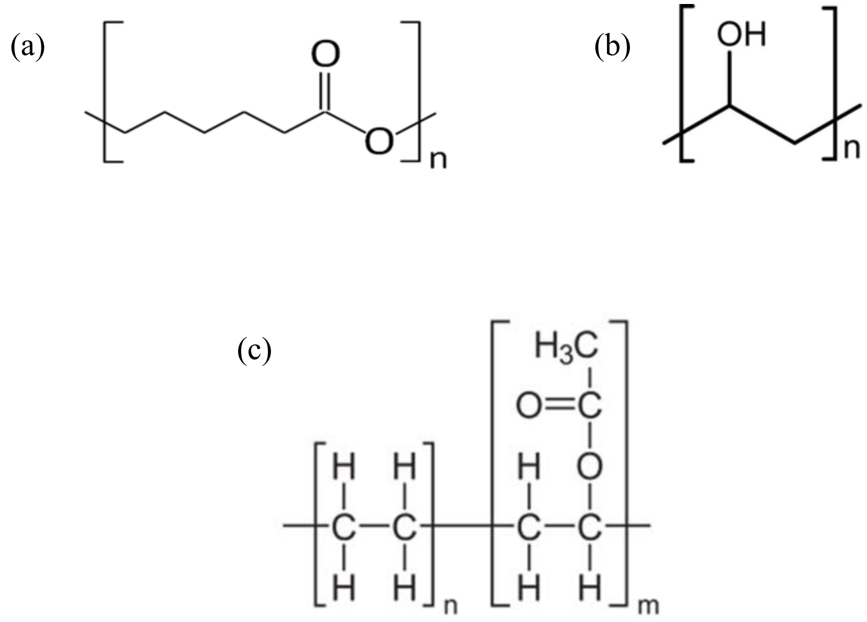

Figure 30: Structures of a) polycaprolactone, b) polyvinyl alcohol and, c) polyethyl-vinyl acetate.

3.2 Experimental

3.2.1 iNOSoxy structural study by FTIR in different organic solvent mixtures used in electrospinning

We used FTIR analysis to characterize iNOSoxy emulsified in different solvents used in the polymer/solvent mixture. We used the diamond ATR crystal assembly (PIKE technologies) coupled to a FTIR (Varian Digilab Scimitar series FTS 2000). Aliquots of 10 µl of ~100 µM iNOSoxy in EPPS buffer were combined with volumes of 60, 70, 80 and 90 µl of either chloroform or acetone, and homogenized. The blank measurement was obtained by placing a 100 µl drop of the respective solvent on the ATR crystal. Aliquots of 100 µl of homogenized iNOSoxy-solvent mixtures were placed on the crystal to acquire FTIR spectra.

3.2.2 Activity of iNOSoxy in polymer mixture before electrospinning

When bathed in buffer containing iNOSoxy substrate cocktail, the enzyme catalyzes the production and release of NO [26, 27]. Similar to the assay methods used in sections 1.2.6 and 2.2.3, we used the Griess reagent system to monitor NO release in electrospinning mixture in order to characterize iNOSoxy activity. The combined iNOS/polymer mixture (25 µl of enzyme in 475 µl in polymer mix) was vortexed at several 3-second cycles. An aliquot of 800 µl of EPPS buffer was added to the vortexed polymer-enzyme mixture. The combination was again vortexed in the same manner, to partially extract iNOSoxy from the emulsified spinning mixture into the buffer phase, which was used for testing enzyme activity. A volume of 300 µl of EPPS layer was transferred into a 500 µl cuvette. Aliquots of 300 µl each of Griess reagent (sulfanilamide and NED, Promega) were added to the cuvette. After 10 minutes, UV-Vis spectra were recorded. In addition, the EPPS layer used to re-extract the enzyme was removed from the vial containing the iNOSoxy/polymer emulsion. The remaining iNOSoxy/polymer mixtures were separated by centrifugation in 1 ml Microcon® filters at 10,000 rpm for 1 minute. The separated enzyme portions remaining in residue were washed and incubated with 500 µl of NOS reaction cocktail for 15 minutes. NO output was measured using the Griess assay to determine the activity of trapped enzyme. A total NO output, produced by both the extracted and trapped iNOSoxy was measured, and compared against an output of NO by a native enzyme aliquot used in the characterization.

3.2.3 Electrospinning apparatus

A sketch of the electrospinning apparatus is shown in Figure 31. The apparatus consists of a syringe, typically 5 cm^3, containing the spinning mixture. The syringe is mounted on, and driven by a syringe pump (model 100 KD scientific Inc., New Hope, PA). The needle (gauge range of 16-20) is cut flat, to facilitate the Taylor cone formation [9, 10]. A high voltage DC power supply (Spellman, CWE1000R, Spellman High Voltage Electronics Corp., Hauppauge, NY) applies the bias between needle and the collecting mandrel. The mandrels are made of steel or coated alloys and are grounded. The oscillation and the rotation of the mandrel are driven by computer numeric control motors. The oscillation is made to glide on a linear drive perpendicular to the direction of ejection. The electrospinning assembly is contained in a cage made of commercial plexiglass with evacuation lines fitted for removing volatile solvent. Ambient conditions such as humidity and temperature are carefully monitored.

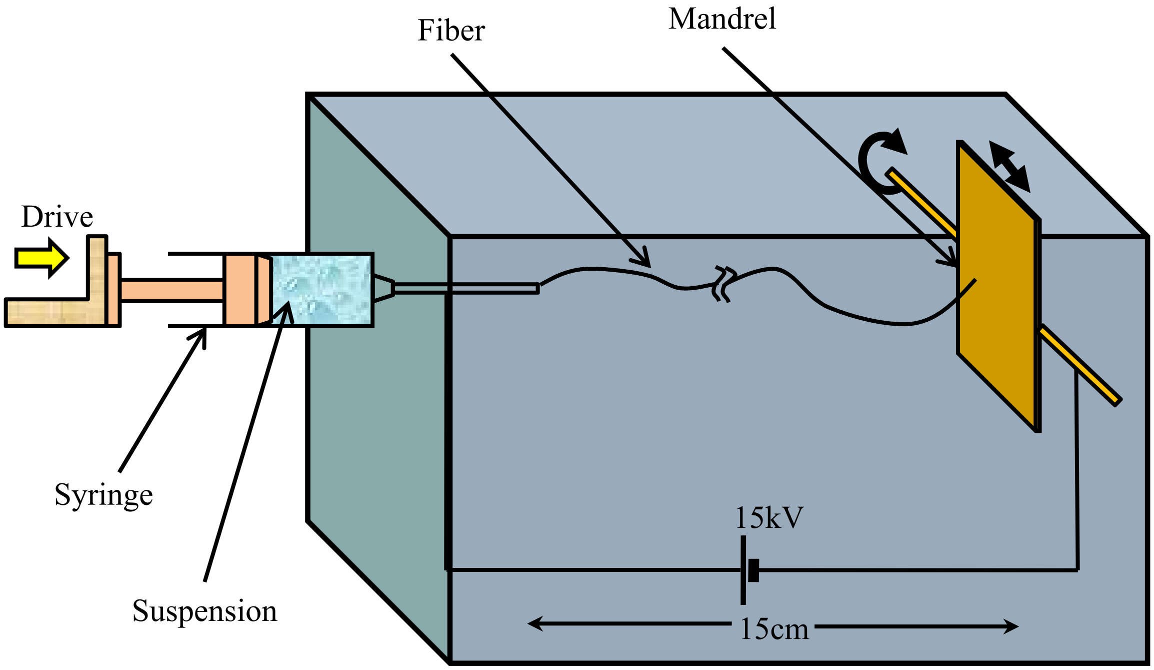

Figure 31: A schematic representation of a typical electrospinning apparatus.

3.2.4 Preparation of polymer solution and electrospinning parameters

A mass of 2.2 g of polycaprolactone (70,000–90,000 MW, Sigma Aldrich by GPC) was dissolved in 15 ml of chloroform (Sigma) overnight to achieve a homogenous solution of ~10% w/w PCL. For polyethylene-co-vinyl acetate, (Sigma Aldrich), a mass of 6.0 g was dissolved in 29 ml of chloroform (Sigma) overnight to achieve a homogenous solution of ~14% w/w PEVA. A mass of 2 g of polyvinyl alcohol (99%, hydrolyzed, Sigma Aldrich) was dissolved in 20 ml of DI water to make ~10% w/w solution of PVA.

We selected a ratio of 20:1 v/v for polymer-solvent to iNOSoxy throughout the experiments, after examining trials for both lower and higher ratios. A volume of 950 µl of polymer solution was pipetted into a capped conical vial. To this, an aliquot of 50 µl of 100 µM iNOSoxy in EPPS buffer was added. The suspension was vortexed in several 2-5 second cycles. The resultant 1 ml homogenized mixture was loaded into the 5 cm^3 syringe for electrospinning.

Polymer / solvent	10% w/w PCL in chloroform	14% w/w PEVA in chloroform	10% w/w PVA in water
Polymer/solvent : iNOSoxy ratio (v/v)	20:1	20:1	20:1
Air-gap distance (cm)	15	30	15
Voltage (kV)	15	15	15
Flow rate (ml/hour)	1.0	3.0	1.0

Table 3: Electrospinning parameters for each polymer/solvent system.

3.2.5 Optical microscopic imaging of electrospun scaffolds and mats

Electrospun microfibers were collected in a glass microscope slides (Fisher Scientific). A number of samples at different distances from the needle were collected and imaged. The purpose was to monitor solvent evaporation along the ejection path and formation of nodes. We used a Nikon Eclipse TS100 inverted optical microscope using 10X, 20X and 40X magnifications. Images were captured using a digital camera connected to the ocular. Image analysis and rendering was done using Qscope software.

We used Sudan IV (Sigma) as a staining reagent to observe separation of polar and non-polar phases in the electrospinning process. We used a ratio of 1 mg of Sudan IV per

1 ml of homogenized electrospinning mixture. Optical microscopic images were obtained separately for stained electrospun scaffolds. We also used fluorescein isothiocyanate (FITC) to observe the nodes formed in emulsion electrospinning method where aqueous solvent pockets are encapsulated.

3.2.6 Scanning Electron Microscopic imaging of electrospun scaffolds and mats

We used JEOL JSM-6510LV series Scanning Electron Microscope (SEM) and Inspect F-50 field emission SEM (FE-SEM) for imaging electrospun scaffolds and mats. We used aluminum stubs and square specimen mounts to fix scaffolds and mats for gold sputtering and imaging. We used Quorum EMS (Quorum Technologies) sputter coater for gold sputtering. All cylindrical scaffolds were cut open and mounted on stubs. Image-J64 software was used to analyze the fiber diameters.

3.2.7 Activity of iNOSoxy enzyme embedded in PVA scaffold through Griess reagent system

Several 2 cm × 2 cm non-crosslinked PVA scaffold sections were cut from each batch of the spun fiber scaffolds containing iNOSoxy. The control sample was a section of scaffold that did not have iNOSoxy in its aqueous suspension during the electrospinning process. The scaffold sections were placed in labeled scintillation vials. Volumes of 5 ml of the NOS reaction cocktail containing 250 μM N-hydroxy-L-arginine (NHA), 10 μM tetrahydrobiopterin (H_4B), and 400 µM dithiothreitol (DTT) prepared in 100 mM phosphate buffer adjusted to pH 7.4, were added to each of the vials. The enzyme-catalyzed reaction was triggered at 37˚C by adding hydrogen peroxide to a final concentration of 150 mM. Aliquots of 100 µl of reaction medium were retrieved and combined with 100 µl of each of Griess reagents R1 (sulfanilamide) and R2 (N-(1-naphthyl)ethylenediamaine) (Cayman Chemical Company) in a UV-Vis cuvettes. Absorbance values at 540 nm against the reagent blank were recorded (UV-Vis; Model 8543, Agilent Technologies) after a 10-minute incubation time for all assay aliquots. Concentrations were determined using a standard calibration curve prepared under the same conditions.

3.2.8 Activity of iNOSoxy enzyme embedded in scaffold using a fluorometric method

Our preliminary activity characterizations on electrospun fiber based iNOSoxy prompted the use of a more sensitive assay than the Griess assay system. We used the DAF-FM (4-amino-5-methylamino-2',7'-difluorofluorescein) diacetate assay [28, 29]. Figure 32 is a schematic representation of the general reaction of DAF-FM based fluorescence assay used to determine NO concentration.

Scaffold sections of 2 cm × 2 cm were cut from each batch of the iNOSoxy enzyme containing PCL and PEVA spun fiber scaffolds. For the control experiment, we used a section of scaffold electrospun without iNOSoxy. The scaffold sections were placed in labeled scintillation vials. Volumes of 1 ml of the reaction cocktail containing 250 µM N-hydroxy-L-arginine (NHA), 10 µM tetrahydrobiopterin (H_4B), and 400 µM dithiothreitol (DTT) dissolved in 100 mM phosphate buffer medium and adjusted to a final pH value of

7.4 were added to each of vial. The enzyme catalyzed reaction was activated by adding hydrogen peroxide to a final concentration of 150 mM. Scaffolds were incubated at 37˚C. Aliquots of 150 µl of reaction media were taken at 2, 4, 8, 12, 24, 48 & 72 hour lapse times for analysis. The reaction aliquots were placed in opaque microplate wells. Aliquots of 150 µl of 10 µM DAF-FM diacetate (4-amino-5-methylamino- 2′,7′-difluorofluorescein diacetate, Molecular Probes Inc.) were added to each well. We used Hitachi f-7000 fluorescence spectrophotometer. Excitation wavelength was set at 495 nm, while emission was monitored at 515 nm. A standard calibration curve for the NO concentration range from 0.1 µM to 12.0 µM was used to measure NO released in reactions catalyzed by iNOSoxy in electrospun scaffolds and mats.

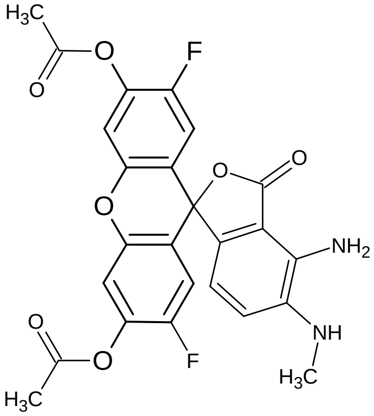

DAF-FM Diacetate

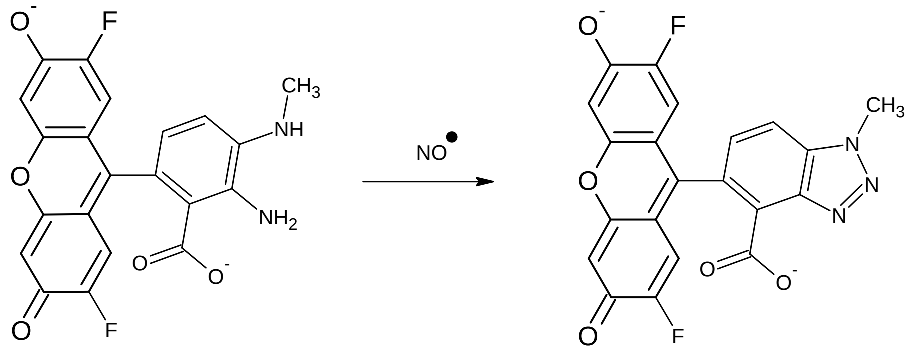

DAF-FM

Benzotriazole derivative
(fluorescent)

Figure 32: Reaction scheme for the detection of NO by DAF-FM diacetate.

3.3 Results and Discussion

3.3.1 FTIR analysis for protein structure in organic solvent systems

We monitored amide I (1650 cm^{-1}) and amide II (1550 cm^{-1}) bands [30-32] (Figure 33) as a handle on changes of structural environments and the overall three dimensional protein structure [32, 33] in contact with chloroform. Overall FTIR spectra enabled us to determine chloroform/iNOSoxy volume ratios that retained or minimally affected iNOSoxy structure in the electrospinning medium [34].

3.3.2 Activity of iNOSoxy in polymer mixture before electrospinning

A fraction of iNOSoxy will be denatured in the emulsion, and would not respond to an activity assay. Some of the iNOSoxy in the emulsion was easily extracted and assayed for activity. The remaining fraction entrapped in the emulsion was centrifuged, resuspended and then assayed separately. The activity of iNOSoxy from both fractions are added and provide the total activity for viable iNOSoxy enzymes in the electrospinning emulsion. Figure 33 shows a comparison iNOSoxy activity for each polymer-solvent combination. As expected, enzyme activity is almost retained in aqueous PVA-based polymer combination as shown in Figure 33. The activity of enzyme in the electrospinning mixture of 10% w/w PCL/chloroform is nearly one fifth of iNOSoxy native activity. On the other hand, iNOSoxy from PEVA/chloroform emulsion is about one tenth of native iNOSoxy activity, taken as the control.

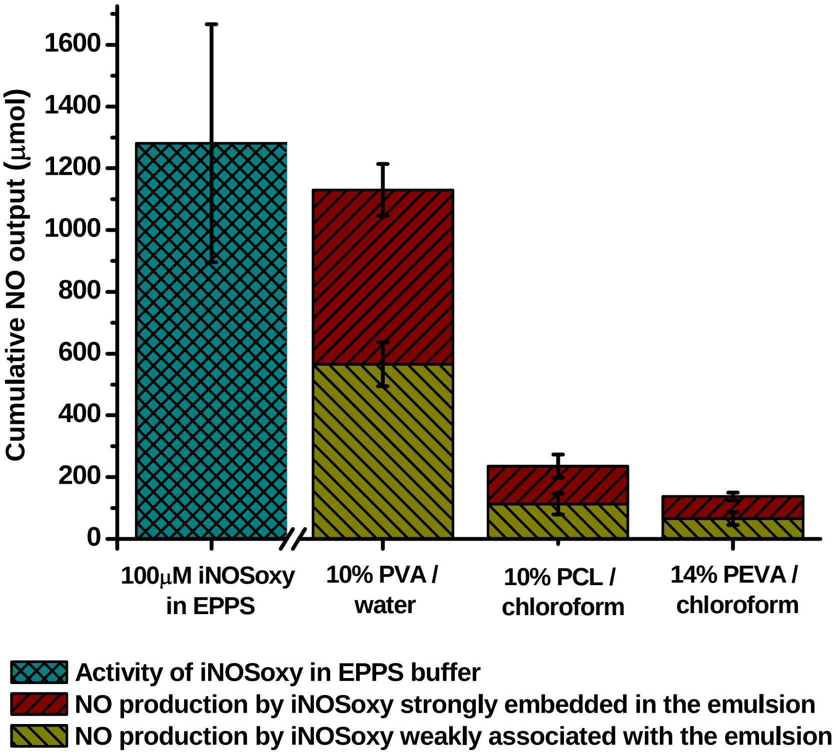

Figure 33: Activity of iNOSoxy prior to electrospinning in three different homogenized polymer/solvent mixtures and iNOSoxy. Control is provided by iNOSoxy enzyme in EPPS buffer. Error bars represent standard deviations in repeated trials (N=3).

3.3.3 Physical characteristics of electrospun fiber scaffolds and mats

Higher w/w ratios of solvent to polymer affect the continuity of the polymer fiber while lower ratios coagulate the spinning mix at the needle due to different viscoelasticity. Using the 1:20 v/v ratio of polymer/solvent to iNOSoxy in buffer, two types of electrospun scaffolds were fabricated and used for characterization.

The main type of scaffold we fabricated was the vessel-like tubular electrospun scaffold. We used the 2 mm and 4 mm diameter smaller mandrels to spin PCL scaffolds of this type. Scaffolds are retrieved by sliding along the mandrel. Figure 34 shows an image of a typical PCL scaffold. The resulting material is cut into sections and used for activity characterization and imaging. PCL scaffolds are relatively rigid mechanically and returns to original form easily after distortion of its cylindrical shape. Figure 35 shows a section of PEVA scaffold. Unlike PCL, PEVA scaffolds tend to adhere to mandrel and other surfaces. The original scaffold is cut along a line parallel to spinning axis. The other type is the electrospun fiber mat. Figure 36 shows a PVA scaffold spun using the larger 50 mm diameter mandrel. Sections ranging from 5 cm × 5 cm to 2 cm × 2 cm were used for activity assays, while smaller sections were used for imaging.

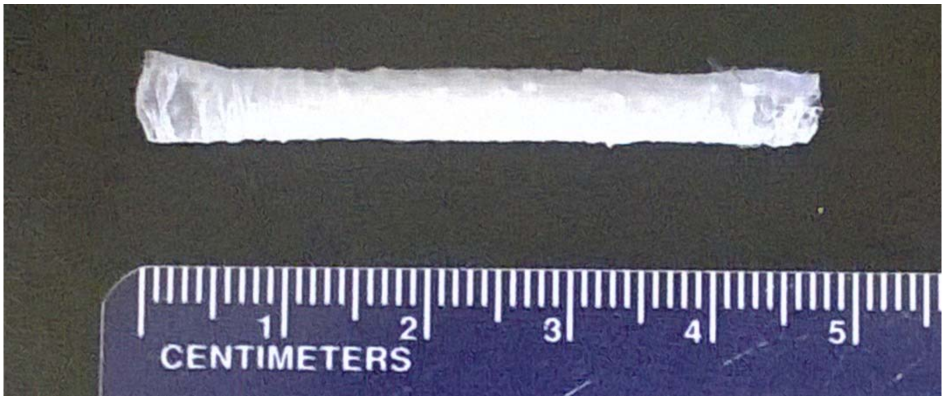

Figure 34: A photograph of a section of PCL scaffold retrieved from the small 4 mm mandrel immediately after electrospinning. Electrospinning conditions: Air-gap distance: 15 cm, Potential: 15 kV, Electrospinning emulsion ratio (v/v): 20:1 (Polymer mixture : iNOSoxy containing buffer), Flow rate 1 ml/hr.

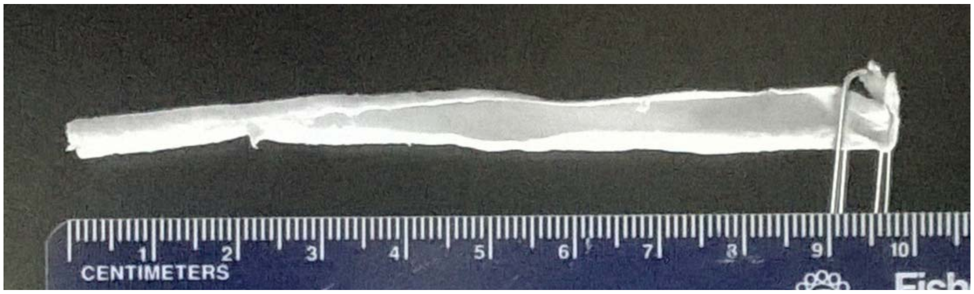

Figure 35: A photograph of a section of PEVA scaffold cut open and retrieved from the small 4 mm mandrel after electrospinning. Electrospinning conditions: Air-gap distance: 30 cm, Potential: 15 kV, Electrospinning emulsion ratio (v/v): 20:1 (Polymer mixture : iNOSoxy containing buffer), Flow rate 3 ml/hr.

Figure 36: A photograph of a section of PVA scaffold retrieved from the large mandrel immediately after electrospinning. Electrospinning conditions: Air-gap distance: 15 cm, Potential: 15 kV, Electrospinning emulsion ratio (v/v): 20:1 (Polymer mixture : iNOSoxy containing buffer), Flow rate 1 ml/hr.

Both PCL and PEVA based scaffolds maintain their physical form in aqueous solutions, for all activity characterizations carried-out in EPPS buffer. PVA scaffolds dissolve considerably in aqueous reaction cocktail where activity assays were carried out. Initially, the original mats coalesce into polymer aggregates that continue to degrade and dissolve. Crosslinked PVA mats do not dissolve. Both the crosslinked and non-crosslinked forms of PVA could be useful, depending on the application. Rapidly dissolving, drug eluting scaffolds and mats have been investigated previously for their specific benefits for PCL based systems [35, 36]. Other polymer systems have also been studied for biodegradable nature of the scaffolds and the accompanying benefits [14].

3.3.4 Optical microscopic imaging

The encapsulation of aqueous pockets in the PCL and PEVA polymer microfiber is driven by the separation of polar aqueous pockets from the non-polar solvent during the electrospinning process. In contrast, PVA shows no clear separation of 'nodes' as expected. This is due to the fact that both the active component, iNOSoxy enzyme and polymer matrix are part of the same aqueous phase.

Figure 37 shows an electrospun microfiber scaffold stained with Sudan IV. Polar aqueous phase containing 'nodes' are shown, which are entrapped in the non-polar PCL polymer microfibers. Sudan IV has been used previously to provide information on the composition of PCL fiber mats [37]. Figure 38 shows optical microscopic images of PVA and PCL microfibers respectively, with embedded iNOSoxy.

Figure 37: Optical microscopic images of PCL microfibers stained with Sudan IV.

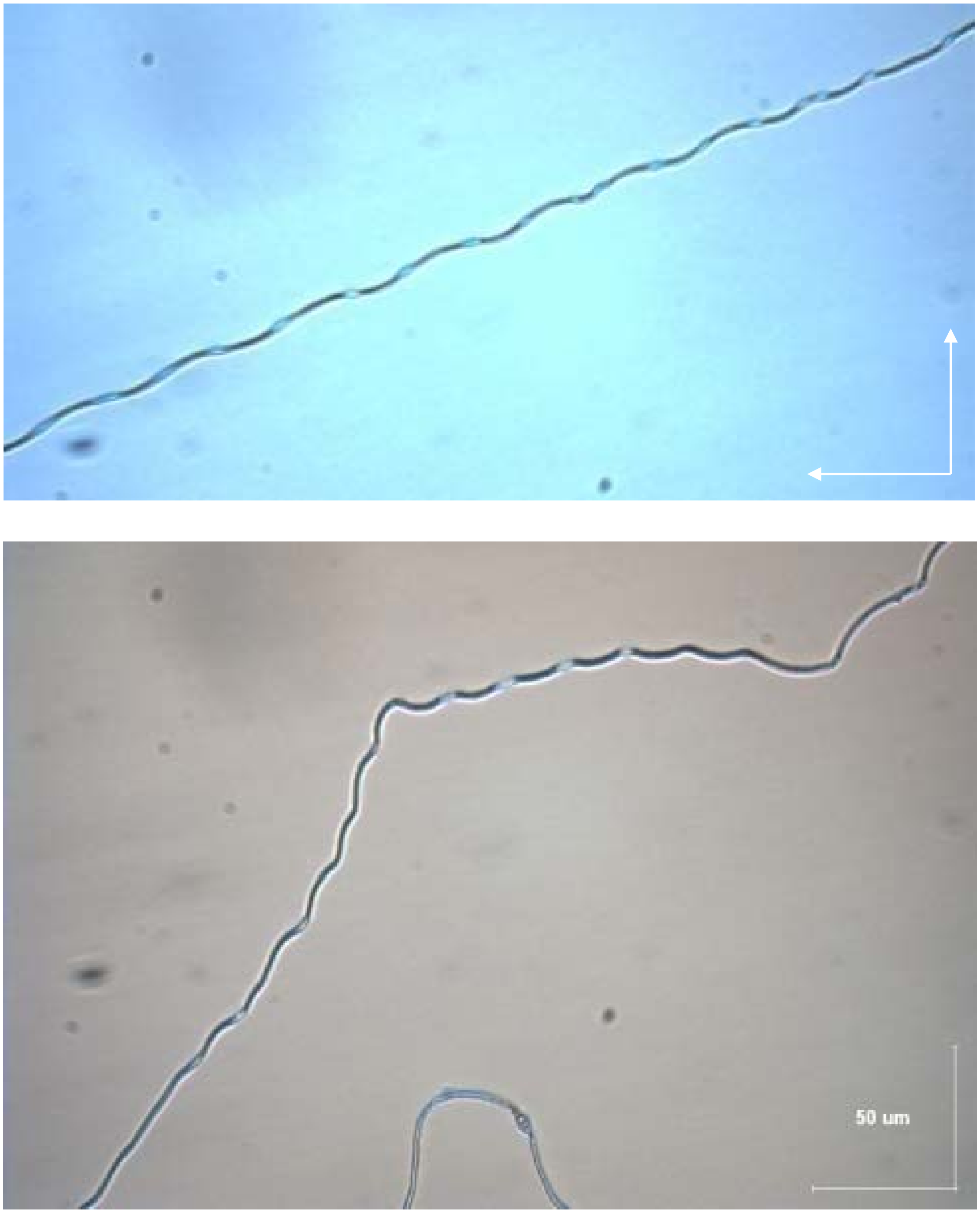

Figure 38: Optical microscopic images of PCL microfibers with encapsulated pockets of iNOSoxy.

Figure 39 shows the fluorescence images of PCL microfibers stained with FITC. With its isothiocyanate group, FITC is known to react and tag proteins [12, 18, 38-40]. The high fluorescence intensity in ‘nodes’ in Figure 39 corresponds to iNOSoxy proteins entrapped in the PCL microfiber.

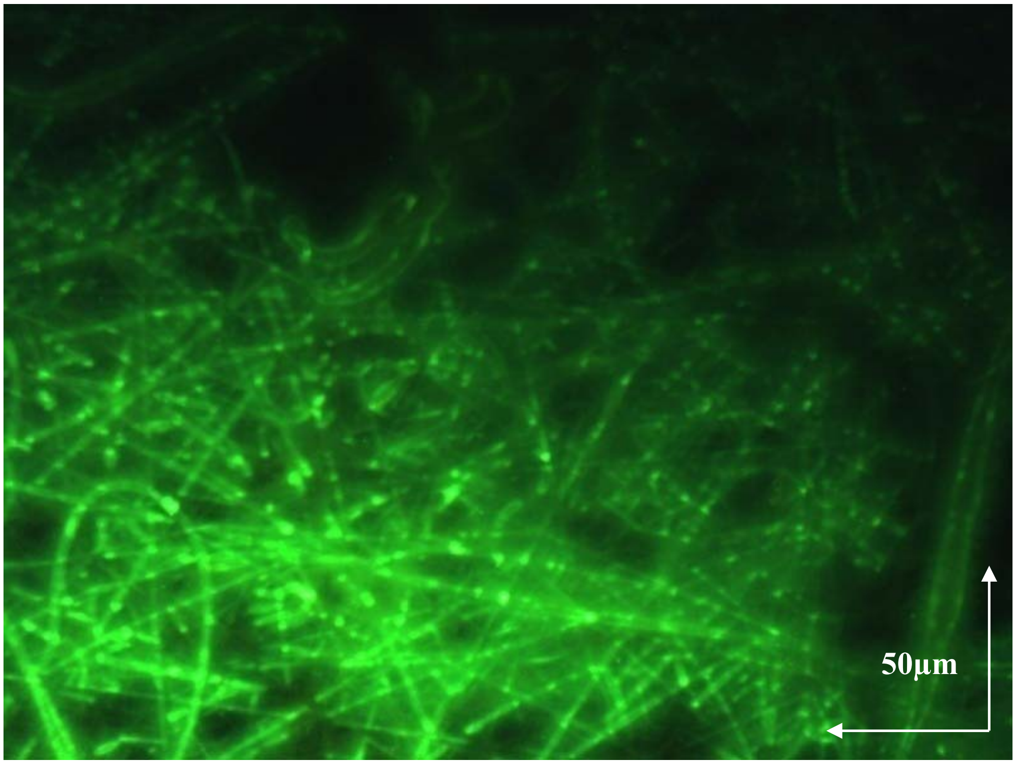

Figure 39: Fluorescence microscopic image of FITC stained PCL electrospun microfibers. Electrospinning conditions: Air-gap distance: 15 cm, Potential: 15 kV, Electrospinning emulsion ratio (v/v): 20:1 (Polymer mixture : iNOSoxy containing buffer), Flow rate 1 ml/hr

3.3.5 Scanning electron microscopic imaging

Scanning electron microscopic (SEM) images help visualize fiber morphology, internal scaffold structures, pore sizes and level of encapsulation [18]. In general, SEM images of the scaffolds show random orientations of fibers. Figure 40(a) and (b) shows successful encapsulation of the aqueous pockets in a PCL microfiber. Average diameter of fibers that successfully encapsulate aqueous pockets is less than few microns.

Figure 41(a) and (b) show SEM images of a section of an electrospun PVA mat. PVA is water soluble, and hence is electrospun in aqueous buffer with iNOSoxy in the same phase. Unlike in a two-phase emulsion electrospinning where pockets are observed, electrospun PVA mats are not expected to show clear separation of entrapped pockets. Instead, the active component - iNOSoxy - is distributed evenly within the fibers.

Image-J64 software was used to measure fiber diameter of PCL microfibers based on SEM images [18, 41]. Analysis of SEM images shows that iNOSoxy enzyme and/or EPPS buffer containing fibers are larger in diameter than the control samples for the analyzed PCL scaffolds. Control samples are scaffolds electrospun with PCL without iNOSoxy or buffer. Figure 42 summarizes the fiber diameter increase upon embedding iNOSoxy/EPPS buffer into electrospun PCL microfibers. Overall broadening of fibers is evidence of encapsulation of aqueous pockets in emulsion electrospinning method.

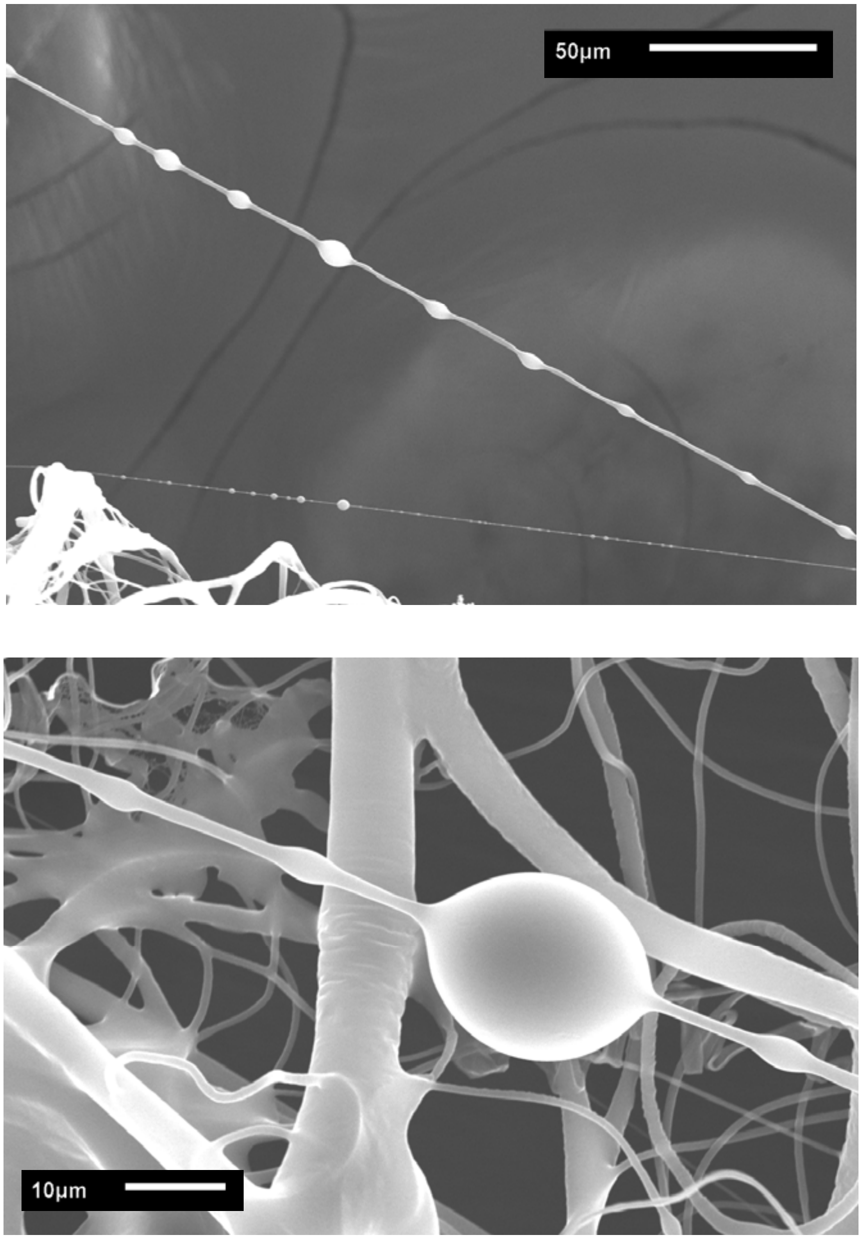

Figure 40: SEM images of electrospun 10% w/w PCL with 20:1 v/v iNOSoxy in EPPS buffer.

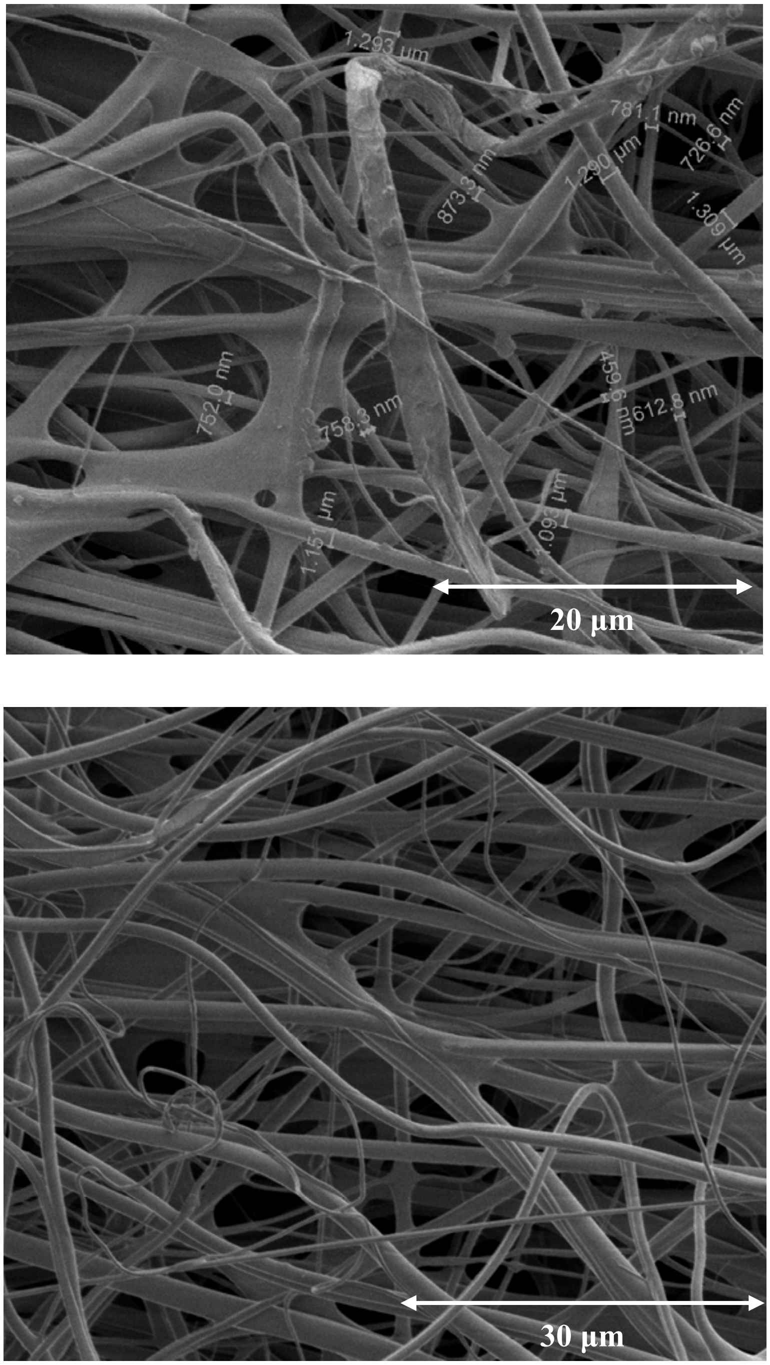

Figure 41: SEM images of electrospun 10% w/w PVA with 20:1 v/v iNOSoxy in EPPS buffer.

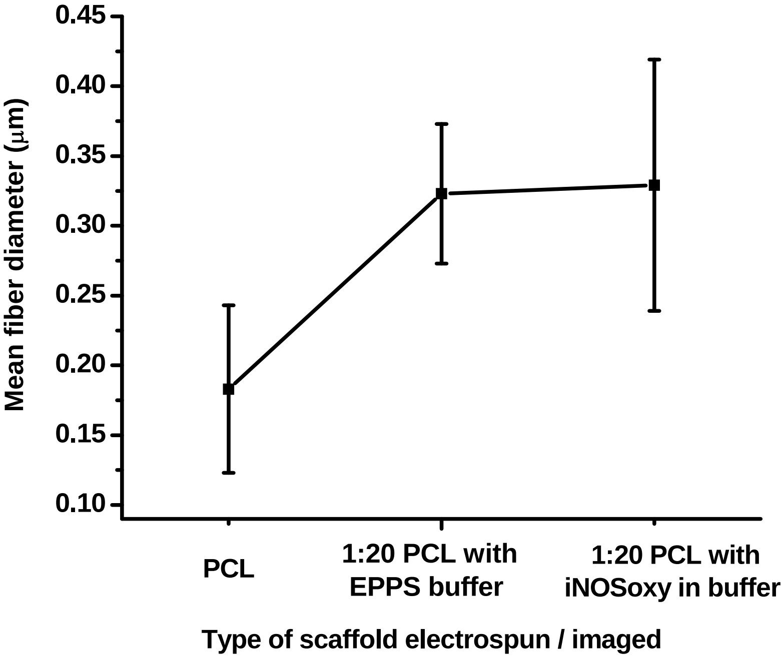

Figure 42: Mean fiber diameter of PCL showing increase of mean fiber diameter in the presence of encapsulated aqueous pockets. Error bars show standard deviations (N=43).

3.3.6 Activity of iNOSoxy enzyme embedded in scaffolds

The release of NO from iNOSoxy encapsulated in electrospun fiber is slow, compared to the cumulative NO concentrations resulting from thin film coatings of iNOSoxy. We were not able to detect significant amounts of NO using the DAF-FM diacetate fluorescence assay until after 48 hour lapse times for electrsospun fibers bathed in reaction cocktail used for the NOS reaction. Figure 43 shows measured activity of iNOSoxy in PCL electrospun fibers, beginning from 48 hours through 72 hours. Similarly, PEVA shows activity after 48 hours.

Figure 44 shows the NO flux for PCL and PEVA scaffolds. The beginning of NO release from electrospun fiber scaffolds is particularly delayed compared to the immediate burst of activity in thin LbL films of iNOSoxy. In thin films, the outermost layer of iNOSoxy is readily accessible to substrate. It is possible that access of substrate and other NOS ingredients to trapped enzyme pockets in electrospun fiber scaffolds is initially limited and longer equilibration times of the polymeric electrospun material is needed before a steady state access is established. This may explain the delayed and slow release of NO by iNOSoxy in electrospun scaffolds as observed in Figure 44.

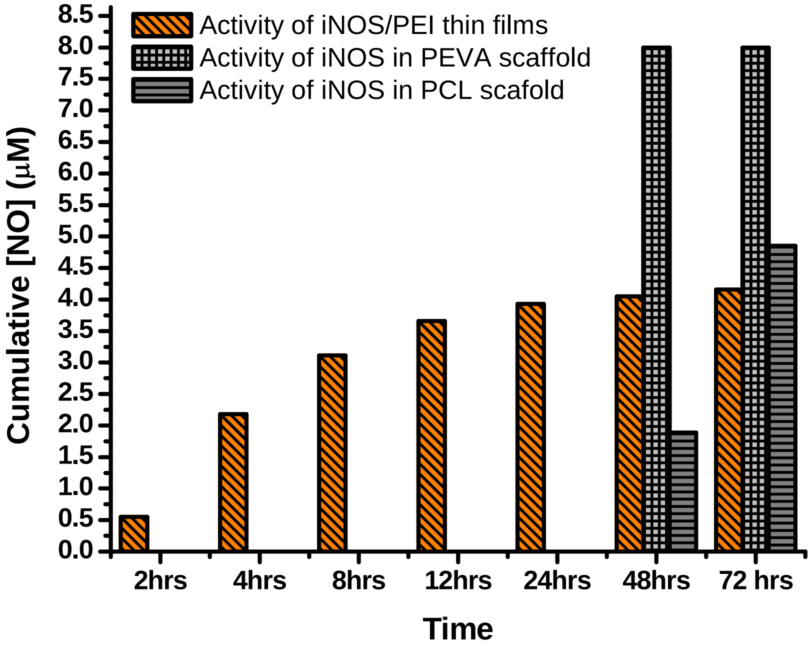

Figure 43: Cumulative NO concentration resulting from iNOSoxy embedded in PCL and PEVA scaffolds in comparison to iNOSoxy immobilized thin film activity.

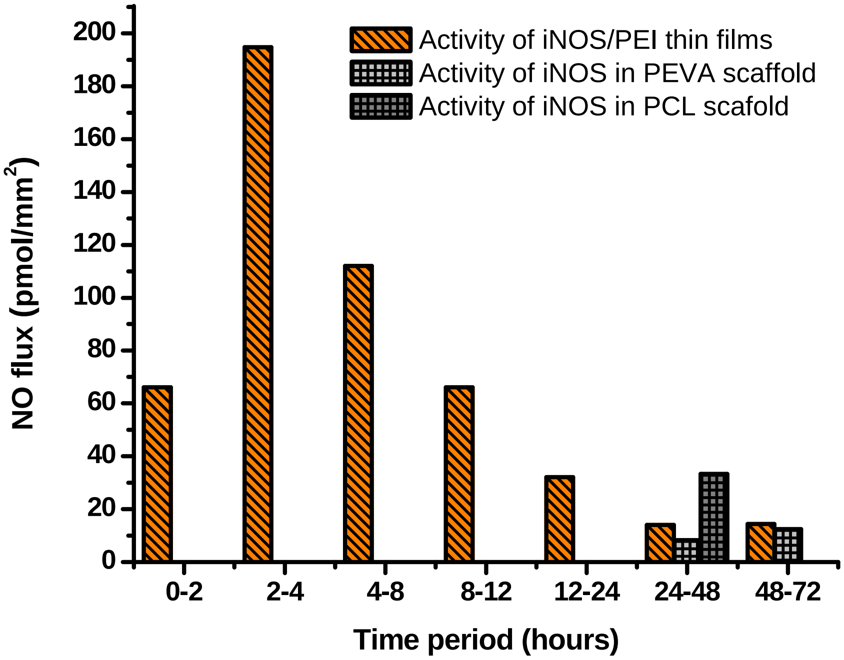

Figure 44: NO flux for each type of scaffold compared to flux of thin films of iNOSoxy.

3.4 Conclusion

This chapter describes the use of electrospinning method for fabricating iNOSoxy embedded scaffolds and mats. NOS enzymes, particularly iNOS, can be used as an antithrombogenic regimen in electrospun scaffolds and mats. As a preliminary step, we have used PCL, PEVA and PVA for the encapsulation of iNOSoxy enzyme. The average activity of iNOSoxy embedded in electrospun fibers described in this chapter is less than the activity of LbL immobilized thin films described in chapter 1 and 2. Microscopic images show successful encapsulation of iNOSoxy in aqueous pockets of microfibers, showing increase of fiber diameter.

A combination of the thin film method and electrospun based encapsulation has the potential to provide NO release to counteract thrombosis in applications requiring immediate and delayed release of NO. We are now exploring the levels and extent to which electrospun fibers with trapped NOS enzymes can sustain NO release under physiological conditions.

3.5 Reference

1. Matthews, J.A., G.E. Wnek, D.G. Simpson, and G.L. Bowlin, *Electrospinning of collagen nanofibers.* Biomacromolecules, 2002. **3**(2): p. 232-8.

2. Wutticharoenmongkol, P., N. Sanchavanakit, P. Pavasant, and P. Supaphol, *Preparation and characterization of novel bone scaffolds based on electrospun polycaprolactone fibers filled with nanoparticles.* Macromol Biosci, 2006. **6**(1): p. 70-7.

3. Boland, E.D., T.A. Telemeco, D.G. Simpson, G.E. Wnek, and G.L. Bowlin, *Utilizing acid pretreatment and electrospinning to improve biocompatibility of poly(glycolic acid) for tissue engineering.* Journal of Biomedical Materials Research Part B: Applied Biomaterials, 2004. **71B**(1): p. 144-152.

4. Telemeco, T.A., C. Ayres, G.L. Bowlin, G.E. Wnek, E.D. Boland, N. Cohen, C.M. Baumgarten, J. Mathews, and D.G. Simpson, *Regulation of cellular infiltration into tissue engineering scaffolds composed of submicron diameter fibrils produced by electrospinning.* Acta Biomater, 2005. **1**(4): p. 377-85.

5. Kenawy, E., G.L. Bowlin, K. Mansfield, J. Layman, D.G. Simpson, E.H. Sanders, and G.E. Wnek, *Release of tetracycline hydrochloride from electrospun poly(ethylene-co-vinylacetate), poly(lactic acid), and a blend.* Journal of Controlled Release, 2002. **81**(1–2): p. 57-64.

6. Son, W.K., J.H. Youk, T.S. Lee, and W.H. Park, *Effect of pH on electrospinning of poly(vinyl alcohol).* Materials Letters, 2005. **59**(12): p. 1571-1575.

7. Patel, A.C., S. Li, J.M. Yuan, and Y. Wei, *In situ encapsulation of horseradish peroxidase in electrospun porous silica fibers for potential biosensor applications.* Nano Lett, 2006. **6**(5): p. 1042-6.

8. Luu, Y.K., K. Kim, B.S. Hsiao, B. Chu, and M. Hadjiargyrou, *Development of a nanostructured DNA delivery scaffold via electrospinning of PLGA and PLA–PEG block copolymers.* Journal of Controlled Release, 2003. **89**(2): p. 341-353.

9. Garg, K. and G.L. Bowlin, *Electrospinning jets and nanofibrous structures.* Biomicrofluidics, 2011. **5**(1): p. -.

10. Bu, N., Y. Huang, Y. Duan, and Z. Yin, *Process optimization of mechano-electrospinning by response surface methodology.* J Nanosci Nanotechnol, 2014. **14**(5): p. 3464-72.

11. Jiang, H., Y. Hu, Y. Li, P. Zhao, K. Zhu, and W. Chen, *A facile technique to prepare biodegradable coaxial electrospun nanofibers for controlled release of bioactive agents.* Journal of Controlled Release, 2005. **108**(2–3): p. 237-243.

12. Zhang, Y.Z., X. Wang, Y. Feng, J. Li, C.T. Lim, and S. Ramakrishna, *Coaxial electrospinning of (fluorescein isothiocyanate-conjugated bovine serum albumin)-encapsulated poly(epsilon-caprolactone) nanofibers for sustained release.* Biomacromolecules, 2006. **7**(4): p. 1049-57.

13. Jiang, H., D. Fang, B. Hsiao, B. Chu, and W. Chen, *Preparation and characterization of ibuprofen-loaded poly(lactide-co-glycolide)/poly(ethylene glycol)-g-chitosan electrospun membranes.* Journal of Biomaterials Science, Polymer Edition, 2004. **15**(3): p. 279-296.

14. Zeng, J., X. Xu, X. Chen, Q. Liang, X. Bian, L. Yang, and X. Jing, *Biodegradable electrospun fibers for drug delivery.* Journal of Controlled Release, 2003. **92**(3): p. 227-231.

15. Chew, S.Y., J. Wen, E.K.F. Yim, and K.W. Leong, *Sustained Release of Proteins from Electrospun Biodegradable Fibers.* Biomacromolecules, 2005. **6**(4): p. 2017-2024.

16. Maretschek, S., A. Greiner, and T. Kissel, *Electrospun biodegradable nanofiber nonwovens for controlled release of proteins.* Journal of Controlled Release, 2008. **127**(2): p. 180-187.

17. Alhusein, N., I. Blagbrough, and P. Bank, *Electrospun matrices for localised controlled drug delivery: release of tetracycline hydrochloride from layers of polycaprolactone and poly(ethylene-co-vinyl acetate).* Drug Delivery and Translational Research, 2012. **2**(6): p. 477-488.

18. Li, L., Y. Qian, C. Jiang, Y. Lv, W. Liu, L. Zhong, K. Cai, S. Li, and L. Yang, *The use of hyaluronan to regulate protein adsorption and cell infiltration in nanofibrous scaffolds.* Biomaterials, 2012. **33**(12): p. 3428-45.

19. Maheshwari, S., S. Kumar, N. Nagiah, and T. Uma, *Electrospinning of polyvinylalcohol–polycaprolactone composite scaffolds for tissue engineering applications.* Polymer Bulletin, 2013. **70**(11): p. 2995-3010.

20. Song, W., X. Yu, D.C. Markel, T. Shi, and W. Ren, *Coaxial PCL/PVA electrospun nanofibers: osseointegration enhancer and controlled drug release device.* Biofabrication, 2013. **5**(3): p. 035006.

21. Li, X., M.A. Kanjwal, L. Lin, and I.S. Chronakis, *Electrospun polyvinyl-alcohol nanofibers as oral fast-dissolving delivery system of caffeine and riboflavin.* Colloids Surf B Biointerfaces, 2013. **103**: p. 182-8.

22. Stone, S.A., P. Gosavi, T.J. Athauda, and R.R. Ozer, *In situ citric acid crosslinking of alginate/polyvinyl alcohol electrospun nanofibers.* Materials Letters, 2013. **112**(0): p. 32-35.

23. Yao, L., T.W. Haas, A. Guiseppi-Elie, G.L. Bowlin, D.G. Simpson, and G.E. Wnek, *Electrospinning and Stabilization of Fully Hydrolyzed Poly(Vinyl Alcohol) Fibers.* Chemistry of Materials, 2003. **15**(9): p. 1860-1864.

24. Shaikh, R.P., P. Kumar, Y.E. Choonara, L.C. du Toit, and V. Pillay, *Crosslinked electrospun PVA nanofibrous membranes: elucidation of their physicochemical, physicomechanical and molecular disposition.* Biofabrication, 2012. **4**(2): p. 025002.

25. Defrere, S., M. Mestagdt, R. Riva, F. Krier, A. Van Langendonckt, P. Drion, C. Jerome, B. Evrard, J.P. Dehoux, J.M. Foidart, and J. Donnez, *In vivo biocompatibility of three potential intraperitoneal implants.* Macromol Biosci, 2011. **11**(10): p. 1336-45.

26. Lefevre-Groboillot, D., J.L. Boucher, D. Mansuy, and D.J. Stuehr, *Reactivity of the heme-dioxygen complex of the inducible nitric oxide synthase in the presence of alternative substrates.* Febs j, 2006. **273**(1): p. 180-91.

27. Pufahl, R.A., J.S. Wishnok, and M.A. Marletta, *Hydrogen Peroxide-Supported Oxidation of NG-Hydroxy-L-Arginine by Nitric Oxide Synthase.* Biochemistry, 1995. **34**(6): p. 1930-1941.

28. Sheng, J.Z., D. Wang, and A.P. Braun, *DAF-FM (4-amino-5-methylamino-2',7'-difluorofluorescein) diacetate detects impairment of agonist-stimulated nitric oxide synthesis by elevated glucose in human vascular endothelial cells: reversal by vitamin C and L-sepiapterin.* J Pharmacol Exp Ther, 2005. **315**(2): p. 931-40.

29. Diez, I., S. Calatayud, C. Hernandez, E. Quintana, J.E. O'Connor, J.V. Esplugues, and M.D. Barrachina, *Nitric oxide, derived from inducible nitric oxide synthase, decreases hypoxia inducible factor-1alpha in macrophages during aspirin-induced mesenteric inflammation.* Br J Pharmacol, 2010. **159**(8): p. 1636-45.

30. Baron, M.H., Revault, M., Servagent-Noinville, S., Abadie, J., Quiquampoix, H., *Chymotrypsin adsorption on Montmorillonite: Enzymatic activity and kinetic FTIR structural analysis.* Journal of Colloid and Interface Science, 1999. **214**(2): p. 319-332.

31. Venyaminov, S. and N.N. Kalnin, *Quantitative IR spectrophotometry of peptide compounds in water (H2O) solutions. I. Spectral parameters of amino acid residue absorption bands.* Biopolymers, 1990. **30**(13-14): p. 1243-57.

32. Krimm, S. and J. Bandekar, *Vibrational spectroscopy and conformation of peptides, polypeptides, and proteins.* Adv Protein Chem, 1986. **38**: p. 181-364.

33. Nevskaya, N.A. and Y.N. Chirgadze, *Infrared spectra and resonance interactions of amide-I and II vibration of alpha-helix.* Biopolymers, 1976. **15**(4): p. 637-48.

34. Klibanov, A.M., *Improving enzymes by using them in organic solvents.* Nature, 2001. **409**(6817): p. 241-246.

35. Li, C., R. Fu, C. Yu, Z. Li, H. Guan, D. Hu, D. Zhao, and L. Lu, *Silver nanoparticle/chitosan oligosaccharide/poly(vinyl alcohol) nanofibers as wound dressings: a preclinical study.* Int J Nanomedicine, 2013. **8**: p. 4131-45.

36. Manasco, J.L., C. Tang, N.A. Burns, C.D. Saquing, and S.A. Khan, *Rapidly dissolving poly(vinyl alcohol)/cyclodextrin electrospun nanofibrous membranes.* RSC Advances, 2014. **4**(26): p. 13274-13279.

37. Ramalingam, M., M.F. Young, V. Thomas, L. Sun, L.C. Chow, C.K. Tison, K. Chatterjee, W.C. Miles, and C.G. Simon, Jr., *Nanofiber scaffold gradients for interfacial tissue engineering.* J Biomater Appl, 2013. **27**(6): p. 695-705.

38. Gök, E. and S. Olgaz, *Binding of Fluorescein Isothiocyanate to Insulin: A Fluorimetric Labeling Study.* Journal of Fluorescence, 2004. **14**(2): p. 203-206.

39. Majima, E., M. Ishida, S. Miki, Y. Shinohara, and H. Terada, *Specific Labeling of the Bovine Heart Mitochondrial Phosphate Carrier with Fluorescein 5-Isothiocyanate: ROLES OF LYS185 AND PUTATIVE ADENINE NUCLEOTIDE RECOGNITION SITE IN PHOSPHATE TRANSPORT.* Journal of Biological Chemistry, 2001. **276**(13): p. 9792-9799.

40. Haynie, D.T., D.B. Khadka, and M.C. Cross, *Physical Properties of Polypeptide Electrospun Nanofiber Cell Culture Scaffolds on a Wettable Substrate.* Polymers, 2012. **4**(3): p. 1535-1553.

41. Sant, S., C.M. Hwang, S.-H. Lee, and A. Khademhosseini, *Hybrid PGS–PCL microfibrous scaffolds with improved mechanical and biological properties.* Journal of Tissue Engineering and Regenerative Medicine, 2011. **5**(4): p. 283-291.